Université de Neuchâtel Institut de Physique de l' Université de Neuchâtel

Optical Pumping: A Possible Approach towards a SiGe Quantum Cascade Laser

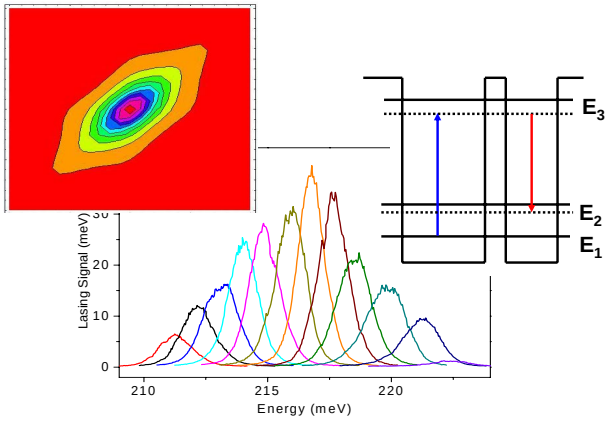

THESE

présentée à la Faculté des Sciences de l'Université de Neuchâtel pour obtenir le grade de docteur ès sciences

par

Maxi Scheinert

Soutenue le 8 octobre 2007

En présence du directeur de thèse

Prof. Jérôme Faist

et des rapporteurs

Prof. Detlev Grützmacher , Prof. Peter Hamm, Prof. Philipp Aebi, Dr. Hans Sigg and Dr. Soichiro Tsujino

Université de Neuchâtel

FACULTE DES SCIENCES
Secrétariat-Décanat de la faculté
- Rue Emile-Argand 11
- CP 158
- CH-2009 Neuchâtel

IMPRIMATUR POUR LA THESE

Optical pumping : a possible approach towards a SiGe quantum cascade laser ?

Maxi SCHEINERT

UNIVERSITE DE NEUCHATEL

FACULTE DES SCIENCES

La Faculté des sciences de l'Université de Neuchâtel,
sur le rapport des membres du jury

MM. J. Faist (directeur de thèse), P. Aebi,
H. Hamm (Zürich), D. Grützmacher (Julich D)
H. Sigg (PSI) et S. Tsujino (PSI)

autorise l'impression de la présente thèse.

Neuchâtel, le 15 novembre 2007

Le doyen :
T. Ward

UNIVERSITE DE NEUCHATEL
FACULTE DES SCIENCES
Secrétariat-décanat de la faculté
Rue Emile-Argand 11 - CP 158
CH-2009 Neuchâtel

Keywords

- Semiconductor heterostructures
- Intersubband Transitions
- Quantum cascade laser
- Si - SiGe
- Optical pumping

Mots-Clés

- Hétérostructures semiconductrices
- Transitions intersousbande
- Laser à cascade quantique
- Si - SiGe
- Pompage optique

Abstract

Since the first Quantum Cascade Laser (QCL) was realized in 1994 in the AlInAs/InGaAs material system, it has attracted a wide interest as infrared light source. Main applications can be found in spectroscopy for gas-sensing, in the data transmission and telecommunication as free space optical data link as well as for infrared monitoring.
This type of light source differs in fundamental ways from semiconductor diode laser, because the radiative transition is based on intersubband transitions which take place between confined states in quantum wells. As the lasing transition is independent from the nature of the band gap, it opens the possibility to a tuneable, infrared light source based on silicon and silicon compatible materials such as germanium. As silicon is the material of choice for electronic components, a SiGe based QCL would allow to extend the functionality of silicon into optoelectronics. The aim of this thesis is to provide possible opportunities to achieve lasing in silicon by using intersubband transitions.
Electroluminescence from SiGe quantum cascade structures was demonstrated in 2002. The present thesis summarizes complementary research regarding electrically pumped SiGe QC structures. On the basis of these results, the problems arising from the electrical pumping at high current densities in SiGe QCs are discussed. The main problem can be found in the free carrier absorption in the strongly doped region providing the electrical contacts. Furthermore, the accurate growth of strained SiGe layers is challenging with respect to the alignment of levels. The latter one is of special importance for the proper injection of carriers. To overcome those problems, another approach was chosen: the optical pumping. Here, carriers are excited to the upper laser state by using an external laser source. This provides several advantages: (i) simple three level structures are sufficient which are either realized by double quantum wells or simple step QWs (ii) no need of doped contact layers and a lower doping in the active region which reduces free carrier losses; (iii) the growth conditions are less stringent as the injection into the upper laser state is provided by a tunable external source.
The realization of this approach is presented in the main part of this thesis. The optical pumping set-up was tested using AlInAs/GaInAs double quantum well structures. From those samples, Raman lasing was obtained which is attributed to a lack of population inversion. Theoretical analysis and femto-second time-resolved measurements were employed to clarify the origin of this behavior.
For approaching optical pumping in the SiGe material system, three level systems obtained by a double quantum well and a step quantum well were investigated. Theoretical considerations and absorption measurements were performed in order to characterize the

designs. The step QW was concluded to be the most suitable design due to its design freedom and the few growth interfaces. Lasing, however, could not be achieved what is probably due to unsatisfactory material quality. Promising results on the latest sample batch are summarized in an appendix.

Résumé

Le laser à cascade quantique a attiré un large intérêt en tant que source infrarouge depuis sa première réalisation en 1994 en utilisant l'AlInAs/InGaAs. Ses applications principales sont dans la spectroscopie pour la détection des gaz, ainsi que pour les télécommunications à travers l'atmosphère.
Ce type de source optique diffère de manière fondamentale d'une diode laser semi-conducteur conventionnelle, car la transition radiative est basée sur des transitions inter-sous-bandes qui ont lieu entre des états confinés dans des puits quantiques. Comme la transition laser est maintenant indépendante de la nature de la bande interdite (directe ou indirecte), ce concept ouvre la voie à l'utilisation du silicium, ou d'autre matériaux comme le SiGe, compatibles avec le silicium, pour obtenir une source infrarouge accordable. Comme le Silicium est le matériau privilégié pour les dispositifs électroniques, un laser à cascade quantique basé sur le SiGe permettrait de rajouter la fonctionnalité optoélectronique au silicium. Le but de cette thèse est d'essayer d'utiliser les transitions inter-sous-bandes pour réaliser un laser basé sur la technologie du silicium.
L'électroluminescence de structures à cascade quantique basées sur le SiGe a été montrée en 2002. Cette thèse présente une étude complémentaire concernant les structures à cascade quantiques pompées électriquement. Sur la base de ces résultats, les problèmes soulevés par l'injection des forts courants nécessaires l'injection électrique dans les structures à cascades basées sur le SiGe sont discutés. Un des problèmes principaux est l'absorption par les porteurs libres dans les régions fortement dopées utilisées pour l'injection du courant dans la structure. Une difficulté supplémentaire est la croissance précise des couches contraintes de SiGe qui puissent maintenir un bon alignement des niveaux électroniques, indispensable pour une injection efficaces dans les états désirés. Pour résoudre ces problèmes, une autre approche a été utilisée: le pompage optique, dans lesquel les électrons sont amenés sur l'état excité après l'absorption d'un photon. Cette approche a plusieurs avantages. Premièrement une structure simple à trois niveaux est suffisante, qui peut être réalisée à l'aide d'un puit couplé ou d'un puit avec une marche de potentiel. Deuxièmement les couches qui oeuvrent de contacts électriques peuvent être évitées, ainsi que les pertes optiques induites. Finalement les exigences sur la précision de la croissance sont un peu moindres vu que l'injection peut être "accordée" par un changement de la longueur d'onde de pompage.
La réalisation de cette approche a représenté la partie principale de cette thèse. L'expérience de pompage optique a été testé en utilisant un puit couplé AlInAs/GaInAs. Les résultats obtenus l'aide de ces échantillons ont montré que le mécanisme de gain obtenu provenait

d'un effet Raman électronique plutôt que d'une inversion de population. Une analyse théorique ainsi que des mesures en temps résolu ont été utilisées pour bien identifier le mécanisme d'opérations du laser.
Pour réaliser la même approche dans les matériaux à base de SiGe, des systèmes à trois niveaux obtenus dans des puits couplés et dans un puit à marche de potentiel ont été étudiés. Des considérations théoriques, ainsi que des mesures d'absorption on été utilisées pour caractériser différents options conceptuelles. Le puit à marche de potentiel s'est révélé être l'approche la plus fructueuse à cause de la liberté de concept qu'il offrait ainsi que la présence d'un nombre moindre d'interfaces. Malheureusement, aucun effet laser n'a été observé. Des résultats en absorption prometteurs sont résumés dans un appendice.

Contents

List of acronyms used throughout this work

Ge	Germanium
Si	Silicon
SiGe	Silicon-Germanium
InP	Indium-Phosphite
AlInAs	Aluminium-Indium-Aresnide
GaInAs	Gallium-Indium-Arsenide
QW	Quantum Well
QCL	Quantum Cascade Laser
QC	Quantum Cascade
DQW	Double Quantum Well
StepQW	Step Quantum Well
SL	Superlattice
RTD	Resonant Tunnelling Diode
HH	Heavy Hole
LH	Light Hole
SO	Split-Off
FIR	Far-infrared
MIR	Mid-infrared
TE	Transverse Electric
TM	Transverse Magnetic
MBE	Molecular Beam Epitaxy
FTIR	Fourier Transform Infrared Spectrometer
TEM	Transmission Electronic Microscope
FWHM	Full Width at Half Maximum
Γ	Linewidth
LI	Light-Current
VI	Voltage-Current

Chapter 1

Introduction

1.1 Motivation

Since the first quantum cascade laser (QCL) realized in the AlInAs/GaInAs system was demonstrated in 1994 [1], the possibility of lasing independent from the nature of the bandgap raised the wish to realize this concept in Si-based heterostructures. This approach could connect two important features which are a longtime focus of intense research: the tunable mid-infrared light source and the silicon light emitter.
The long wavelength regime in the mid-infrared has attracted special interest because of the atmospheric windows situated at wavelengths of $3-5\mu$m and $8-13\mu$m where many molecules have their vibrational modes. In the last twenty years, several different solid state laser sources emitting in this wavelength range have been developed:

- lead-salt interband laser [2]
- antimony based interband laser [3]
- interband quantum cascade laser [4]
- p-germanium laser based on inversion between Landau levels [5]
- intersubband quantum cascade lasers in the III-V material system [1].

Among all these devices, the QCL has the greatest flexibility regarding the wavelength range and operation temperature. Furthermore, it relies on intersubband transitions which implies the possibility to realize such a system in a Si-based material system as shown in Section 2.1.
Silicon is the dominating semiconductor for electronic applications. The main reason for its technological domination is the possible low-cost and large scale integration of devices. Furthermore, the large band gap of Si is ideal for room temperature operation and its high quality oxides (SiO_2, Si_3N_4) can be easily grown and processed. Nowadays, chips with a high integration density (a Pentium 4 microprocessor consist of about $55 \cdot 10^6$ transistors) on 8 inch Si wafer can be produced. Up to now, the switching behavior of the single devices was the speed limiting factor. In the current state of the art, the interconnection

(or data transport) between devices on one chip will be the limiting process in order to follow the predictions of Moore's law. This gave rise to the idea to combine electronic with optical components on one chip and provide the data exchange between the single devices via photons. This combination of silicon micro- and optoelectronics is a longstanding dream which drove a widespread scientific and technical interest. However, for a long period, only passive Si based devices could be demonstrated (for a review see [6]) while no practical light source on Si could be realized. The reason for this difficulty can be explained by the indirect band gap of silicon which makes radiative transitions via the band gap unlikely. Due to this, common interband lasers as realized in the III-V system were impossible to achieve using silicon. To overcome this problem and fabricate efficient Si based light emitters, several strategies have been explored of which some are briefly summarized in the following:

- *Band gap based devices* In that kind of light emitting diodes (LEDs), recombination over the band gap through non radiative transitions is prevented by localizing the carriers in defect-free regions which is achieved by implanting Boron [7]. Another approach is to enhance the absorbance and hence the emissivity of a p-n junction diode by suitable texturing its surface [8]. Although strong luminescence has been demonstrated, lasing action will be very difficult to achieve with these devices as they still rely on the ineffective indirect band gap. Besides, integration of a waveguide and the compatibility of surface texturing with standard CMOS processing is not clarified.

- *porous Silicon* The idea of using porous silicon which is a spongy phase of Si was pioneered by L.Canham in 1990 [9] who showed that visible light can be efficiently emitted by porous Si. Devices exploiting this radiative process have been demonstrated later on [10]. Despite of its very efficient photo- and electroluminescence, optical gain was not observed so far and the aging of the material is a severe problem.

- *Silicon nanocrystals* Optical gain in silicon nanocrystals was reported in 2000 for the first time [11]. The luminescence properties of Si-nc are very similar to those of porous silicon: a wide emission band is observed at room temperature whose spectral position depends on the size of the Si-nc. Here, the problem of an inhomogeneous size distribution still needs to be solved. An effective four-level system presented in [12], [13] has been proposed to explain the build-up of population inversion. This approach seems to be promising for the realization of Si based lasers although the implementation in CMOS technology and in particular the electrical pumping of the devices might be a quasi-impossible task since SiO_2 is among the best insulating materials.

- *Erbium doped silicon* Erbium ions exhibit a sharp luminescence at the very important 1.54μm wavelength. Er-doped silica fibers are widely used as light amplifiers or lasers in all-optical data links. By adapting this concept to silicon crystals, electrically pumped LEDs operating at room temperature have been demonstrated [14], [15].

- *SiGe quantum dots* Quantum dots were successfully used to realized low-threshold interband lasers using group III-V materials [16]. This could be applied to strained Si/SiGeC material. The pre-deposition of C allows to grow QDs whose diameter and height are as small as 70-200 Å and 20 to 30 Å respectively [17], [18]. However, gain was not yet observed in these structures as the site of the dots and their lateral dimension my still be too large.

- *SiGe based Quantum Cascade Laser* These devices are the topic of this thesis and will be explained in detail in the following chapters.

Many of these approaches are still under investigation and possible ways towards a silicon based light laser. However, within the last three years, two functional concepts of silicon laser have been presented by the Intel cooperation and the University of California:

Hybrid Silicon Laser

Hybrid lasers are an alternative way to achieve Si based emitters. In such devices, III-V lasers are coupled to silicon waveguides which is called hybrid integration: First, the silicon waveguides are fabricated on a silicon-on-insulator (SOI) substrate which is then aligned to the III-V laser. This latter process can be done either by flip-chip bonding [19],[20] , self assembly [21] or vertical coupling of membrane devices [22]. For all these methods, the problem of aligning two devices of different dimensions and materials increases costs and is time-consuming. In 2006, *Fang et al.* finally presented an electrically driven hybrid

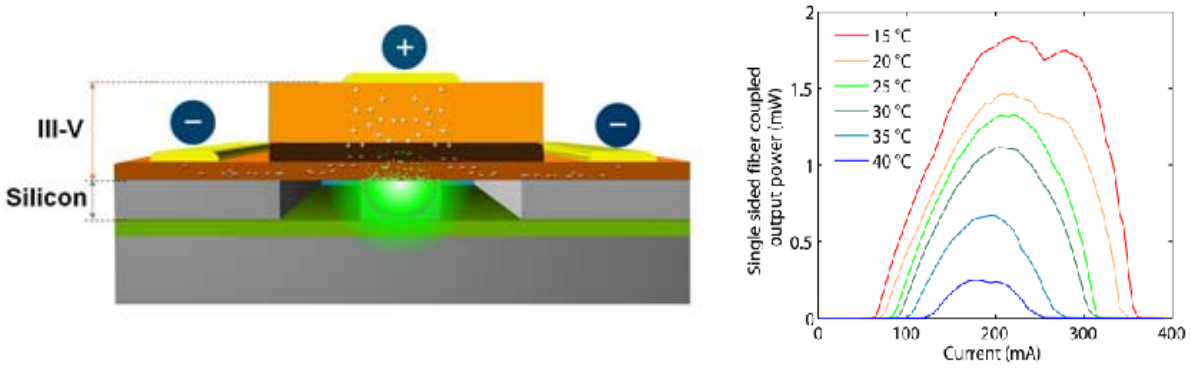

(a) (b)

Figure 1.1: (a) Schematic cross section of a hybrid silicon laser. The III-V and silicon parts are indicated as well as the metal contacts. (b) Single sided laser output as a function of drive current and operating temperatures. After [23].

AlGaInAs-silicon evanescent laser [23] which is a further development of the previously presented optically pumped silicon evanescent laser [24]. The cross section and a lasing spectra of such a laser are shown in Figure 1.1. As it can be electrically driven, no external laser source is necessary which is advantageous with respect to integration and applications. Furthermore, it is a self-aligning device: The optical mode of the III-V laser (bonded to the Si waveguide, see Fig. 1.1a), overlaps with both, the III-V material and

the silicon waveguide. This mode can be electrically excited by the III-V region while it is guided through the silicon waveguide. As the III-V region is symmetric in lateral dimension, no alignment steps are necessary before bonding.
In Figure 1.1b, the measured c.w.laser output power from one facet in dependence on the injected current is shown (after [23]). The lasers threshold is about 65mA with a maximum output power of 1.8mW and a differential quantum efficiency of 12%. Operation temperatures up to 40°C have been achieved. Up to 100 lasers can be fabricated in one step without critical alignment of III-V active material and silicon waveguide which makes the process suitable for high volume and low-cost integration.
Further approaches using silicon based integration of III-V lasers were e.g. recently shown by *Van Campenhout et al.* who integrated InP based microdisk lasers on SOI wafers [25] or by *Vecchi et al.* with the integration of III-V photonic crystals on silicon wafers [26].

All Silicon Raman Laser

The first all silicon laser was realized by *Rong et al.* using light amplification on the basis of the 'stimulated Raman scattering' (SRS). It was first demonstrated in pulsed operation [27] and later on as continuous-wave Raman silicon laser [28]. For a review, see also [29]. Stimulated Raman Scattering has been used within the last years to demonstrate several silicon sources for light amplification and lasing (see for example [30]-[32]). SRS is a non-

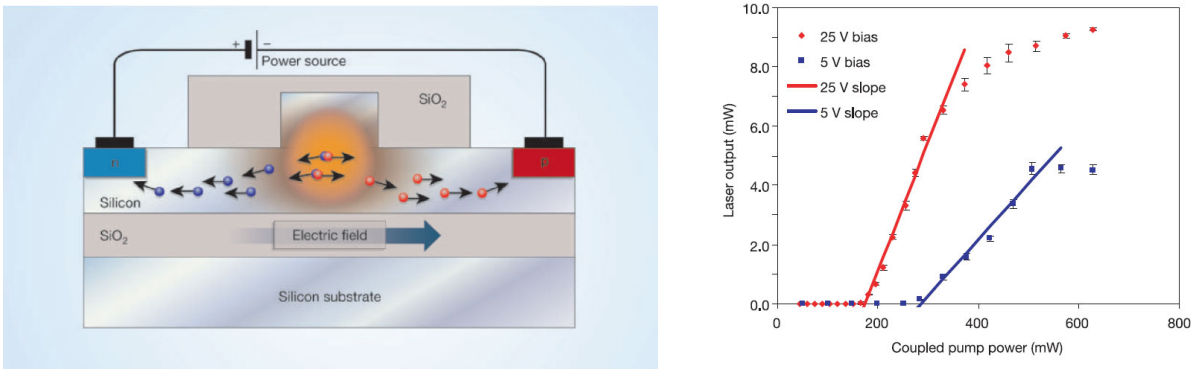

(a) (b)

Figure 1.2: (a) Cross section of a silicon-on-insulator rib waveguide containing a reverse biased p-i-n diode structure with an applied voltage. (b) Output power as a function of input power for two different applied voltages. The pump wavelength is 1550nm and the lasing wavelength 1686nm. (After [28].)

linear optical effect in which a pump laser photon is absorbed and re-emitted as a signal photon of a longer wavelength and an additional phonon [33]. By this process, the pump energy is converted into a signal beam which is then amplified (Raman amplification). This implies the need of a strong optical pump laser. As Raman based amplification is a comparably small effect, besides the strong pumping, very low absorption processes are required. Therefore, the device was based on the SOI technology: A low-loss single mode rib waveguide was fabricated on a SOI substrate. The rib waveguide contains a

reverse biased p-i-n diode structure which reduces the free carrier absorption (FCA) induced by the two-photon absorption (TPA). Due to the large step in the refractive index between crystalline silicon (n=3.6) and silica layers (n=1.5), a tight mode confinement can be achieved. A cross section of such a silicon rib waveguide is shown in Figure 1.2a (after[28]). In Figure 1.2b, the threshold characteristics of a Silicon Raman laser in dependence on the input power are shown. Threshold values of $\sim$ 280mW (5V reverse bias) to $\sim$ 180mW (25V reverse bias) are obtained. An output power between 400mW to 600mW and a slope efficiency of 4.2% to 2% were reported. The observed saturation is mainly due to the TPA-induced FCA which is caused by the non-zero lifetime in the p-i-n waveguide. With this design, a silicon laser with continuous operation was demonstrated. However, the use of nonlinear optical processes will always require optical pumping via a strong external laser source of which only a small percentage will be transferred into laser light. This will be the limiting parameter regarding application and output power.

1.2 Scope and organization of this thesis

In the frame of this work, another approach towards a Si based light emitter will be explored. In previous works (for a summary see [34], [35]), the possibility of realizing an electrically pumped SiGe quantum cascade laser (QCL) has been investigated and electroluminescence from intersubband transitions was reported [36], [37]. The present work is continuing the above mentioned research and is organized in the following way: In Chapter 2, an overview about intersubband processes and quantum cascade lasers will be given. This is followed by the theoretical basis used for the design and simulation of the SiGe quantum well structures (Chapter 3). The choice of p-type SiGe structures will be motivated. Technical aspects regarding MBE growth and measurement setups will be given in Chapter 4 and 5. The experiments carried out within the last four years on electrically pumped SiGe structures will be discussed in Chapter 6. The investigations regarding contact and waveguide design as well as results from resonant tunnelling experiments will be addressed. Obstacles which still have to be overcome are discussed. As these problems were improbably to be solved by using electrical pumping of the structures, another approach was chosen: The optical pumping. The concept was tested using III-V quantum well structures as described in Chapter 7. The observed Raman lasing was further investigated using different designs. This concept is then transferred into the SiGe material system using two different designs as discussed in Chapter 8. Absorption measurements on waveguide structures were employed in order to characterize the grown SiGe structures. In Chapter 9, the steps towards an optically pumped SiGe quantum well laser will be summarized and possible further steps will be given.

Chapter 2

Intersubband Transitions and Quantum Cascade Lasers

In this chapter, intersubband (ISB) transitions are generally introduced and their some aspects of their physics are briefly given. The main features of ISB transitions in SiGe are summarized as they are treated in detail in chapter 3. The basic principle of quantum cascade lasers is then described. Finally, some applications for QCLs are given. It has to be noted, that for devices realized in the III-V system, the conduction band and processes involving electrons are treated. For SiGe structures, the valence band and hole-involving processes are described. By convention, (x, y) and z refers to the in-plane directions (parallel to the layers) and the growth direction (perpendicular to the layers).

2.1 Intersubband versus Interband Transitions

Conventional solid state lasers (including interband quantum well lasers) rely on transitions between energy bands. Such kind of lasers is used in CD, DVD or for telecommunication. The optical transition is an interband transition between conduction and valence band in which electrons and holes recombine across the band gap. This includes that the band gap of the material determines the emission wavelength as schematically shown in Figure 2.1a. The gain for these interband transitions is limited by the joint density of states and saturates when the electron and hole quasi Fermi level is well within the conduction and valence band, respectively. Radiative lifetimes are in the order of 1ns.
The devices described within this work are relying on a different kind of transition. The main feature of an intersubband laser or quantum cascade laser is its unipolarity: only one type of carriers, electrons or holes, are involved in the process. The unipolar nature of the optical transition is based on the use of subbands within the conduction or valence band, respectively, which are formed in quantum wells (QW) in semiconductor heterostructures. The QWs can be achieved by embedding a thin layer of a semiconductor between two layers of another semiconductor who has a larger band gap energy. This situation is shown in Figure 2.1b: Depending on the material composition and the thickness of the different layers, the motion of the carriers in the growth direction can be restricted to the QW

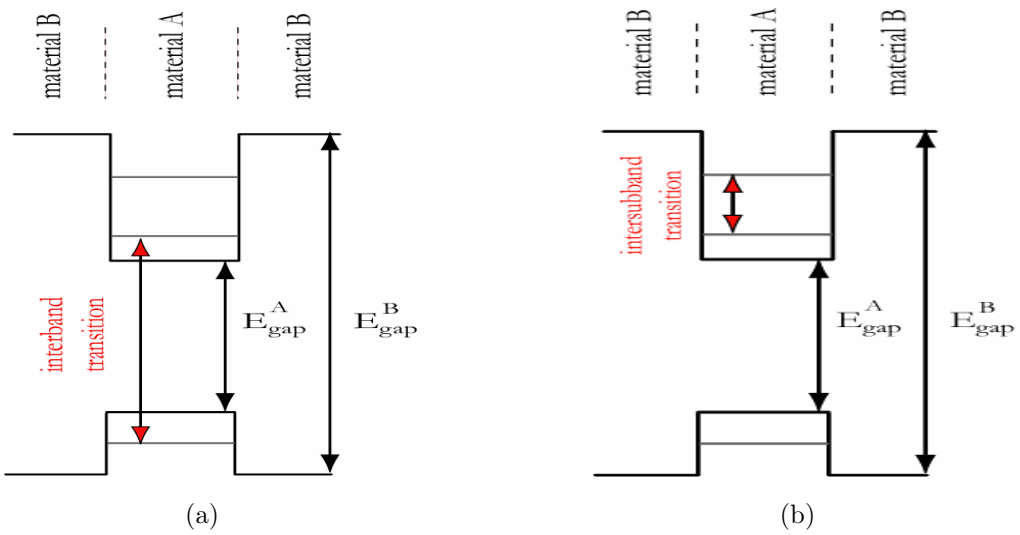

Figure 2.1: Schematic drawing representing quantum wells formed with two different semiconductors having different band gap energy. The confined states are indicated by red lines and the interband (a) and intersubband (b) transition by arrows.

layer and quantized. By this, discrete energy levels, called subbands are formed. Both, the initial and final state of the optical transition are within one band (the conduction band in this example). These confinement effects have first been reported by *Esaki and Tsu* in the 70's in transport experiments [38] and by *R.Dingle et al.* in optical absorption measurements [39]. The first intersubband absorption was observed by West and Eglash in 1985 [40].
An important property of the intersubband systems is the tunability of the emission wavelength: For a quantum cascade laser, the emission wave length is not an intrinsic property of the semiconductor used but can be adjusted by changing the thickness of the epitaxial layers as well as their composition. By this, wavelengths covering the entire near- to far-infrared spectrum are accessible. Intersubband absorption ranging from 1.4μm [41] to 200μm [42] has been demonstrated. In the III-V system (InGaAs/InAlAs) emission wavelengths between 3.4μm [43] and 24μm [44] were achieved. In the long wavelength range, terahertz lasing between 1THz to 3THz has been achieved (see e.g. [45], [46]). The only wavelength region in which the realization of a III-V QCL is not possible is the so-called *Reststrahlenband*. There, the light can not propagate because the material is highly dispersive and heavily absorbing due to the interaction of the light with the optical phonons of the material. In InGaAs for example, this region is found around 30μm-60μm.

2.1.1 Intersubband Transitions in SiGe

The concept of intersubband transitions implies a big advantage for a Si based light emitter: As silicon is an indirect band gap material, radiative transitions over the band gap are very unlikely as they require a momentum transfer via phonons (see Fig. 2.2). Therefore, an interband diode laser as realized for III-V systems becomes improbable. In the

quantum cascade laser concept, this fundamental restriction is circumvented as the optical transitions take place in either the valence or the conduction band as described above. Hence, the nature of the bandgap does not influence the optical transitions as shown in Figure 2.2b. So far, there is no real physical limitation to the application of this concept to the SiGe system.

Nevertheless, this task is not trivial because of several challenges: The large lattice

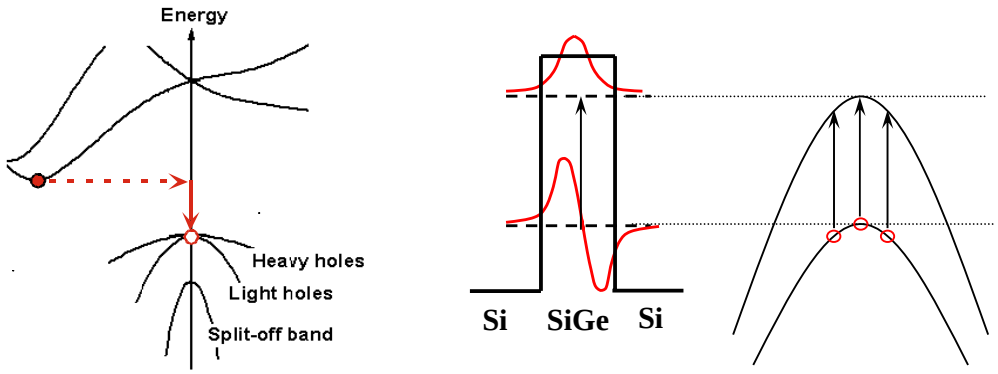

(a) (b)

Figure 2.2: (a) Dispersion of the conduction and valence band in silicon. (b) Real space band diagram representing a Si/SiGe QW. The real part of the electronic wavefunctions are shown. On the right hand side the dispersion of the electronic subbands is shown.

mismatch between Si and Ge ($\sim 4\%$) requires careful strain compensation (see also chapter 3.2.3) which needs to be taken into account when designing a structure. Furthermore, the band offset in the conduction band of Si/SiGe heterostructures grown pseudomorphically on Si substrates is too small to be useful for the design of cascade structures. A possible solution for this is the growth of Si/SiGe structures on SiGe pseudosubstrates which allows sizeable conduction band offset. However, for that type of structure, the electron tunnelling mass is probably too large ($> 0.85m_0$ [47]) to allow efficient tunnelling processes. For those reasons, one needs to work in the more complicated valence band which is described in detail in chapter 3. Besides this, working with QWs gives a control to most of the properties of the structure such as the carrier transport, on the contrary to most attempts tried so far to fabricate Si-based light sources. In particular the population inversion in QCLs is engineered, e.g. can be achieved through a careful design of the optically active region.

At present, electroluminescence originating from intersubband transitions in Si-based QC structures has been demonstrated in the mid-infrared ([36],[37]) and the far-infrared ([48],[49]). More details on those structures can also be found in [35].

The implementation of mid- or far-infrared SiGe QC lasers in standard CMOS technology will be difficult because of the low thermal budget possible for these very complicated heterostructures. The high temperature needed for the growth of thermal oxides can indeed induce the formation of defects and a severe diffusion of Ge atoms at the barrier-QW interfaces. QC lasers typically operate at large voltages and currents, which is a severe disadvantage in term of CMOS integration. Moreover, room temperature operation may

be difficult to achieve and the typical range of emission wavelength achievable with a SiGe QC laser is quite different from those commonly used in telecommunication.
On the other hand the fabrication of vertically emitting cavity lasers with p-type QC structures is possible which is an important advantage for applications. Moreover QC lasers emitting at wavelengths ranging from about 30 to 60μm are not feasible in III-V materials because of the strong phonon-light interaction. This process is absent in non-polar materials such as Si and Ge and therefore SiGe QC lasers can in principle cover the entire spectrum, from the mid- to far-infrared wavelengths.

2.2 The principle of Quantum Cascade Lasers

The concept of a laser based on intersubband transitions in semiconductor heterostructures has first been proposed in the early seventies by Kazarinov and Suris, who predicted the stimulated emission of infrared light in a strongly biased superlattice [50]. This drove an intense experimental and theoretical work which led to the demonstration of intersubband electroluminescence in 1988 by *M. Helm et al.* [51] In 1994, *Faist et al.* realized at Bell Labs the first quantum cascade laser in $Ga_{0.47}In_{0.53}As/Al_{0.48}In_{0.52}As$ lattice matched to InP [1]. Since then, numerous milestones have been achieved, such as continuous operation at room-temperature[52] and the extension of emission wavelength from the mid- to the far-infrared [53]. Lasing action has also been demonstrated in GaAs/AlGaAs [54] and InAs/AlSb [55]. Attempts to fabricate QCLs in other material systems are being made. In particular nitride alloys have brought a marked attention because the possibility of reaching the very important wavelengths commonly used in telecommunications (1.55μm) [41]. Cascade structures based on Si/SiGe alloys are also of special interest as already discussed in the precedent chapter.
A fundamental feature of the intersubband quantum cascade laser is its multistage cascade scheme: Electrons are recycled from period to period contributing each time to the gain and photon emission as shown in Figure 2.3. In an ideal case, each electron injected above threshold will generate the same number of photons N as the number of periods N which leads to an optical power proportional to N. As shown in Figure 2.3, one period of a quantum cascade structure consists of an active region where population inversion and gain takes place followed by a relaxation-injection region. The latter one is formed by a chirped superlattice. When the appropriate electric field is applied to the structure (typically $50 - 80$kV/cm), carriers are injected by resonant tunnelling from the injection-relaxation region into the upper state of the lasing transition of the next period.[1] The electrons then lose their energy by emitting a photon or by a scattering mechanism involving the emission of an optical phonon. This process is the main non-radiative channel, and limits the lifetime of the upper laser level to typically 1 to several picoseconds (ps). The electrons are then extracted from the lower state of the active region and are further injected into the next period. Therefore, each electron can potentially generate the same number of photons as the number of periods. Typically, QCLs emitting in the

[1] Further readings on the design of the injector can be found in Ref. [56]

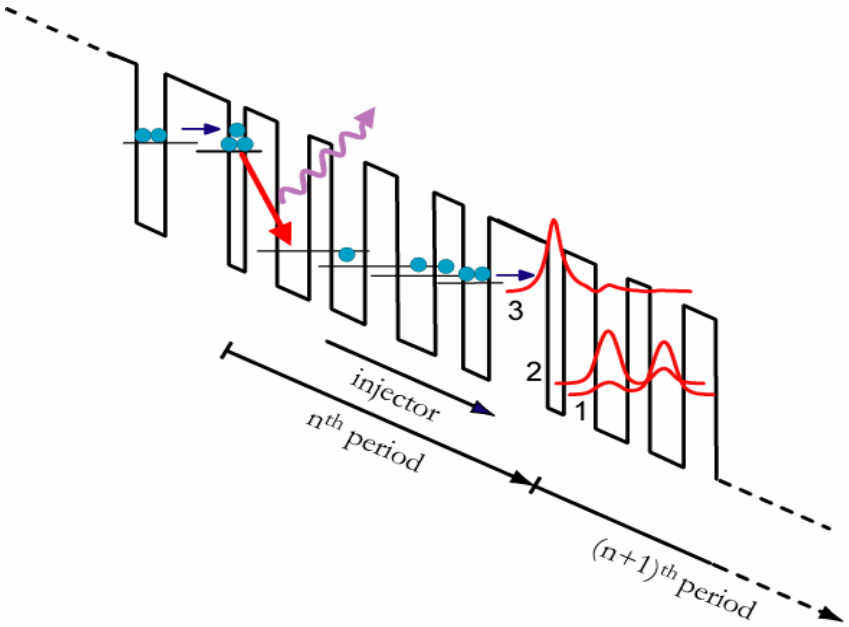

Figure 2.3: Biased electronic bandstructure corresponding to the active region of the first QCL based on a three QWs design. The squared moduli of the relevant wavefunctions are displayed. The red arrow represents the laser transition between states 3 and 2. Note that the injector in the present figure consists of only of two QWs for clarity and to keep the drawing to a reasonable size. Typically this part of the structure is composed by 4 to 10 QWs.

mid-infrared consist of 30 identical periods.
An important aspect in the design of QCLs is the lifetime engineering. As the population inversion between subbands in quantum cascade lasers does not come from an intrinsic property of the material (as for interband lasers), it is important to know and to design the different scattering times involved in intersubband transitions. The active region of the first QCL [1] for example consists of a three levels system comprising the ground state (labelled "1", "2" and "3" on Fig. 2.3.) of two thick and one thinner neighboring QWs. Lasing occurs between the states 3 and 2 and the upper state lifetime is estimated to be 4.3ps for an energy separation of 295meV. By design, the energy separation E_{21} equals the energy of an optical phonon (34meV in InGaAs/InAlAs materials) having the effect of depleting very efficiently the state 2. The relaxation time τ_{21} is as short as 0.6ps, insuring the build up of population inversion. Reason for the small lifetime of the state 2 compared to state 3 is the small momentum exchanged in transitions at energies close to the optical phonon energy which is proportional to the state lifetime. A detailed summary and discussion of the lifetime engineering can for example be found in [35].

2.2.1 Applications for Quantum Cascade Lasers

QCLs have many potential applications as they are nowadays the most convenient infrared light sources available. They are indeed very compact and can operate at room

temperature in pulsed [57] or continuous mode [52]. Their emission wavelength covers the entire mid-infrared, from 3.4 to 24μm and this range has recently been extended to the far-infrared [53]. At any of these wavelengths, Distributed Feedback (DFB) lasers can be fabricated. They are particularly well-suited for spectroscopy as their emission spectrum is single mode and has an extremely narrow linewidth [58], [59]. Moreover it is possible to easily match very specific frequency by tuning the voltage applied to the structure or the heat-sink temperature. The high output powers necessary for commercial applications are nowadays achievable. In pulsed mode, hundreds of milliWatts (average) can be easily obtained from single devices on Peltier cooler. Devices capable of cw operation can produce up to 10 milliWatts at room temperature.
Other infrared light emitters exist but are usually not as convenient as QCLs. Among other examples of infrared lasers, one can cite the CO_2 lasers which are used for metal cutting or manufacturing machines as they can produce easily 100 W in continuous-wave operation. However, their emission spectrum consists of many discrete lines ranging from 9.2 to 10.8μm which are not easily tunable. The applications of CO_2 lasers for mid-infrared spectroscopy are restricted to a rather narrow spectral range. Interband lasers based on low bandgap materials such as lead-salt [2] and antimonide [3] lasers have also been demonstrated in a wide spectral range, roughly from 1.9 to 30μm. Most of them can not operate at room-temperature and have low output power. In the far-infrared, p-Ge lasers can emit radiation between 70 and 300μm. Crossed electric and magnetic fields are usually required as these lasers rely on radiative transitions between heavy and light-hole cyclotron resonances in weakly p-doped Ge [5]. It has been demonstrated recently that strain can also replace the large magnetic field [60]. Despite this progress, p-Ge lasers are still not very convenient to use because of their size, their low operating temperature and their weak output power which can not be obtained in cw.
Infrared spectroscopy is so far the most important application of QCLs because most molecular gases have their fundamental vibrational modes in the mid-infrared region spanning approximately from 3 to 15μm. The corresponding absorption lines are very strong, allowing very sensitive chemical detection to be performed, with sensitivities down to below part per billion. Quantum cascade lasers and in particular distributed feedback QC lasers are well suitable for such applications. The usual techniques employed for gas-sensing is photoacoustic spectroscopy [61], [62] or direct absorption measurement[63], [64]. The high transparency of the atmosphere in the two windows of the atmosphere (approximately $3-5\mu$m and $8-12\mu$m) allows precise remote sensing and detection of dangerous gases such as ammonium and carbon monoxide.
Further important applications for high performance quantum cascade lasers are in the field data transmission [65]. In contrast to fiber optical telecommunications, this technique has the advantage of not requiring additional cables to be buried in the ground. Such free-space optical data links could therefore be particularly convenient in urban areas. QC lasers emitting in the transparent windows of the atmosphere (around 5 and 10μm) are very suitable for such applications. Light in the mid-infrared can indeed propagate even in bad weather conditions such as fog as the Rayleigh scattering is strongly reduced at theses wavelengths. The latter are much larger than the diameter of water

drops in clouds ($\sim 1\mu$m). Moreover, because of the very short intersubband lifetimes, the devices can be modulated in principle up to Terahertz frequencies [65], [66]. This is more than one order of magnitude faster than the speed achievable with interband lasers. Data have been successfully transmitted over a distance of 70m at a frequency of 5GHz. A similar experiment performed between two different buildings separated by about 350m has also been recently reported. In the latter investigations, a Peltier-cooled QC laser and a room-temperature HgCdTe detector were used [67].

Chapter 3

Theory

In this chapter, an overview over the properties of Si and Ge as well as the SiGe alloy will be given. The first part will be a discussion on the lattice structure of the group IV elements including the bandstructure. As the SiGe structures employed in this work are all p-type, the details of the valence band structure will be discussed. The Luttinger-Kohn formalism is presented which allows to take into account six valence bands and the interaction with remote bands. As the lattice constant between Si and Ge shows a mismatch of 4%, the effects of strain will be considered for the SiGe heterostructures. Furthermore, the band lineup at the interfaces Si/SiGe is discussed which forms the QW structure. The formalism to calculate the energy states and wavefunctions of the bound states in the QW is presented. From this, the optical matrix elements of intersubband transitions and the resulting selection rules will be given. The calculation of the absorption coefficient is explained. Finally, the impact of the specific properties of the SiGe system on the realization of the SiGe QC structures is discussed.

3.1 Si and Ge Crystal

Silicon and germanium are group IV elements in the periodic table of elements. Therefore, each atom has four valence electrons which are arranged in atomic shells: 3s2, 3p2 in Si and 4s2, 4p2 in Ge. The valence atoms form sp3 hybrid states which lead to four equivalent atomic bonds between nearest neighbor atoms. Hence, each atom in a crystal is bound to four neighbors arranged at the corners of a regular tetrahedron. This corresponds to the primitive cell of the so-called diamond lattice as shown in Figure 3.1. Silicon has a lattice constant of 5.43Å while the germanium lattice constant is 5.567Å. This results in a large lattice mismatch of 4.2% which is the reason for a number of effects as describe in the following section. For a $Si_{1-x}Ge_x$ alloy, one can use in a first approximation a linear fit between the lattice parameters of Si and Ge. A better fit to the experimental values is given by $a(Si_{1-x}Ge_x) = 0.002733x^2 + 0.01992x + 0.5431\text{nm}$. A detailed review can for example be found in [68]-[71]. For the doping of the SiGe layers, group III or V elements are either ion implanted or incorporated during growth [72]. For n-type doping,

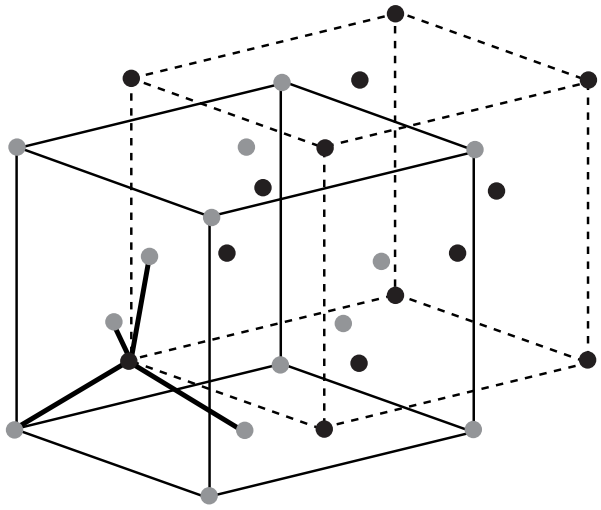

Figure 3.1: Schematic drawing of the diamond lattice. The unit cell consists of two face centered cubic lattices (fcc) which are displaced a quarter of the space diagonal with respect to each other. For clarity, one of the cells is plotted with dashed lines and open circles. The bonds between nearest-neighboring atoms are drawn for one point forming a tetradron. This corresponds to the primitive unit cell of the diamond lattice.

phosphorus and antimony is commonly used. In that repsect, it has to be mentioned that these elements have the tendency to segregate on the growing surface of the epitaxial layer which makes the doping profile of n-type SiGe layers hard to control. For the doping of p-type structures as used within the frame of this work, boron is the most preferred dopant.

In Figure 3.2, the band structure of Si and Ge is shown. The maximum of the valence band is situated at the Γ-point (Brioullion zone center at $k = 0$) and is fourfold degenerate as two spin-degenerated bands referred to as heavy- and light-hole bands (HH and LH) are formed. The degeneracy between HHs and LHs is lifted for nonzero values of the wavevector k. Furthermore, the so-called split-off bands downshifted of about 44meV need to be taken into account for a complete description of the valence band. As the valence band can not be described by a simple parabolic band formalism, a more correct treatment as given in section 3.2 is required.

In Si, the minimum of the conduction band (also called Δ) is situated along the ⟨100⟩ direction near the X point. In Germanium, the lowest conduction band is located at the L point along the ⟨111⟩. Both materials are thus indirect band gap materials with a band gap energy of 1.17eV and 0.78eV for Si and Ge, respectively. The direct band gap of Si is 3.4eV while it is 0.84eV for Ge. The band alignment between Si and SiGe crystals is of type II, with holes localized in the Ge-rich semiconductor and electrons in the Si [73].

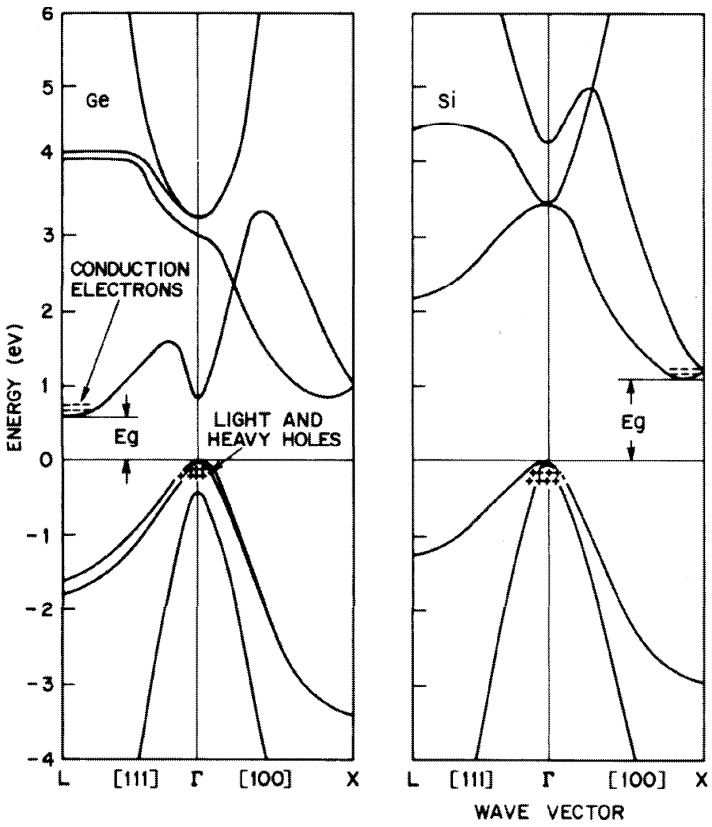

Figure 3.2: Bandstructure for the indirect bandgap materials germanium (a) and silicon (b) taken from [74]. Electrons and holes are schematically drawn at the minimum of the conduction and the maximum of the valence band. The top of the valence band is taken as common reference.

3.2 Valence band Structure

The knowledge of the band structure is essential for the understanding of the optical properties of a semiconductor. The energy bands and wavefunctions have to be calculated in an appropriate way. By knowing the initial and final states of the carriers which contribute to an optical transition, one can calculate e.g. absorption and gain using Fermi's golden rule. As the SiGe structures in this work are p-type, one needs to consider the valence band which is much more complex than the conduction band. At the Γ point, the valence band consists of three spin degenerated bands: The heavy hole, light hole and split off band. A proper theoretical treatment requires to take into account the six bands including the coupling to the remote bands. For this, the Luttinger-Kohn model is the appropriate approach in which the remote bands ar included via a second order perturbation. Furthermore, the spin-orbit interaction is taking into account. In the following, first the $\mathbf{k} \cdot \mathbf{p}$ model for single band will be briefly summarized and in the following applied in the Luttinger-Kohn model as well as for spin-orbit interaction.

3.2.1 $\mathbf{k}\cdot\mathbf{p}$ model for a single band

For the discussion, we focus on the valence band structure near the band edge which can be described by the $\mathbf{k}\cdot\mathbf{p}$ model. The $\mathbf{k}\cdot\mathbf{p}$ method was first introduced by Bardeen [75] and Seitz [76] and then applied to bulk and QW seminconductors [77]-[80].
When an electron in a periodic potential $V(\mathbf{r}) = V(\mathbf{r}+\mathbf{R})$ is considered, the electron wave function $\Psi(\mathbf{r})$ describing the motion of the electron through the crystal satisfies the Schrödinger equation:

$$\mathcal{H}\Psi(\mathbf{r}) = \left[\frac{\mathbf{p}^2}{2m_0} + V(\mathbf{r})\right]\Psi(\mathbf{r}) = E\Psi(\mathbf{r}) \tag{3.1}$$

where m_0 is the free electron mass. The quantities in the above equation are all periodic functions of the basis vector in the Bravais lattice and therefore, the function $\Psi(\mathbf{r}+\mathbf{R})$ will only differ from $\Psi(\mathbf{r})$ by a constant. This gives the general solution of Equation 3.1 as $\Psi_{n,\mathbf{k}}(\mathbf{r}) = u_{n,\mathbf{k}}(\mathbf{r})e^{i\mathbf{kr}}$ for the band of index n and the wave vector $\mathbf{k}$ with $u_{n,\mathbf{k}}$ as periodic function. This result is the Bloch theorem with $\Psi(\mathbf{r})$as Bloch function. Using this in the Schrödinger equation, one obtains:

$$\left[\frac{p^2}{2m_0} + \frac{\hbar}{m_0}\mathbf{k}\cdot\mathbf{p} + \frac{\hbar^2k^2}{2m_0} + V(r)\right]u_{n,k}(r) = E_n(k)u_{n,k}(r) \tag{3.2}$$

In the following, we consider a band structure near a single band (e.g. the band edge of a conduction band) and negligible coupling to neighboring bands (so-called remote bands). Then the second order perturbation theory gives for the eigenvalues of the energy (obtained from Eq. 3.2):

$$E_n(k) = E_n(k=0) + \frac{\hbar^2k^2}{2m_0} + \frac{\hbar}{2m_0}\mathbf{k}\cdot\mathbf{p}_{nn} + \frac{\hbar^2k^2}{2m_0}\sum_{n'\neq n}\frac{|\mathbf{k}\cdot\mathbf{p}_{nn'}|^2}{E_n(\mathbf{k}=0) - E_{n'}(\mathbf{k}=0)} \tag{3.3}$$

where the momentum matrix elements are defined as $\mathbf{p}_{nn'} = \int\limits_{unitcell} u^{\star}_{n,0}(r)\mathbf{p}u_{n',0}(r)d^3r$. If $E_n(\mathbf{k})$ has a maximum at the Γ point $k=0$, then $\mathbf{p}_{nn}$ must vanish and the energy band is parabolic as obtained from the effective mass theory. Therefore, eq. 3.3 can be rewritten as:

$$E_n(\mathbf{k}) = E_n(\mathbf{k}=0) + \sum_{\alpha\beta}D^{\alpha\beta}\mathbf{k}_\alpha\mathbf{k}_\beta = E_n(\mathbf{k}=0) + \frac{\hbar^2}{2m_0}\sum_{\alpha\beta}\left(\frac{1}{m^\star}\right)_{\alpha\beta}\mathbf{k}_\alpha\mathbf{k}_\beta \tag{3.4}$$

with $\alpha,\beta = x,y,z$ and

$$D^{\alpha\beta} = \frac{\hbar^2}{2m_0}\delta_{\alpha\beta} + \frac{\hbar^2}{2m_0}\sum_{n'\neq n}\frac{\mathbf{p}^\alpha_{nn'}\mathbf{p}^\beta_{n'n} + \mathbf{p}^\beta_{nn'}\mathbf{p}^\alpha_{n'n}}{E_n(\mathbf{k}=0) - E_{n'}(\mathbf{k}=0)} \tag{3.5}$$

The matrix $D^{\alpha\beta}$ is symmetric in the quadratic form and represents the inverse effective mass in matrix form multiplied by $\hbar/2$.

3.2.2 6-band k · p model

To expand the single band model to a complete description of the valence band, spin-orbit coupling as well as the three spin-degenerated bands are taken into account. An overview of this treatment is given in the following.

Spin-orbit interaction

The spin-orbit interaction results (in a qualitative description) from a relativistic effect: The electron crosses the electrostatic potential at high speed. In the electron frame of reference, the electric field associated with this potential transforms into a magnetic component which in turn interacts with the electron spin. The electron motion and spin become decoupled and the spin operator no longer commutes with the Hamiltonian which results in a splitting of the levels. This spin-orbit interaction is described by

$$\frac{e^2}{m_0^2 c^2 r^3}\mathbf{L}\cdot\mathbf{S} = \frac{1}{4m_0^2c^2}(\sigma \times \nabla V(r))\cdot\mathbf{p} \tag{3.6}$$

where σ, $\mathbf{L}$ and $\mathbf{S}$ are the Pauli spin matrices, the angular momentum and the spin operators, respectively. When the spin-orbit interaction is included, another set of basis functions is usually chosen in which the term 3.6 is diagonal. As the wave functions near the top of the valence band are p-symmetrized, the eigenvalues of the total angular momentum $j = l \pm s$ are $l = 1$ and $s = 1/2$ as every electron carries the spin 1/2. This leads to a doublet with $j = 1/2$ and a quadruplet with $j = 3/2$. The set of basic functions expressed by $u_{n0}(\mathbf{r}) = |j, m_z\rangle$ with the quantum number m_z can also be presented as a linear combination of the functions $|X\rangle$, $|Y\rangle$ and $|Z\rangle$. The latter ones are the spin-degenerated functions $|X\rangle = xf(\mathbf{r})$, $|Y\rangle = yf(\mathbf{r})$ and $|Z\rangle = zf(\mathbf{r})$ where $f(r)$ is an even function of r. The basic functions for the description of the valence band are given in Table 3.1.

Denomination	j and m_j basis	$\|X\rangle$, $\|Y\rangle$, $\|Z\rangle$ basis
Heavy hole (HH)	$\|3/2, 3/2\rangle$	$-1/\sqrt{2}\|(X+iY)\uparrow\rangle$
Light hole (LH)	$\|3/2, 1/2\rangle$	$-1/\sqrt{6}\|(X+iY)\downarrow\rangle + \sqrt{2}/\sqrt{3}\|Z\uparrow\rangle$
Split-off band (SO)	$\|1/2, 1/2\rangle$	$1/\sqrt{3}\|(X+iY)\downarrow\rangle + 1/\sqrt{3}\|Z\uparrow\rangle$

Table 3.1: Expression of the valence bands basis functions. Only the eigenvectors having a positive value for m_j are given for clarity. The constants in the right column are given by the multiplication of the Clebsch-Gordon coefficients for the composition of an angular momentum $l = 1$ and a spin 1/2 together with the factors expressing the angular momentum functions.

Luttinger-Kohn's model

The Schrödinger equation for the complete Bloch wave function including the above discussed spin-orbit interaction is given by:

$$\mathcal{H}\Psi(\mathbf{r}) = \left[\frac{\mathbf{p}^2}{2m_0} + V(\mathbf{r}) + \frac{\hbar}{4m_0^2c^2}(\nabla V \times \mathbf{p})\cdot\sigma\right]\Psi(\mathbf{r}) = E(\mathbf{k})\Psi(\mathbf{r}) \tag{3.7}$$

Using the Bloch theorem, the lattice-periodic basis functions discussed in the previous section are introduced. They are expanded into linear combinations of six zone-center Bloch functions of the hole bands and the remote bands. The six bands are treated exactly whereas the remote bands are included via a second order perturbation. The coupling of the basic functions to the remote bands is then removed by $\mathbf{k}\cdot\mathbf{p}$ perturbation theory. This gives the 6×6 matrix Schrödinger equation:

$$\sum_{j'=1}^{6} H_{jj'}^{LK}(\mathbf{k})a_{j'}(\mathbf{k}) = E(\mathbf{k})a_j(\mathbf{k}) \tag{3.8}$$

where the Luttinger-Kohn hamiltonian $\mathcal{H}^{LK}$ reads:

$$\mathcal{H}_{jj'}^{LK} = E_j(\mathbf{k}=0)\delta jj' + \sum_{\alpha\beta} D_{jj'}^{\alpha\beta}k_\alpha k_\beta \tag{3.9}$$

The matrix $D^{\alpha\beta}(\alpha,\beta) = (x,y,z)$ represents the nondiagonal elements of the LK Hamiltonian caused by the interaction with remote bands and has the nature of an inverse effective-mass tensor:

$$D_{jj'}^{\alpha\beta} = \frac{\hbar^2}{2m_0}\delta_{jj'}\delta_{\alpha\beta} + \frac{\hbar^2}{2m_0}\sum_{\xi}\frac{\mathbf{p}_{j\xi}^{\alpha}\mathbf{p}_{\xi j'}^{\beta} + \mathbf{p}_{j\xi}^{\beta}\mathbf{p}_{\xi j'}^{\alpha}}{E_j(\mathbf{k}=0) - E_{j'}(\mathbf{k}=0)} \tag{3.10}$$

The explicit form of the hamiltonian $\mathcal{H}^{LK}$ (6x6 matrix for 6 bands) is given by:

$$\mathcal{H}_{LK} = -\begin{pmatrix} P+Q & -S & R & 0 & -S/\sqrt{2} & \sqrt{2}R \\ -S^\star & P-Q & 0 & R & -\sqrt{2}Q & \sqrt{3/2}S \\ R^\star & 0 & P-Q & S & \sqrt{3/2}S^\star & \sqrt{2}Q \\ 0 & R^\star & S^\star & P+Q & -\sqrt{2}R^\star & -S^\star/\sqrt{2} \\ -S^\star/\sqrt{2} & -\sqrt{2}Q^\star & \sqrt{3/2}S & -\sqrt{2}R & P+\Delta & 0 \\ \sqrt{2}R^\star & \sqrt{3/2}S^\star & \sqrt{2}Q^\star & -S/\sqrt{2} & 0 & P+\Delta \end{pmatrix} \tag{3.11}$$

where

$$P = \frac{\hbar^2}{2m_0}\gamma_1(k_x^2+k_y^2+k_z^2) \tag{3.12a}$$

$$Q = \frac{\hbar^2}{2m_0}\gamma_2(k_x^2+k_y^2-2k_z^2) \tag{3.12b}$$

$$R = -\frac{\sqrt{3}\hbar^2}{2m_0}\left[-\gamma_2(k_x-ik_y)^2 + 2i\gamma_3 k_x k_y)\right] \tag{3.12c}$$

$$S = \frac{\sqrt{3}\hbar^2}{m_0}\gamma_3(k_x-ik_y)k_z \tag{3.12d}$$

Here, Δ is the spin-orbit splitting and m_0 the free electron mass and γ_1, γ_2 and γ_3 are the so-called Luttinger parameters which describe the influence of the remote bands on the valence band. The following remarks should be noted about the LK Hamiltonian:

1. the Luttinger parameters γ can be expressed with the momentum matrix elements $p_{nn'}$ and calculated. However, they are usually considered as empirical parameters and their values are deduced from cyclotron resonance experiments, see Ref. [81].

2. Δ is the spin-orbit splitting, which lifts the degeneracy between the HH/LH and the SO bands. Indeed $\mathbf{L}\cdot\mathbf{S}$ can be rewritten $\mathbf{L}\cdot\mathbf{S} = 1/2(j^2 - l^2 - s^2)$ and is different if $j = 3/2$ (HH/LH bands) or $j = 1/2$ (SO band). Note that the influence of the SO band can not be neglected in particular in bulk Si, as the spin-orbit splitting is only 44meV.

3. as in the case of the single band problem, the matrix $D^{\alpha\beta}$ determines the effective mass and totally depends on the coupling of the band n with neighboring bands. In the case of a $Si/Si_{0.2}Ge_{0.8}$ QW, the effective masses take the following values: HH $m^\star_\perp = 0.215$, $m^\star_{//} = 0.079$ LH $m^\star_\perp = 0.091$, $m^\star_{//} = 0.148$. After Ref. [81].

4. for $k_x, k_y = 0$, the factors R and S vanish. The non-diagonal elements involving the HH bands in 3.11 are as a consequence equal to zero. The latter band remains in that case completely decoupled from the others, which are mixed even at vanishing $k_{//}$. On the contrary all the bands are coupled whenever the value of the momentum is non-negligible. This fact has a particular importance in many physical processes

A more detailed discussion on this matrix can be found e.g. in [82] and [83].

3.2.3 Strain Effects

For Si and Ge, a lattice mismatch of 4.2% exists. Strain is introduced in a SiGe system when for example a $Si_{1-x}Ge_x$ laxer is grown on a $Si_{1-y}Ge_y$ substrate with $x \neq y$. The larger lattice constant of Ge results in a compressive (tensile) strain when less (more) germanium than in the substrate is incorporated in the SiGe layer: In order to minimize the total energy of the crystal (including binding and strain energy), the grown layer adjust itself to the substrate leaving the lattice constant of the substrate plane virtually unchanged. Figure 3.3a and b shows the situation for a compressively strained SiGe layer. The resulting strain leads to a tetragonal distortion of the unit cell. Since this causes both, a volume change of the primitive cell and an in-plane change of interatomic distance, the effects on the valence band structure can be modelled by separating into hydrostatic and uniaxial strain [84].

The hydrostatic strain corresponds to a fractional volume change of the unit cell and results in a uniform shift of all valence bands: $\epsilon_{hydr} = a_\nu \frac{\Delta V}{V}$. The change of volume is directly expressed by the strain components parallel and perpendicular to the growth direction (see also Fig. 3.3c) $\frac{\Delta V}{V} = 2\epsilon_{//} + \epsilon_\perp$ and a_ν is the hydrostatic deformation potential ($a_\nu(Si) = 2.46, a_\nu(Ge) = 1.24$). For the description of the volume change, the strain in the direction parallel $\epsilon_{//}$ to the growth direction is expressed as: $\epsilon_{//} = \frac{a_l - a_s}{a_s}$ where the lattice constant of the substrate and the epitaxial layer are given by a_s and a_l. The strain component perpendicular to the growth direction $\epsilon_\perp$ is related to $\epsilon_{//}$ through the Poisson

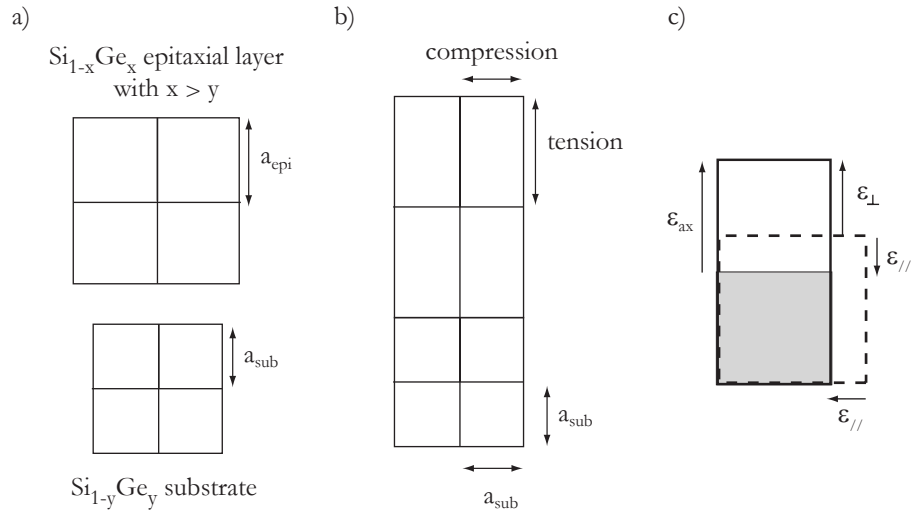

Figure 3.3: a)Schematic representation of two free standing Si_xGe_x and Si_yGe_y crystals. The latter are represented by cubic lattices for simplicity. b) Situation when the Si_xGe_x layer is grown on a Si_yGe_y crystal. c) Decomposition of the effects of the strain into either the components $\epsilon_\perp$ and $\epsilon_{//}$ solid line) or ϵ_{hydr} and ϵ_{ax}. The isotropic dimension change accounted by ϵ_{hydr} is represented by a grey square. The dashed line shows the unstrained lattice.

ratio: $\epsilon_\perp = -\frac{2\sigma}{1-\sigma}\epsilon_{//} = -\frac{2C_{12}}{C_{11}}\epsilon_{//}$. Here σ is the Poisson's ratio[1]. As the change of volume does not alter the symmetry of the crystal, no additional band degeneracies are expected from the hydrostatic strain.
The uniaxial strain is originating from the in-plane change of interatomic distances and results in a splitting of the valence band degeneracy at $k = 0$ as it breaks the symmetry of the unit cell along the z-direction. Therefore, it affects the HH, LH and SO bands differently depending on their symmetry (see Table 3.1) and due to this the degeneracy of the heavy- and light-hole bands at the Γ point is lifted and light-hole and split-off bands even mix at $k_{//} = 0$ [71], [83]. The uniaxial strain is given by $\epsilon_{ax} = \epsilon_\perp - \epsilon_{//}$.
The relative shifts of the valence bands along the (100) axis at $k_{//} = 0$ including strain and spin orbit interaction Δ are given by [84]:

$$\Delta E_{HH}(\mathbf{k}=0) = -\delta E_{hydr} - \frac{\delta E_{ax}}{2} \tag{3.13a}$$

$$\Delta E_{LH}(\mathbf{k}=0) = -\delta E_{hydr} + \frac{1}{2}(\delta E_{ax} - \Delta + \sqrt{\Delta^2 + \Delta\delta E_{ax} + 9/4\delta E_{ax}^2}) \tag{3.13b}$$

$$\Delta E_{SO}(\mathbf{k}=0) = -\delta E_{hydr} + \frac{1}{2}(\delta E_{ax} - \Delta - \sqrt{\Delta^2 + \Delta\delta E_{ax} + 9/4\delta E_{ax}^2}) \tag{3.13c}$$

For vanishing stress, the LH and HH bands are degenerate and raised by an energy corresponding to the spin-orbit coupling Δ with respect to the SO band (see section 3.2.2). Note that the valence band edge can be either HH- or LH-like, depending on the sign of

[1]For the (100) crystal orientation the Poisson's ratio is given by $\sigma = c_{11}/(c_{11}+c_{12})$ and the elastic stiffness constants of Si and Ge are $c_{11}(Si) = 165.8\text{MPa}, c_{12}(Si) = 63.9\text{MPa}, c_{11}(Ge) = 128.5\text{MPa}, c_{12}(Ge) = 48.3\text{MPa}$ For the SiGe alloy one can assume linear approximation between these values.

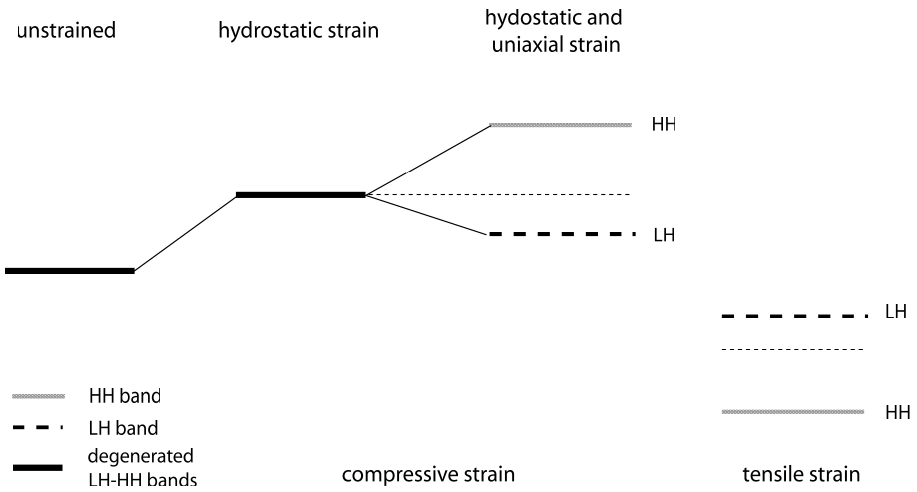

Figure 3.4: Illustration of the effect of strain on the band lineup of the HH and the LH bands. The SO band is omitted together with the effect of the spin-orbit coupling. Hydrostatic strain shifts the average energy position of the bands while their degeneracy is lifted by uniaxial strain.

ϵ_{ax} as shown in Figure 3.4.

The thickness of the grown SiGe layer can not be infinite: The thicker the epitaxially grown layer is, the more strain energy will be stored in the crystal. When a critical thickness is reached, the formation of dislocations becomes energetically favorable, leading to a relaxation of the crystal. As long as the thickness of the epitaxial layer is kept below the critical thickness, the growth is said to be pseudomorphic. Typical thicknesses of individual layers for a germanium content of 50% are about 10nm. A way to avoid the thickness limitations due to strain is the use of SiGe substrates. The latter ones allow to deposit successively layers under compressive and tensile strain compensating each other. The average elastic energy in the structure can therefore be reduced to zero by carefully choosing the thickness and the composition of each layer. This technique, called strain compensation is of course not possible for structures deposited on Si (100) substrates, since SiGe layers with only one sign of strain can be grown. For this reason the thick active region of SiGe QC emitters can only be realized on SiGe pseudosubstrate.

3.2.4 Band Offsets

Two materials brought together in a heterojunction will create discontinuities in the conduction and the valence band due to their different energies with respect to the vacuum potential. These band edge discontinuities are among the most essential parameters which are necessary to determine the intersubband properties of heterostructures.

As already mentioned in the first chapter, the discontinuity of the conduction band edge at the interface of unstrained bulk Si and Ge is rather small. Electrons can only be confined in a QW when strain is applied. From this, the need to work in the valence band arises. Therefore, the following discussion is focussed on the valence band.

A first model for the calculation of the band offsets was proposed by *Van de Walle* [84]: An absolute reference needs to be defined for the different semiconductor alloys. On this

basis, the average position of the three valence bands is calculated. The spin-orbit energy Δ is taken from experimental data, as well as the energy of the bandgap. Through this, the alignment for two unstrained materials can be obtained. By adding the corrections for the hydrostatic and uniaxial strain as given in eq. 3.13c, the values for the offsets are obtained. This procedure must be carried out for the different materials of the heterojunction and allows to derive the band lineups. Further details and examples can e.g. be found in [68], [47] and [85].

The valence band offsets calculated on the basis of the model of van de Walle and the

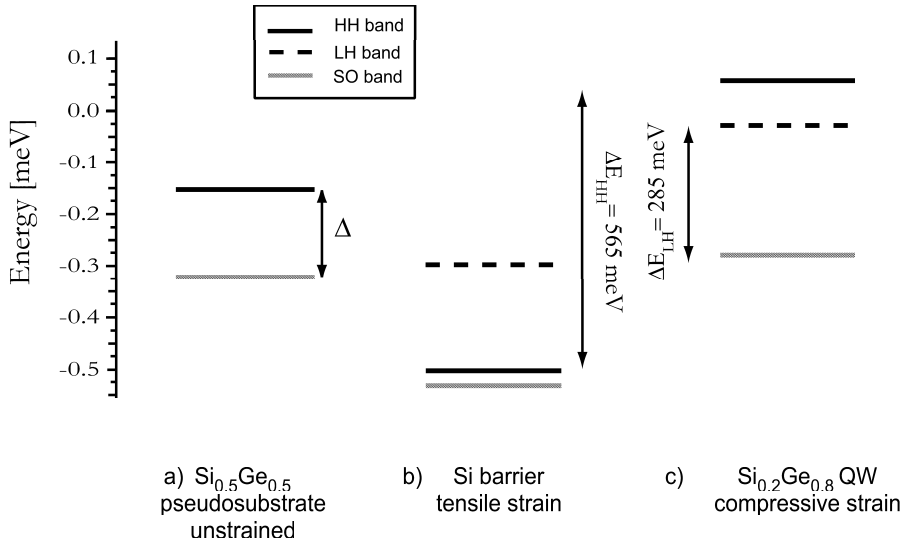

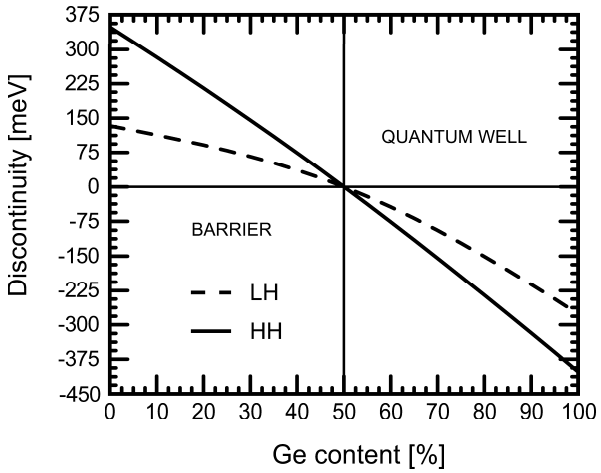

Figure 3.5: (a) Band alignment for a $Si_{0.5}Ge_{0.5}$ substrate. As the crystal is unstrained, the LH and the HH bands are degenerated and splitted from the SO band by an amount Δ. (b) Band alignment in the case of a Si layer grown on a $Si_{0.5}Ge_{0.5}$ substrate. (c) Band lineup for a $Si_{0.2}Ge_{0.8}$ layer grown on a a $Si_{0.5}Ge_{0.5}$ substrate. (d) HH and LH discontinuities as a function of the Ge content in the epitaxial layer. The effect of strain is included.

resulting band diagram is shown in Figure 3.5. Here, a common heterojunction composed of Si barriers and $Si_{0.2}Ge_{0.8}$ QWs grown on $Si_{0.5}Ge_{0.5}$ is shown. The heavy hole band

offset for that type of structure is $V_{HH} = 565$meV. The Si layer forms a barrier for holes. One finds that the barrier for heavy holes is higher than for light holes. By changing the Germanium content in the structure, different band offsets can be achieved as shown in Figure 3.5d.

3.2.5 Valence Band Structure in a QW

Finding the eigenvalues and eigenfunctions solution of the Schrödinger equation describing the motion of a particle in a QW is a classical problem of quantum mechanics. First the Schrödinger equation in the well and the barriers is solved. The wavefunction has the form of either propagating or evanescent plane waves. The eigenstates and the eigenvalues are found by solving the equation $\mathcal{H}\psi = E\psi$ and by imposing the continuity of the wavefunction and of the current probability $\frac{1}{m^\star}\frac{\partial \Psi}{\partial z}$ at both barrier/well interfaces. From the boundary conditions, discrete energy levels arise, corresponding to states confined in the QW. This problem and the way to solve it are very similar if a semiconductor QW is considered, except that the hamiltonian in the barriers and the well is given by the bulk Luttinger-Kohn hamiltonian $\mathcal{H}_{LK}$. Furthermore, the wavefunctions must account for both the rapidly varying potential describing the different bulk crystals, and the slowly varying potential due to the heterostructure. The latter only affects the motion of the carriers along the growth direction and therefore the wavefunctions are described by plane waves in the directions x and y, a set of 6 slowly varying functions of z $f_n(z)$ and the 6 Bloch functions $u_n(r)^m$, where the index m refers to either the barrier or the QW:

$$\psi^{(m)}(\mathbf{k}, r) = e^{i(\mathbf{k}_x x + k_y y)} \sum_{n=1}^{6} f_n(z) \cdot u_n^m(\mathbf{k}, r) \tag{3.14}$$

Usually the $u_n(r)^m$ are taken to be equal in the materials composing the barrier and the QW, limiting the validity of the method to semiconductors having similar chemical properties. As a consequence the difference of the crystals are fully accounted by the Luttinger parameters in the LK-hamiltonian. As in the classical one-band model for QWs, the confined states in the QW are fully determined by the effective mass equation $\mathcal{H}_{LK}\psi(\mathbf{k}, r) = E\psi(\mathbf{k}, r)$ in each semiconductor layer and the boundary conditions at each interfaces. The matrix corresponding to this system of coupled differential equations has to be diagonalized to find the solutions. A complete and exact treatment, including light and heavy hole bands for a single QW is presented in Ref. [86]. This method has been further extended to any heterostructure using a transfer-matrix approach [87], [88].
Another possibility for calculating the energy and the wavefunction of bound states in a heterostructure has been developed by *T.Fromherz* [71]. The basic idea is to consider that the structure is repeated infinitely, as in a crystal that would have a lattice constant L given by the sum of stack of QWs and barriers. This assumption allows to expand the envelope functions $f_n(z)$ in Fourier series by analogy with the Bloch functions:

$$f_n(z) = e^{ik_z z} \sum_p c_{n,k_z} e^{ipk_z z} \tag{3.15}$$

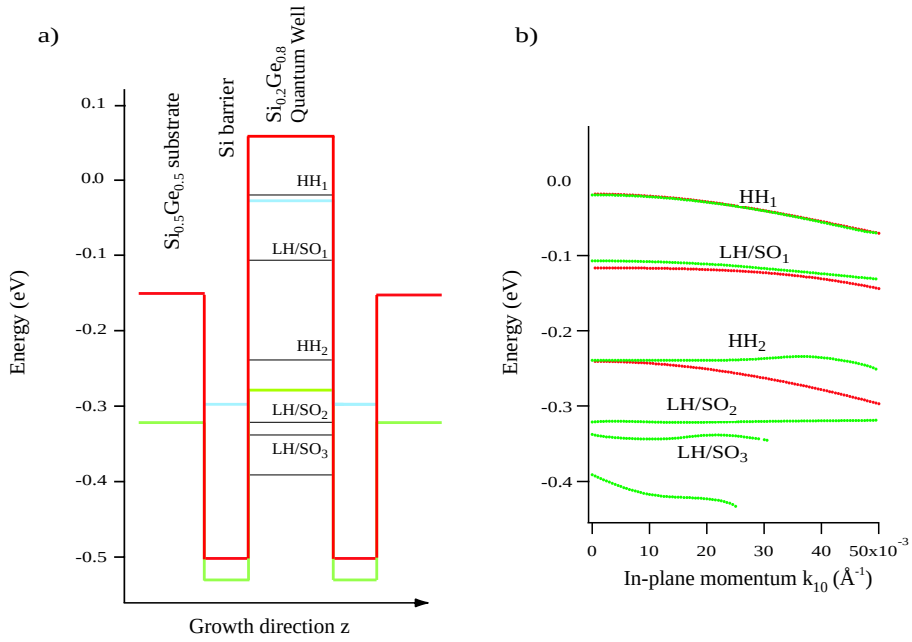

Figure 3.6: a) Band structure of a 35 Å $Si/Si_{0.2}Ge_{0.8}$ QW grown on $Si_{0.5}Ge_{0.5}$ substrate as calculated in the 6 band $\mathbf{k}\cdot\mathbf{p}$ transfer-matrix approach. The energy at $k = 0$ of each bound state is shown by a dashed line. The offsets are indicated with different colors, i.e. red, light blue and green for respectively the HH, the LH and the SO bands and can be read from Fig. **??**. b) Dispersion relations calculated by either a 4 (red curve) or a 6 (green curve) bands $\mathbf{k}\cdot\mathbf{p}$ models.

with $k_z = \frac{\pi}{L}$, $p = \pm1, \pm2,...$ and $|q| \leq \frac{\pi}{L}$. The boundary conditions expressed as $\psi(z+L) = e^{ik_zL}\psi(z)$, are automatically fulfilled with the choice of ψ. The coefficients c_{n,k_z} and the energies E_k are found from calculating the matrix elements of the LK hamiltonian and then determining the eigenvalues and eigenvectors. As can be seen on the example presented on Fig. 3.6a), the bandstructure of even a single p-type QW can be very complicated because of the confinement of many levels. Moreover the symmetry of the states is not well defined as they are a mixture of the three valence bands at $k \neq 0$. In particular the LH and the SO levels are coupled even for vanishing momentum (see section 3.2.2) and thus are usually referred to as LH/SO states. The effects of the strong bandmixing must be included in order to correctly determine the energy position for each subband. Neglecting this can lead indeed to non-negligible energy differences reaching tens of meV, in particular for LH and SO levels. Such discrepancies are clearly displayed on Fig. 3.6b), where the results of a 4 and a 6 band $\mathbf{k}\cdot\mathbf{p}$ model are shown. Dissimilar LH/SO_1 energies are indeed found at $k_{//} = 0$. A more much spectacular difference is the absence of the anticrossing between the LH/SO_1 and HH_2 levels in the predictions of the 4 bands model. The HH_1 and the LH/SO_1 levels are split at $k = 0$ due to the strain. Since the QW is under compressive strain, the ground state has a HH symmetry. It is important to note that when the QW width is such that the HH_1-HH_2 transition energy corresponds to a wavelength in the mid-infrared range, the strain is not large enough (or only in extremely strained layer which can be barely grown because of the critical thickness) to shift the

LH/SO_1 level above the the first excited HH level HH_2. This has significant consequences for the realization of a SiGe QC laser as the phonon scattering between HH and LH is very efficient, reducing substantially the lifetime of the HH_2.

3.3 Optical matrix elements and selection rules

In order to describe radiative transitions between two bound states i and j in a p-type QW, the optical matrix elements need to be calculated. The detailed procedure can be found in several publications and textbooks (e.g. [82], [71], [89] and [90]), in the following only the results will be explained and the selection rules given. Here, with respect to the references, we restrict ourselves to the treatment of HH and LH bands only, neglecting the spin orbit coupling.
When calculating optical transitions, one starts with Fermi's golden rule. The optical matrix elements are given by $\langle i|\epsilon \cdot \mathbf{p}|j\rangle$ in the dipole approximation and assuming $k_i = k_j$. The vector ϵ describes the direction of the electric field. By neglecting the spin-orbit interaction, the matrix elements of the momentum operator between the complete wave functions Ψ can be written as:

$$\left\langle \Psi_i|\frac{\hbar}{m_0}\epsilon \cdot \mathbf{p}|\Psi_j \right\rangle = \frac{\hbar}{m_0}\epsilon \cdot \mathbf{p_{i,j}} = \epsilon \cdot \sum_{m,n=1}^{4} (I_{mn}Q_{mn}^{ij} + J_{mn}R_{mn}^{ij}) \tag{3.16}$$

Q and R are the terms of the transition matrix elements p_{ij} and are obtained from the envelope functions $f_n^{i,j}(z)$ as follows:

$$R_{mn}^{ij} = \int_\Omega dz f_m^*(i, k_\perp, z)\Big(- \nu\frac{d}{dz}\Big) f_n(j, k_\perp, z)$$

where the index ν extends over the cartesian components and represents the dot product. Furthermore:

$$Q_{mn}^{ij} = \int_\Omega dz f_m^*(i, k_\perp, z) f_n(j, k_\perp, z)$$

where Ω is the volume of the crystal. These terms of the momentum matrix element p_{ij} written in a matrix which contains the Luttinger parameters, define the selection rules. One can distinguish two types of contribution to an optical transition:

- Terms containing the dipole matrix element of the envelope function R^{ij}: Only optical transitions between two levels having a different parity are allowed at $k_\perp$ as given by the dipole moment. Moreover the light must polarized along the growth direction z (so-called transverse-magnetic or TM polarization) since the two envelope functions are only dependant on z. This selection rule, valid for both HH-HH and LH-LH transitions is analogous to the situation occurring between subbands in the conduction band. LH-HH transitions are also allowed, but only in the opposite polarization (so-called transverse-electric or TE polarization). The explanation for the latter point is not straightforward and will therefore not be given here. For further details the reader is referred to Ref. [82].

- Terms containing Q^{ij}: These contributions do not vanish if both envelope functions $f_n^{i,j}(z)$ have the same parity. As they are proportional to $k_\perp$, transitions are only allowed

at $k \neq 0$. Hence, transitions between all the subbands in the x-y directions and only LH-HH transitions in the z polarization. These contributions are proportional to $k_{//}$ and their origin come from the coupling to the remote bands.

The matrices describing the polarization selection rules are not shown here for the sake of brevity but can be found in various references [89], [90], [82]. Note that they are somewhat similar to the Luttinger-Kohn hamiltonian $\mathcal{H}^{LK}$ because of the analogy between the operators $\epsilon \cdot \mathbf{p}$ and $\mathbf{k} \cdot \mathbf{p}$. An excellent illustration is given in Ref. [82], p. 71. In Table 3.2 the selection rules for transitions occurring between the first levels of the HH and LH bands are summarized. Terms containing the index k are proportional to the in-plane wave vector, i.e. the matrix element of the corresponding transition is zero at k=0 and the transition therefore forbidden at vanishing k. At higher k values, the optical matrix element becomes stronger and the transition is allowed. Transition terms without index are allowed at all k in the either TM or TE polarization.

From the optical matrix elements, the 2D absorption coefficient can be obtained:

	HH_1	LH_1	HH_2	LH_2	HH_3
HH_1	-	TE_k/TM_k	TM	TE	TE_k
LH_1	TE_k/TM_k	-	TE	TM	TE_k/TM_k
HH_2	TM	TE	-	TE_k/TM_k	TM

Table 3.2: Polarization selection rules for the intersubband transitions possible between the first few HH and LH states confined in a p-type square QW. The index k indicates when the optical matrix element is proportional to the in-plane momentum k.

$$\alpha_{2D} = \frac{\pi e^2}{\epsilon_0 c n \omega m_0^2 A} \sum_{i,j} \sum_{k} |\epsilon \cdot \mathbf{p_{ij}}(k_\perp)|^2 \cdot [f(E_i(k_\perp)) - f(E_j(k_\perp))] \cdot \frac{\Gamma/\pi}{[E_i(k_\perp) - E_j(k_\perp) - \hbar\omega]^2 + \Gamma^2} \tag{3.17}$$

In the calculations presented in Chapter 8, the absorption between two subbands i and j is characterized by the differential cross section σij which is connected to the $3D$ absorption coefficient as:

$$\alpha_{3D}[cm^{-1}] = \sigma_{ij} \frac{N_S}{L}$$

where N_S is the sheet carrier density and L the quantum well width. The differential cross section for the transition $i \rightarrow j$ at the wavelength ω_{ij} expressed with the fine structure constant α_0 can be written as:

$$\sigma_{ij} = \sum_k (\frac{4\pi\alpha_0}{n}) \frac{\hbar\omega_{ij}}{\Gamma_{ij}} \cdot \langle i|p_{ij}|j\rangle^2 \tag{3.18}$$

where Γ_{ij} is the linewidth of the transition and n the refractive index. The summation over the in-plane k vector gives the dispersion relations.

3.4 Conclusion for SiGe Quantum Well Structures

In this chapter, the basic properties of the SiGe system were discussed and theoretically described as far as of importance for the realization of an optically pumped SiGe quantum cascade laser. In conclusion, the main material and physical issues obtained from this will be summarized.

It is obvious that the strain induced by the mismatch of the lattice constant of Si and Ge is a stringent obstacle to the fabrication od Si/SiGe QC structures. A way to circumvent the resulting limitations is the strain compensated growth on SiGe pseudosubstrates. However, an interface quality and roughness comparable to similar III-V structures can not be achieved by this.

p-type heterostructures are the most convenient choice in the Si/SiGe material system. The conduction band may appear at first sight more attractive than the complicated valence band. Actually the bandstructure is complex in both cases, as mentioned in section 3.2.4 and 3.2.5. The properties of n-type multi-QW structures depend strongly on the different Δ and L valleys, whereas in the valence band one must take into account HH, LH and SO bands. However working with holes presents several advantages. The value of the bandoffset in the conduction band is in general smaller compared to the valence band. The effective mass of an electron can be more than four times larger than the value corresponding to the HH band. A heavy mass is usually a severe handicap since the oscillator strength between two states ($f_{ij} = \frac{2}{m^* \hbar \omega_{ij}} \left| \langle i | p_{ij} | j \rangle \right|^2$) is proportional to the inverse of this quantity. The transport of carriers through barriers, which is a crucial issue for QCLs, can also be strongly affected by a large tunnelling mass. Moreover, the physics of intersubband transitions between levels in the conduction band is not as well-characterized as for the valence band since much less experiments have been performed on n-type Si/SiGe heterostructures. It is also much more difficult to achieve an abrupt and well-controlled doping profile in Si with donors.

As a consequence of the above arguments, the combination of materials chosen for the development of optically pumped QC structures consists of p-type Si barriers and $Si_{1-x}Ge_x$ QWs. The germanium content was varied from 80% to 100% depending on the chosen design as described in chapter 8. The Ge content of the substrate was varied between 25% and 50% which determines the total amount of germanium allowed in the structure. The choice of substrate and germanium content of the wells defines the band offsets and is adapted regarding the design. Finally, for the realization of low loss optical waveguides, the gradient of Ge concentration and hence of the refractive index in the pseudosubstrates provides a suitable cladding layer for the confinement of the light.

Chapter 4

MBE growth and Characterization

The samples investigated and discussed within this work were grown by Molecular Beam Epitaxy (MBE). In this chapter, the principle of MBE growth will be described. Common characterization techniques of MBE grown structures like High Resolution Transmission Electron Microscope (HR-TEM) and X-Ray diffraction are discussed.

4.1 MBE growth

Within the last fifty years, constant progress in the growth of semiconductor crystals from a melt has been made. The growth of SiGe on pure Si was pioneered by *E.Kasper et al.* in the late 70's [91]. This opened the way towards new Si based heterostructures and the possibility to apply the principles of band structure engineering to the Si material system. For the SiGe depositions, two principles can be chosen: Chemical Vapor deposition (CVD) and MBE. The advantage of the MBE is the independent control of growth rate and substrate temperature which allows the growth of thin layers with sharp interfaces. Its basic requirements are discussed in the following:
The principle idea of an heteroepitaxial growth is to have an atomic beam directed towards a clean crystal surface on which the atoms are sticking in an ordered way, usually monolayer by monolayer. In the case of a Si-based MBE, this atomic beam is achieved by heating a source material with an electron beam yielding reasonable fluxes. The requirements for a suitable growth are very pure source materials as well as Ultra High Vacuum (UHV) $\leq 10^{-9}$mbar as any impurity will be incorporated in the crystal. Low pressure is also essential to produce a molecular beam which is only achieved when the mean free path of the electrons is longer than the distance between source and substrate. This would for example require a pressure of 10^{-4}mbar for a mean free path of 1m. Hence, the epitaxial restrictions are more stringent than the molecular beam conditions. Besides the pressure, the growth temperature is an essential parameter deciding about the quality of the grown structure. Low temperature (< 300°C) favors a higher density of point defects. Furthermore, the coverage of the surface with atoms from residual gases is increased at low temperature as the sticking coefficients are in the same range as for Si. With higher temperature however, the sticking coefficients of most gases are reduced while the one

of Si remains around one for the whole temperature range. This leads to an improved background impurity density at higher temperatures. The high temperature limit is defined by the diffusion of dopants and interdiffusion of interfaces which is enhanced at higher temperature due to the higher surface mobility of deposited atoms. Furthermore, high temperature assists the strain relaxation due to misfit dislocation and/or buckling of interfaces. Finally, the segregation of Ge atoms into Si layers is increased for higher temperature which smears out the interfaces. For those reasons, a trade off with respect to the growth temperature is necessary. For the QC structure, the tendency is towards lower growth temperature ($\sim 300 - 350°C$) as the relaxation for thick structures is the most critical point.

The MBE system employed for the growth of the structures discussed in this work is a

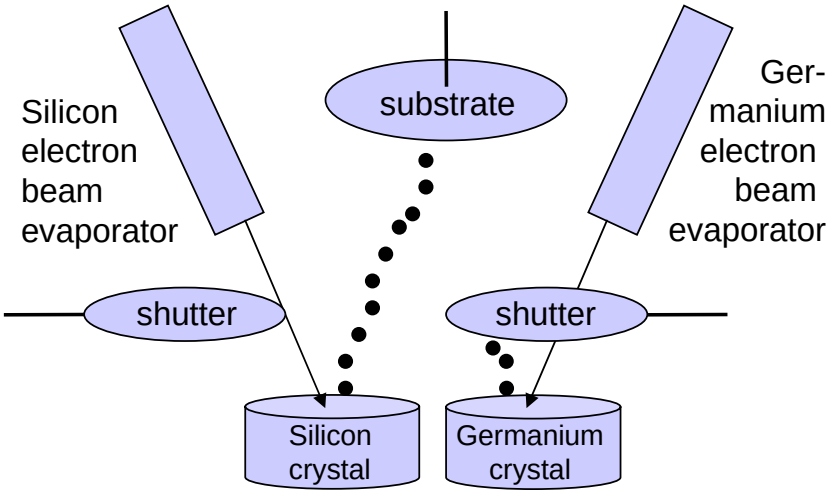

Figure 4.1: Schematic drawing of the inside of the MBE growth chamber. The electron gun evaporators are focussed on the target with the source material. The evaporated material produces the molecular beam which is directed towards the substrate. The growth is controlled by opening or closing the shutters. The Si and Ge fluxes are adjusted by changing the focus of the electron beam.

Blazers UMS 500. It is equipped with two e-gun evaporators for Si and Ge (see Figure 4.1) and an effusion cell for boron as dopant. The substrate can be heated up to 1000°C and the substrate holder is rotatable. The base pressure is $< 10^{-9}$mbar. During growth, the pressure is dependent on the growth parameters but usually $\sim 10^{-8}$mbar. The Si and Ge fluxes are controlled using a mass spectrometer. Its signal enters a feedback loop which adjusts the focus of the electron beam and therefore allows a fast change of the atomic fluxes.

The investigated structures were grown on SiGe pseudosubstrates with Ge contents of 20%, 25% or 50%. The pseudosubstrates were grown by Low Pressure CVD (LPCVD): On a Si wafer, epitaxial films with increasing Ge content were deposited until the final Ge concentration is reached (the actual relaxed buffer). A post-growth chemical mechanical polishing step to flatten the surface finishes the pseudosubstrate preparation. The surface roughness measured by AFM is about 2nm.

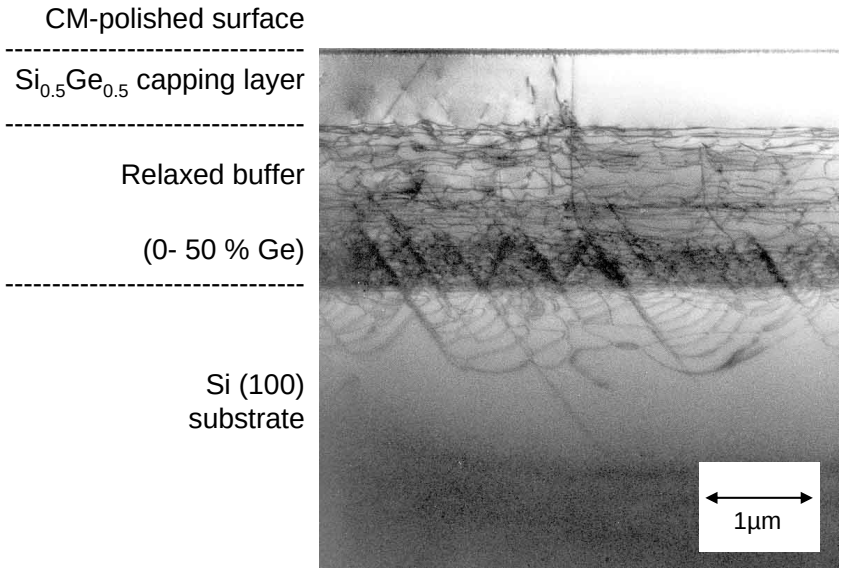

Figure 4.2: TEM picture of a $Si_{0.5}Ge_{0.5}$ psuedosubstrate grown by STMicroelectronics using LPCVD.

In Figure 4.2, the TEM picture of a 50% SiGe pseudosubstrate is shown. One finds many defects in the grown part but most of them are confined in the relaxed buffer with increasing germanium content. The confinement is achieved by the final, about 1μm thick $Si_{0.5}Ge_{0.5}$ cap layer which avoids that the defects have influence on the heterostructure. However, some of the defects reach the surface (so-called threading dislocations) and can short circuit the vertical transport through the heterostructure. In a usual buffer, the density of threading dislocations is in the range of $1 - 10 \cdot 10^7 \text{defects/cm}^2$ and needs to be taken into account as it is not negligible with respect to the device performance.
Before the transfer into the MBE growth chamber, the SiGe pseudosubstrates are cleaned by a wet-chemical etching step. In the growth chamber, the substrates are baked at 800°C. The growth itself is carried out at low temperatures between $300 - 350$°C and the Si and Ge fluxes are usually kept between $0.25 - 0.5$Å/s, respectively.

4.2 Characterization

For the structural characterization, usually two methods were employed: X-ray diffraction and Transmission Electron Microscopy. The first one gives a fast feedback on the periodicity, the composition and the layer thicknesses of the grown structure. The second method allows to draw a more qualitative conclusion about interfaces roughness, strain compensation in the structure as well as threading dislocations and point defects.
The method of X-Ray diffraction is a way of an exact and quantitative sample characterization. As the beam of the X-Ray has a size of several millimeters, the average over a lateral area of this size is measured. The depth of investigation can be several micrometers deep. The obtained diffraction pattern is very sensitive to the thickness of the layers and their composition. The fitting of these diffraction pattern is therefore possible with

monolayer accuracy and allows to determine the thickness of each layer in one period. A detailed description of this method can be found in [92]. In general, three results can be obtained from X-Ray measurements in different configurations. First, from the angle resolved measurement, the diffractogram can be obtained. The measured peaks and their positions relative to each other allow to draw conclusions about composition and thickness of each layer by fitting the diffractogram. A sample of such an X-Ray rocking curve is shown in Figure 4.3a together with the fitted curve and its parameters. The investigated sample is a 60 period waveguide structure (described in Chapter 8.2.3) with one period consisting of 21.5Å Si, 7Å Ge, 20Å $Si_{0.5}Ge_{0.5}$, 21.5Å starting with the lowest layer. The structural parameters found from the X-Ray diffraction are given in the inset in the left upper corner. It shows, that even small deviations of $\sim$ 1Å can be resolved by this tech-

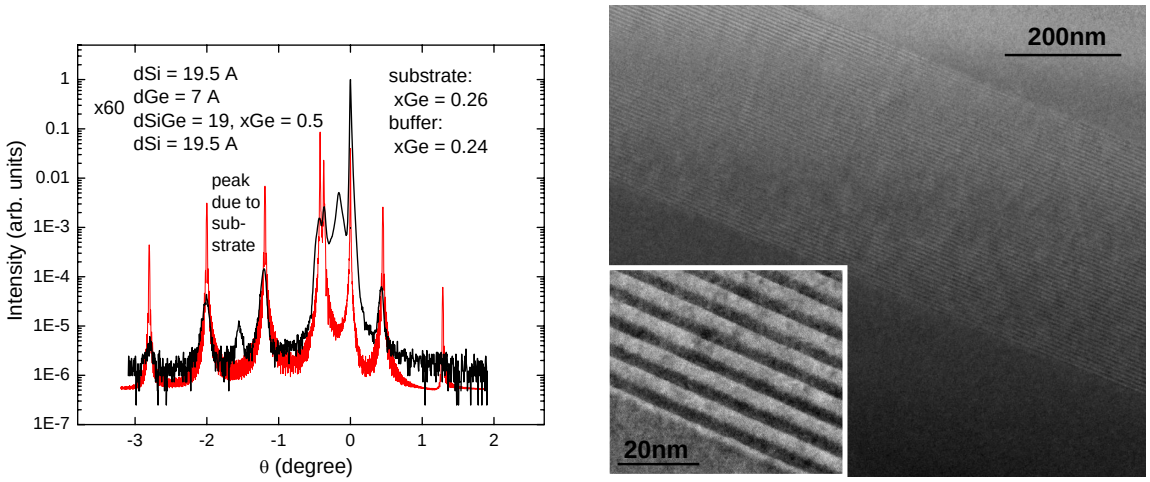

Figure 4.3: XRay diffractogram (a) and TEM picture(b) for a 60 period structure including pure Ge layers.

nique. The second tool of characterization obtained from the Xray measurement is the reciprocal space map. For this, several angle resolved measurements are taken while the angle off set between incident and scattered beam is changed for each measurement. This kind of measurement yields information about the degree of relaxation in the structure by mapping out the reciprocal space. Finally, information about the interface roughness in the structure can be obtained by X-Ray reflectometry in which both, the angle between incident and scattered light and the detector angle are varied while the reflected intensity is monitored.

The Transmission Electron Microscopy (TEM) yield a qualitative overview over the whole structure as well as good insight into atomic ordering process. It is an important analysis tool as the data obtained from XRay measurement are values averaged over a size of several millimeters. By using TEM, the high range of magnification (100 times to 10^6 times) allows a better insight in the crystal quality and the amount of strain. Point defects which are caused during the growth are increased by the strong e-beam and become visible. Also dislocations originating from the relaxed buffer can be identified which is important for

the electric properties of the grown structures.
The samples were characterized by Elisabeth Müller at the ETH-Zürich using a Philipps CM30 microscope with 300keV (for a detailed description see [93]). A TEM picture of a 60 period waveguide structure with 7Å pure Germanium layers is shown in Figure 4.3b. The contrast between bright and dark areas is obtained by the distortion of the crystal due to strain and by the different scattering factors of the different materials. By this, the separate layers and their thickness can be identified and it allows to draw conclusion about interface roughness. In the shown structure, one finds flat interfaces without strain induced waviness whereby the dark areas correspond to germanium rich regions and the bright areas correspond to silicon rich layers. For such kind of structure, the growth is well controllable including desired layer thickness and strain compensation.

Chapter 5

Measurement Setups

In this chapter, the experimental setups used in the frame of this work are described. For the characterization of the optical properties of the samples, absorption spectroscopy was employed. Using this method, the position of the energy levels in the active region can be mapped out. The comparison to the calculated absorption spectrum regarding transition energies and linewidths allows to draw conclusions about growth and quality of the samples.
The optical pumping setup described in the second section of this chapter was built up within this work. With this setup, the basis for optical pumping has been developed and the experimental conditions for SiGe lasing has been investigated. Tests of this setup with III-V samples proved its functionality. The lasing has been achieved in practically all investigated samples (see Chapter 7).

5.1 Absorption Setup

Absorption measurements are a common mean to investigate the energy levels within a grown structure. Throughout this work, two methods were employed:
(a) *Electrically modulated absorption:* The carrier population within the active region is modulated by an electric field. For this purpose, the upper barrier was doped between $1 \cdot 10^{18}\text{cm}^{-3}$ and $2 \cdot 10^{18}\text{cm}^{-3}$. As ohmic contacts, Al pads were evaporated and annealed for 2 minutes at 400°C under forming gas. In between two ohmic contacts, a $900 \times 900 \mu\text{m}^2$ Ti/Al (50nm/150nm) Schottky gate is evaporated. The gate is used to modulated the carriers in the quantum wells and consequently, the intersubband absorption. The modulated signal is detected using lock-in technique and can therefore be separated from the unmodulated background. The square wave voltage usually modulated at 1kHZ was applied between the four line-up gates and the ohmic contacts. The bias was alternatively change from -2V to $+(1)$V. Using the relation

$$N_S = \frac{\epsilon_0 \epsilon_r}{d} \cdot \frac{V}{e}$$

a total carrier density of $\sim 1 \cdot 10^{12}\text{cm}^2$ modulated in the whole active region is determined. Here, V is the applied voltage and d the active region thickness.

(b) *transmission measurements:* Absorption measurements using the direct transmission were employed for the waveguide structures. Due to the thick cladding layer in a waveguide structure, the application of a field is unsuitable. But the active region of those samples is composed of numerous periods (usually 60 periods, $\sim 0.5\mu$m) which allows to detect the intersubband transitions by analyzing the light transmitted through the active region. To separate the contributions of the active region from the one of the substrate, a reference measurement of the substrate was taken. For this, samples were investigated where in parts of the samples the active region was etched away or MBE shadowed regions were present.
The backside of the 4mm long samples was polished down to a thickness of 250μm, typically. The sample facets were wedged in a 45° geometry. The light coupled into one of the 45° facets was obtained from a glowbar source. The number of passes given by length and thickness of the samples was typically 13. A sketch of the experimental setup is given Figure 5.1 and the detailed path of light within the sample is shown in the schematic drawing in the left lower corner. The modulated absorption was measured

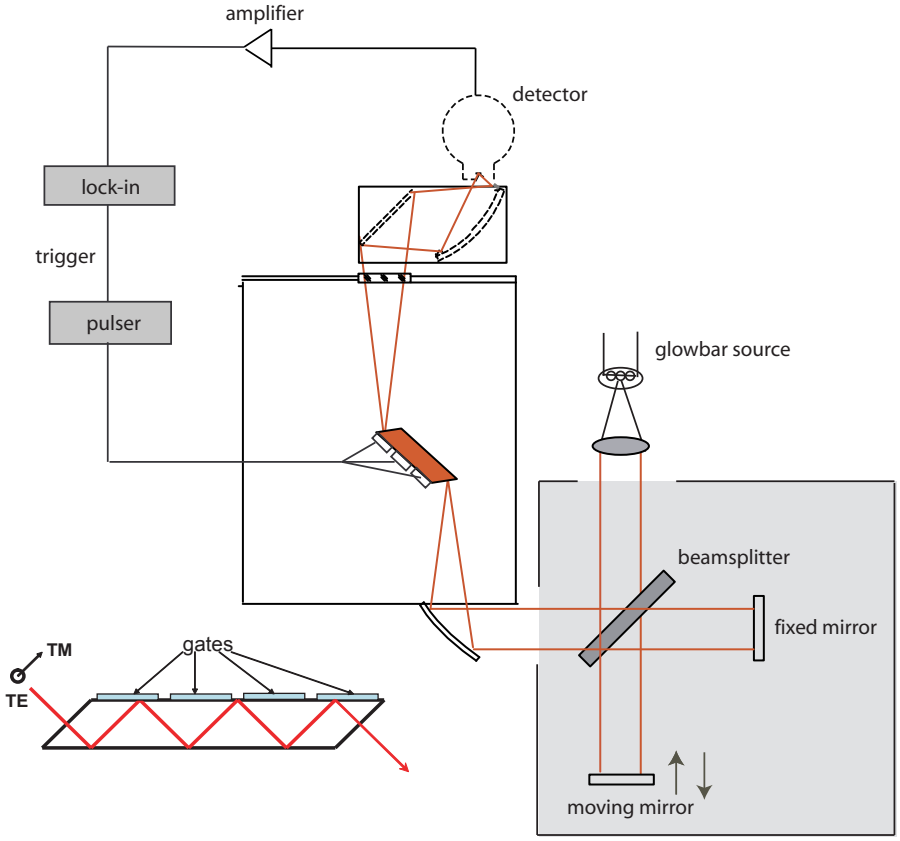

Figure 5.1: Schematic drawing of the experimental setup used for the absorption measurements. The red lines indicate the path of the light. In the lower left corner a sketch of the incoupling geometry is shown and the two polarizations TM and TE are indicated.

with a Bruker IFS 55 Fourier transform infrared spectrometer in step scan mode. The transmission was measured in fast scan mode. The samples were mounted into a He-cooled cryostat and measured between 20K and 300K. The optical signal was detected

by a liquid nitrogen cooled MCT (HgCdTe) detector. To obtain the polarized spectra in either TE or TM mode, a polarizer was placed before the cryostat. This setup was used for the characterization of the III-V samples (see Chapter 7) and for the SiGe samples described in Chapter 8.

5.2 Optical Pumping Setup

The experimental setup for the optical pumping is shown in Figure 5.2. As pumping source, two different Nd:YAG lasers were (alternately) used: The first one is a more powerful flash-lamp pumped active mode locked Nd:YAG laser with a pump pulse energy of typically 300μJ to 500μJ at a repetition rate of 3Hz and a pulse width of 0.8ns. The second one is a Q-switched PowerChip Nd:YAG (teem-photonics) laser with a typical pulse energy of 70μJ at 1kHz and a pulse width of 0.4ns. These laser pulses have a better

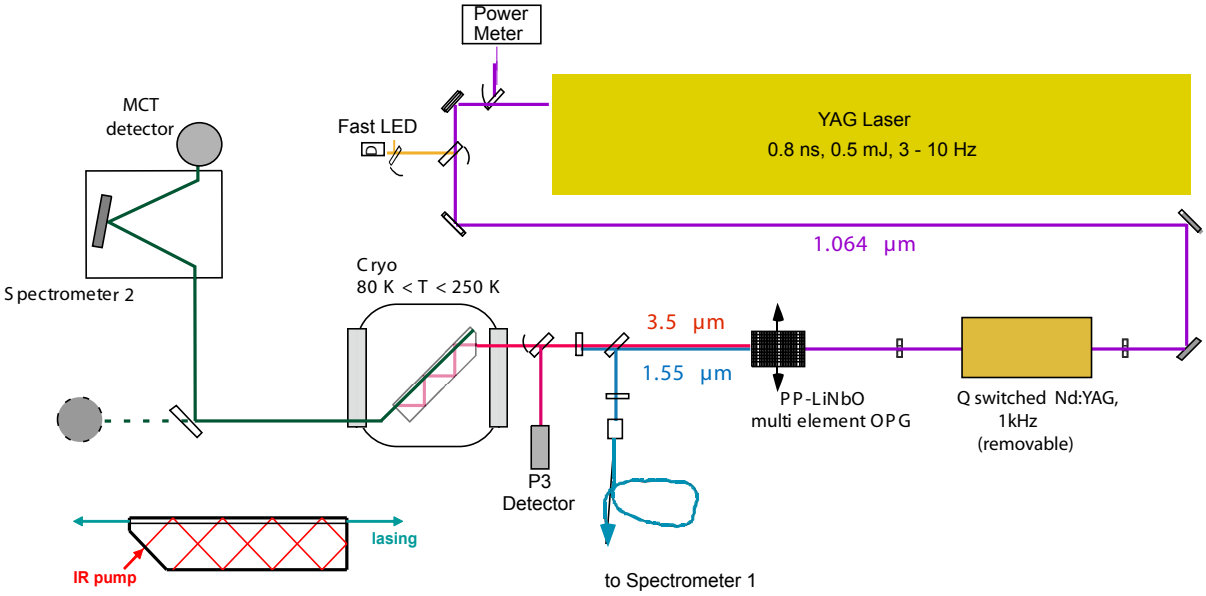

Figure 5.2: Sketch of the experimental setup for the optical pumping experiments. The infrared light is indicated as red line, the idler blue and the outcoupled laser light as green line. The inset in the lower left corner shows the sample geometry.

stability and the higher repetition rate decreases the measuring time considerably but the total output power is a factor $2-4$ lower. Both lasers operate at a wavelength of 1064nm. The laser pulses are coupled into a 5mm long, periodically pooled Li-Niobate crystal which converts the incident light into infrared pulses with pump pulse energies of 20μJ or 3.5μJ for the 3Hz and 1kHz laser, respectively. Filters are used to block the wavelengths below 3μm coming from the laser source and the idler signal which however introduced loss of about 50%. Behind the filters, lenses and cryostat window, an incoupling pump pulse power at the samples facet of 9.5μJ and 1.7μJ for the 3Hz and 1kHz laser is achieved, respectively. The obtained wavelength between 3μm and 4μm can be fine-tuned by using different elements of the crystal and by setting the temperature of the crystal between

50°C and 200°C. For a precise determination of the obtained signal wavelength, the idler photon was used. In the nonlinear crystal, the incident photon is split into two photons, the signal and the idler photon. Their wavelengths (λ) are connected by:

$$\frac{1}{\lambda_{inc}} = \frac{1}{\lambda_{Signal}} + \frac{1}{\lambda_{Idler}}$$

The wavelength of the idler photon ($\sim 1.5\mu$m) was determined using a mini spectrometer as shown in Fig. 5.2. The infrared light was couple into the $\sim 250\mu$m thick samples via the polished 45° facet. The inset in Fig. 5.2 shows the coupling geometry and the path of light. The broad area lasing cavity is formed by either cleaved 90° facets (III-V material) or by etched mirrors (SiGe) using a Bosch etching step. The samples were mounted into a He-cooled flow cryostat and held between 20K and 150K. For integral measurements like threshold and total power measurements, the outcoupled lasing light was directly detected by an MCT detector. For spectral analysis, the MCT detector was placed behind a grating spectrometer with a resolution of 0.2meV for a slit width of 400μm. The responsiveness of the MCT detector was calibrated using a room temperature MCT detector. To minimize the atmospheric absorption due to water and CO_2, the spectrometer was nitrogen purged and the outcoupled lasing light was guided from the cryostat to the detector through a nitrogen flow box.
For the optical pumping experiment of the SiGe structures, TM and TE polarized excitation is required. The incident light from the YAG lasers was TM polarized in the plane of the optical table. To obtain TE polarization, the light could either be converted using a $\lambda/4$ plate or by rotating the sample about 90°. For our experiment, the second possibility was chosen as with the appropriate holder, samples for TE and TM excitation could be mounted together. That way, III-V samples with TM excitation could be used as alignment reference for the SiGe structures.
The setup was built up and tested using III-V structures. The results on these samples are summarized in Chapter 7. For those measurements, the 1kHz laser was used in order to obtain smoother spectra and more precise data, especially for threshold measurements and wavelength determination. For the SiGe structures both lasers were used as the 1kHz laser allows a better prealignment but the 3Hz offers a 3 times higher power after downconversion.

Chapter 6

Electrically pumped SiGe quantum cascade structures

In this chapter, the work carried out in the collaboration between the PSI and the University of Neuchâtel and work relevant for this thesis is summarized. First, the SiGe benchmark structure and the obtained electroluminescence is introduced, characteristic values and the main problems are explained. These problems are discussed in the course of this chapter with main emphasize on the topic of linewidth broadening and waveguide design. Transport properties are investigated using Resonant Tunnelling Diodes (RTDs). The problems and hindrances in realizing an electrically pumped SiGe QCL are briefly summarized. From that, we conclude that the way to overcome these difficulties for the electrical pumping is too long to be feasible. This leads to another, more straight forward approach towards a SiGe based QCL , the optical pumping. It offers an alternative way to study the intersubband lasing in SiGe because it applies to structures without the optical loss inducing contact layers.

6.1 Active Layer Design based on strain compensated bound-to-continuum transitions

Electroluminescence from SiGe heterostructures was first demonstrated in [36] approving the idea of realizing the quantum cascade concept in Si-based materials. An emission wavelength of about 9μm with a linewidth of $\sim$ 22meV and an estimated upper state lifetime of 0.5ps are the characteristic values obtained for those structures. The samples were grown pseudomorphically on Si substrates which implies a large strain accumulation within the structure limiting the total layer thickness. As discussed in chapter 2, the gain in quantum cascade lasers is proportional to the number of periods and it is desirable to obtain large overlap factors of the gain medium with the optical field in the waveguide. Though, this is not possible in pseudomorphic structures as the layers will relax when a critical thickness is exceeded. The growth on SiGe pseudosubstrates in a strain compensated manner is a possible solution. The pseudosubstrates consist of a graded SiGe buffer grown on Si substrates by chemical vapor deposition with a Ge content ramped

from 0% to 50%. By employing this concept, the compressive strain of the SiGe wells grown with a higher Ge content than the one of the pseudosubstrates can be compensated by the tensile strain of Si layers. This opens broader possibilities in the design of laser schemes and for the growth of thick waveguide structures. Emission from such strain compensated $Si_{0.2}Ge_{0.8}$ quantum cascade structures was first reported in [37] employing HH states for the optical transition. The design was based on a 'bound-to-continuum' scheme (Fig. 6.1) which was previously developed in III-V materials [94]. This kind of

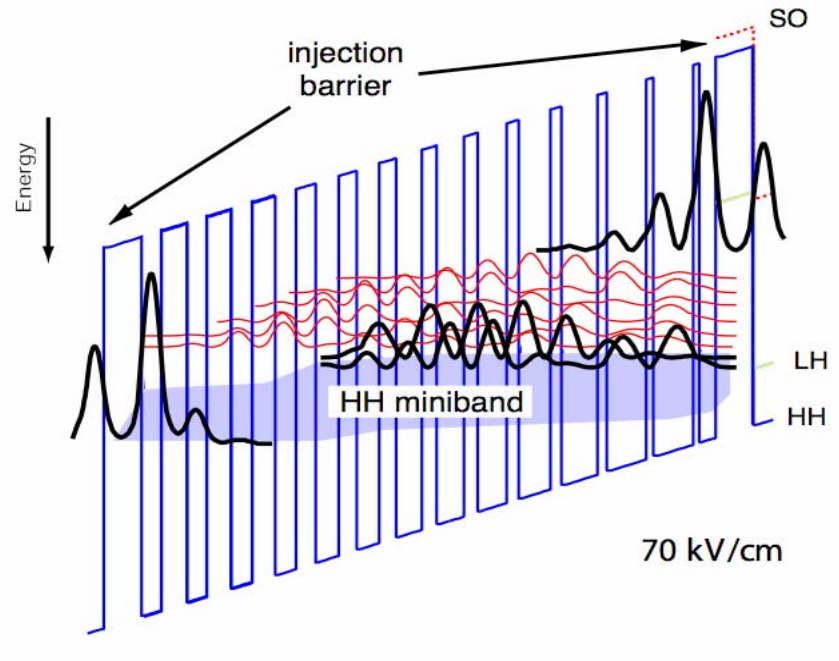

Figure 6.1: Schematic valence band diagram and square moduli of the wavefunctions for the bound-to-continuum SiGe quantum cascade with applied field of 70kv/cm as published in [37]. The black solid lines indicate the HH levels, the blue thin lines the interspersed LH levels. One period consists of the following Si barriers and $Si_{0.2}Ge_{0.8}$ wells (bold) in Å: 25/**11**/4/**26**/5/**26**/6/**24**/7/ **21**/8/**19**/9/**18**/10/**17**/11/**15** /12/**15**/13/**14**/15/**14**/16/**13**/17/**13**. The underlined values correspond to layers doped with $p \sim 5 * 10^{17}\mathrm{cm}^{-3}$.

design provides the advantage of an effective injection to the upper laser state (which is referred to as the bound state) and a fast extraction of carriers from the lower laser state via the miniband in order to build up population inversion. The fast depopulation of the lower level is especially important for SiGe structures as only short upper state lifetimes of 0.1ps [37] to 0.25ps [95], [96] for the excited states are expected due to selection rules and strong bandmixing [35]. However, this extraction region is difficult to design for SiGe based structures as Si and Ge are non-polar materials: In polar material like in any III-V material, due to the dominating Fröhlich interaction, an effective electron-phonon scattering can be achieved by bringing the electronic levels in resonance with the optical phonon energies. In contrary, for non-polar materials the deformation potential interaction is dominating the nonradiative scattering which does not show such resonant behavior. In [95] it has been shown that the optical phonon interaction of holes is increas-

ing with the subband spacing if the latter one is bigger than the optical phonon energy. This suggests broader minibands in the range of 100meV for SiGe QC structures in order to provide efficient extraction, which is considerably broader than in a comparable III-V structure ($\sim$ 60meV). Beyond this, the selection rules, which state that the emission of phonons between subbands with identical symmetry are forbidden, require to take into account LH and HH level while designing an effective depopulation. A detailed discussion of lifetimes in SiGe and means to increase upper state lifetimes, though, is beyond the scope of this overview and the interested reader is referred to [35]. In Figure 6.2, V-I

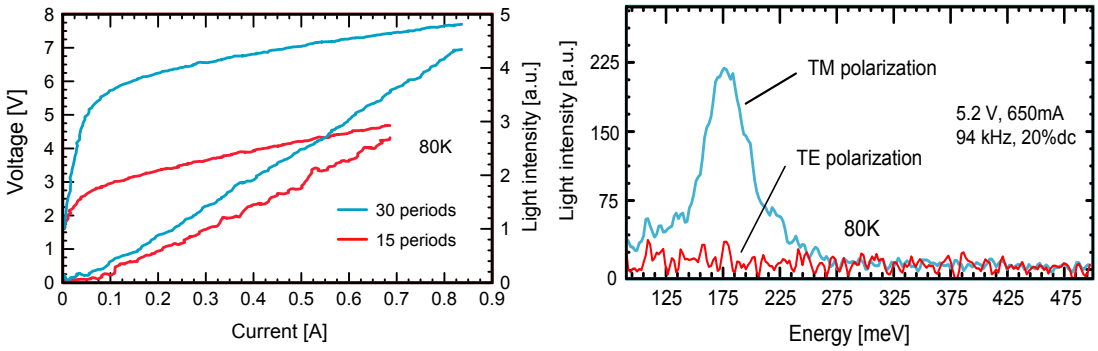

Figure 6.2: (a) V-I and L-I for a 15 and 30 periods sample. The threshold voltage for both samples are found to be 2.4V (5.7V), respectively. These values are considerably lower than the ones calculated for a proper injection (4.25V and (8.5V). (b) Emission spectra of the b2c sample at $T = 80$K in TE and TM polarization at 5.2V, 650mA, 94kHz and a duty cycle of 20%. Taken from [37].

and L-I curves and a typical spectra of a structure based on bound-to-continuum (b2c) transitions at a temperature of 80K is shown. The emission peak obtained at 185meV shows a FWHM of $\sim$ 46meV. This value agrees well with the typical widths obtained by absorption spectroscopy for intersubband transitions in modulation doped $Si/Si_{0.2}Ge_{0.8}$ QWs as published in [97]. The polarized spectra prove the TM character of the emission as expected for HH transitions from the selection rules [71]. Injection current densities up to 1kA/cm^2 were be reported by using finger structures with an area of $5.4 * 10^{-4}$cm^2. In further research [98], the injection current density could be efficiently improved up to 6.5kA/cm^2 by providing the current via smaller finger structures and therefore, ensuring a more uniform injection. Above $J = 7$kA/cm^2, the emission spectra are clearly dominated by black body emission due to lattice or carrier heating.
The condition to achieve lasing is, that the gain has to overcome the losses. The gain in the active region is determined by linewidth, injection current density as well as upper state lifetime and occupation. The material losses in the active region result from free carrier like absorption of holes in the lower states. This loss can be modelled using a Drude-type absorption [99]. It shows, that to improve the gain in the active region (besides a long upper state lifetime as mentioned before), narrow linewidths and an efficient injection process is required. To clarify the possible efficiency of the tunnelling process, resonant tunnelling diodes have been investigated (Chapter 6.4). Besides the active region design, a low loss optical waveguide is necessary. In SiGe, thick contact layers are

needed determined by the high effective mass of the holes in SiGe ($m^* = 0.2m_e$) as well as the strong interface roughness and alloy scattering resulting in a poor mobility. These contact layers lead to high optical losses caused by free carrier absorption. The main results of the research within the last years regarding the understanding of the origins of the linewidth broadening on the one hand and the waveguide loss on the other hand will be summarized in Section 6.2 and 6.3, respectively.

6.2 Intersubband Broadening

The typical linewidth of $\sim$ 45meV for intersubband transition in SiGe quantum cascade structures is about factor 4 larger than in similar III-V devices. The two main reasons for linewidth broadening are found to be the non-parabolicity of the subbands and the interface roughness which is negligible in most III-V QC structures but has to be considered in SiGe devices due to the large lattice mismatch of 4% between Si and Ge and the need to grow at low temperature to avoid Ge islanding. In Fig. 6.3, the effects of the

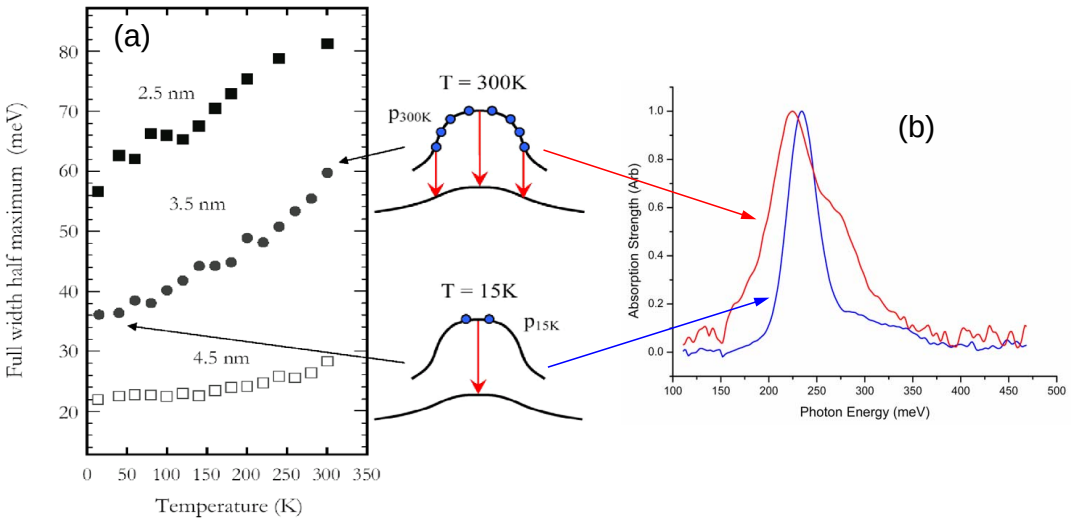

Figure 6.3: Influence of the temperature on the linewidth broadening due to non-parabolicity for different QW thicknesses. (a) The FWHM plotted against temperature for 2.5nm, 3.5nm and 4.5nm thick QWs. The linewidth is increasing with temperature. This is also illustrated by the absorption spectra shown in (b) and can be assigned to the occupation of subbands at higher k.

non-parabolicity are shown. At low temperature, carriers are located around zero inplane wavevector $k = 0$ and hence, no distribution of carriers within the k space takes place. As the energy bands have a different bending in k space (non-parabolicity), the transition energies are changed for higher k values. With increasing temperature, carriers are now distributed to higher k where the two subbands involved in the transition process are not parallel and therefore broaden the transition linewidth (Fig. 6.3b). This temperature effect is increasing for thinner quantum wells below 35Å (Fig. 6.3a). Furthermore, from

the comparison of the linewidth of quantum wells with different thicknesses, it is obvious that thinner wells show larger broadening. This is due to the position of the HH2 states relative to the $Si_{0.5}Ge_{0.5}$ band edge. In thicker QWs (e.g. 35Å), the HH2 state is located below the $Si_{0.5}Ge_{0.5}$ band edge while it is above for the 25Å QW. This leads to a much stronger coupling of mixing between HH and LH/SO states causing a stronger non-parabolicity and therefore larger broadening with increasing lattice temperature.

The second effect which was found to have a crucial impact on the linewidth broad-

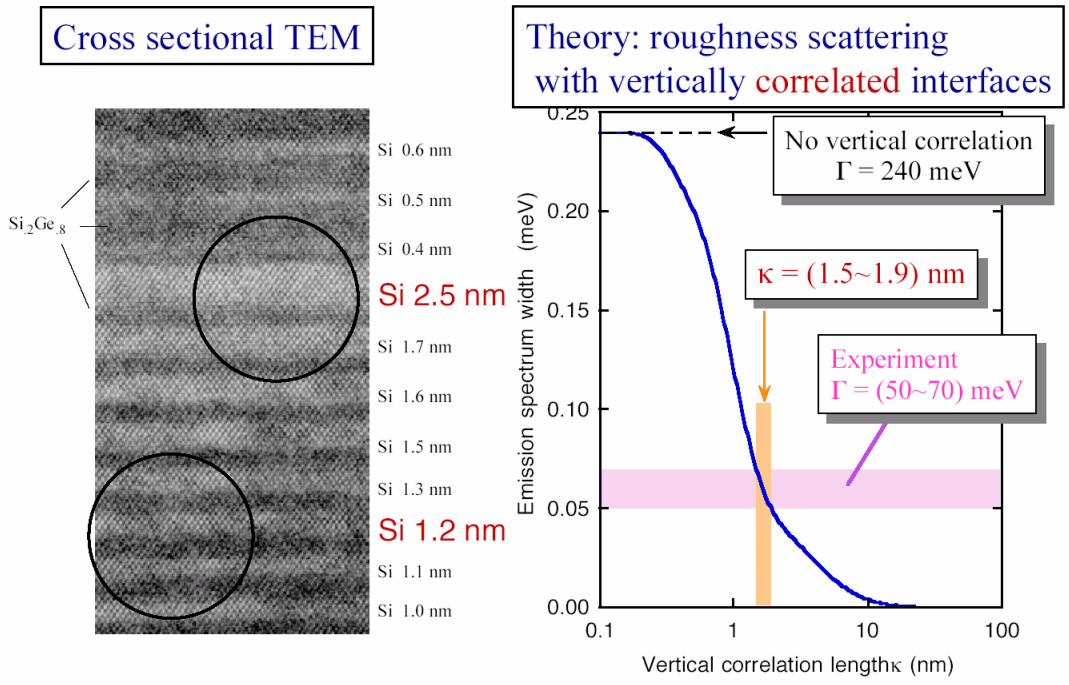

Figure 6.4: (a) TEM cross section of the investigated SL structure. (b) Influence of the vertical correlation between the QWs on the broadening of the intersubband transitions. The bars for the linewidth and the vertical correlation length mark the experimental results. [102]

ening is the interface roughness which was theoretically described in [100] and [101] and applied for SiGe quantum cascade structures in [102]. According to this, the broadening of a transition between two subbands is determined by the extension of the wavefunctions, the average roughness of the interfaces and the correlation length. These values can be obtained from statistical analysis of the TEM cross section of the corresponding samples (see e.g. Fig 6.4a). For our samples, average values of 0.32nm for the roughness and 2.3nm for the correlation length are obtained. Including these parameters into the linewidth calculation, a $4-7$ times larger linewidth is found than observed in measurements. However, by taking into account the vertical correlation, the theory coincides with the experiments. The vertical correlation describes the influence of the interface roughness of two adjacent quantum wells (i and j) by a vertical correlation factor c_{ij} which is zero for uncorrelated interfaces. Figure 6.4b shows the influence of the vertical correlation length κ ($c_{ij} = exp[-(z_i - z_j)^2/\kappa_2]$) on the linewidth broadening. The bigger the vertical correlation length, the smaller is the broadening of the transition linewidth as the

interfaces of neighboring quantum wells are compensating each other. As from the experiment linewidths in the range of 45meV to 70meV are obtained, a corresponding vertical correlation length of $(1.5 - 1.9)$nm was determined for the investigated SiGe structures. The impact of the vertical correlation can be clearly deduced from Figure 6.4b, as the linewidth for correlated interfaces is improved by a factor 4. Hence, it can be concluded that the interface roughness and therefore the vertical correlation have a tremendous impact on the linewidth broadening. Optimization of the Si/Ge crystal growth regarding to the interface quality is thus crucial for the realization of SiGe QCLs.

6.3 Optical Loss in Waveguide Structures

The effective mass of holes in SiGe is in the range of $0.2m_e$ with m_e as free electron mass. This leads to relatively low mobilities of less than $100\text{cm}^2/\text{Vs}$ in moderately doped SiGe layers with $\sim 50\%$ Germanium concentration which is about a factor 50 lower than in the common III-V systems. Hence, in order to provide sufficient electrical conduction, high doping levels are required. Furthermore, the standard waveguide design used e.g. in MIR InP QCs consisting of a lightly doped cladding layer embedded into highly doped plasma reflectors (the doping of the latter one is chosen that way that the plasma frequency matches the desired emission wavelength causing a considerable drop of the refractive index) is not suitable. The low plasma reflection, the required high doping and the resulting high optical loss require a more sophisticated waveguide (see section 6.3.1) and a careful design of the contact regions (see section 6.3.2).

6.3.1 Waveguide Design

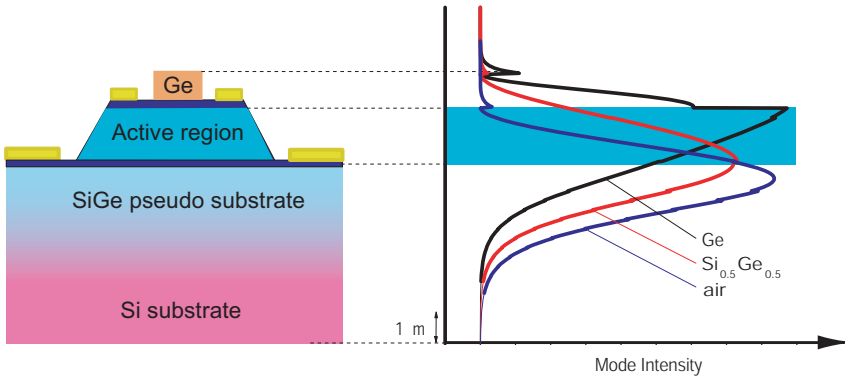

Figure 6.5: Schematic drawing of the proposed WG structure (a). The Ge stripe is centered and the contacts are shifted from the mode maximum towards the sides of the etched mesa. (b) The calculated mode profiles for different cladding layers (air, SiGe and Ge) are shown. For demonstration, the area of the active region is plotted within this graph. [99],[103]

The challenge in developing a suitable waveguide for SiGe quantum cascade structures is to reduce the free carrier absorption at the electrical contacts and to achieve a high

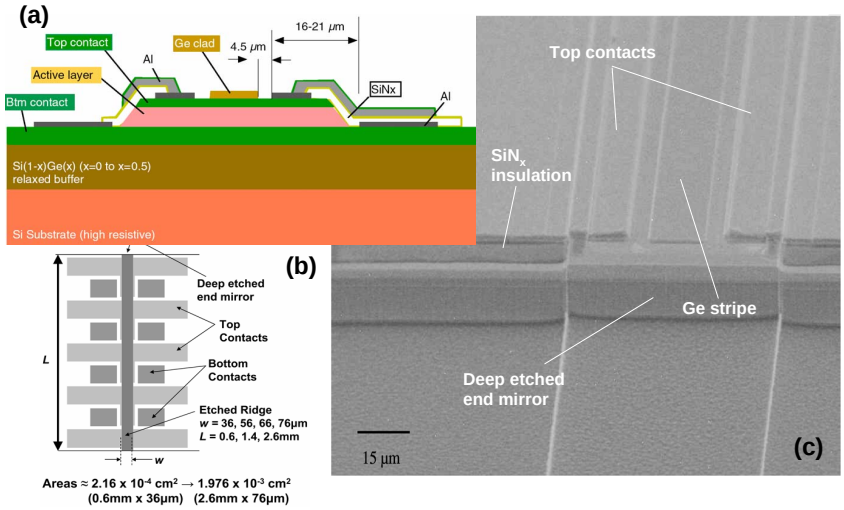

Figure 6.6: Schematic drawing of the realized waveguide structure (a), the top view of the structure with wide contact areas in order to provide uniform injection (b). The SEM picture (c) shows the completed waveguide structure. As published in [98]

overlap factor for the waveguide mode with the active region. The mode intensity and the overlap with the active region is determined by the boundary conditions at the interface of the cladding layer with the adjacent medium. To meet above challenges a waveguide design as shown in Figure 6.5 was suggested [99],[103]: On top of the common SiGe cladding layer, an additional Ge layer was added in order to force the mode towards the surface, as shown in the right plot. Compared to air and SiGe claddings, the mode overlap with Ge is the highest. The values for the mode overlap obtained from the calculation is 0.24 without cladding (air), 0.39 with a SiGe cladding of 1μm and 0.45 for a 1μm Ge layer. From this calculation it is obvious, that the best overlap and strongest intensity can be achieved by adding a Germanium layer. To separate this peak of the mode laterally from the contact area, the Germanium was evaporated as a stripe in the middle of the waveguide well separated from contacts to reduce the optical loss from the contact regions. However, in this configuration, the contacts have to provide a high lateral conductivity as well as a high vertical conductivity.
The waveguide structure described above was realized in SiGe for the benchmark structure discussed previously and compared to the performance of small area ($1.8 * 10^{-4}$cm^2) finger structures [98]. The processing was optimized especially regarding to process temperatures in order to minimize the material stress and to avoid defect formation causing high leakage currents. The schematic cross of such a ridge waveguide, the top view and the SEM picture of a completed waveguide structure are shown in Figure 6.6.

Processing of the Germanium stripe

The suitability of the above design was tested using III-V micro-cylinder cavities. Details on the processing and the working principle of these micro-disks are given in [35] and [103]. The round mesas with a diameter of 160μm were wet etched in a HBr solution. On

top of that, a 100um Ge/Au/Ag/Au contact was evaporated and annealed at 355°C. The final step was the evaporation of the 750nm thick Ge layer on top of the mesa. A hole in the middle of the Ge layer was left for bonding the devices.
Testing and comparison to common InP cladding samples showed a much larger threshold current density for these structures and therefore, operation at low temperature only [103]. In numbers, a conventional waveguide has a threshold of about 1.2kA/cm^2 at 80K while for the Ge cladding waveguide structure a threshold of $\sim$ 4.3kA/cm^2 was found. A reason for this bad performance was found in the final process step of Ge evaporation. As the Germanium is evaporated after the contact processing, the surface of the microdisks shows contamination and/or oxide layers making a proper Ge deposition difficult. Therefore, an additional Argon cleaning step before the Ge evaporation was done in order to improve the interface quality between the InGaAs and the Ge cladding. The results for different times of this cleaning step are shown in 6.7. The threshold current density could

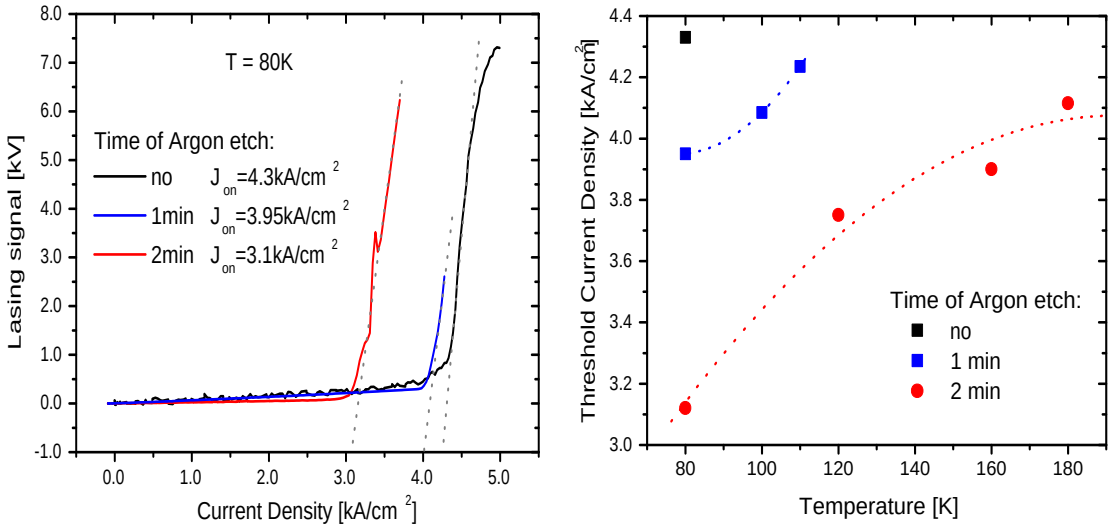

(a) (b)

Figure 6.7: (a) L-I characteristic of three InP based microdisc lasers at T = 80K. On all of them Ge was deposited, one without any Ar etching before the Ge evaporation, the other two with 1min and 2min Ar etch, respectively. (b) Lasing onset current density in dependance of the temperature for the samples with different treatment before Ge evaporation.

be reduced down to 3.1kA/cm^2 at 80K by using a 2min Ar etch before the Germanium evaporation. Furthermore, lasing at temperatures up to 180K was achieved. These results indicated that the performance of the Ge waveguide devices is highly influenced by the InGaAs/Ge interface. This assumption is supported by the fact that the investigated devices showed aging behavior after several weeks storage under ambient air. It is assumed that an interfacial oxide between the InGaAs and the Ge layer is formed which has a low refractive index resulting in very high optical losses for the TM lasing mode [103]. These additional losses could be avoided by using an additional passivation step with Si_3N_4 after the Argon cleaning step.

6.3.2 Contact Design

The first contacts investigated for the SiGe waveguides were common 3D contacts: The active region was sandwiched between $\sim 1\mu$m thick $Si_{0.5}Ge_{0.5}$ contacts layers, doped at $p \sim 1 * 10^{19}\text{cm}^{-3}$ in order to provide sufficient transconductance. However, by using this scheme, the mode overlap with the contact layers is about 5% resulting in a free carrier loss of estimated $\alpha = 60\text{cm}^{-1}$. This estimate is based on the Drude free carrier absorption using for the scattering time the value found from the Hall measurement yielding a mobility of $6 * 10^{-3}\text{m}^2/\text{Vs}$. As possible solution to these problems, modulation doped

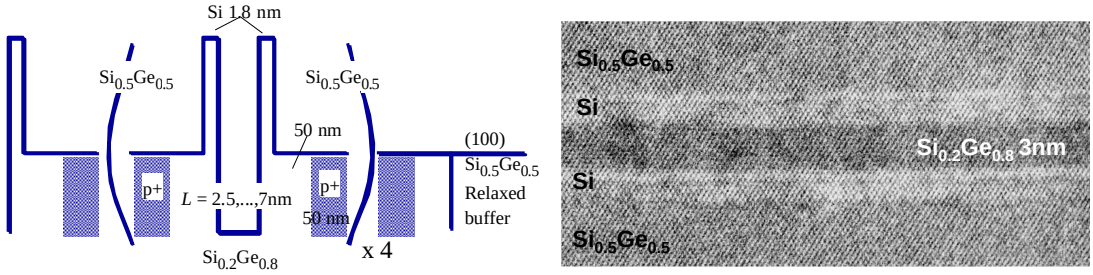

Figure 6.8: (a) Schematic drawing of the MQW structures. One period (region in brackets) was repeated 4 times. (b) Section of a TEM picture taken for the 3nm thick QW including barriers. [104]

MQW structures providing a high inplane mobility via a 2-dimensional hole gas (2DHG) were investigated. Waveguide calculations suggested that by employing these contacts, the free carrier losses could be reduced by a factor of 10 to $\alpha = 5\text{cm}^{-1}$ while maintaining the overlap factor of 5%. Therefore, these structures were investigated in detail as reported in [104] and briefly summarized in the following: The samples consist of four identical $Si_{0.2}Ge_{0.8}$ QWs and Si barriers separated by $Si_{0.5}Ge_{0.5}$ layers. The thickness of the QWs was varied between 2.5 and 7.5nm with a barrier thickness of 1.8nm. In Figure 6.8 the TEM cross section of the 3.0nm thick QW sample is shown. All interfaces were found to be abrupt and undulations or structural degradations were negligible. Absorption measurements performed on these structures are presented in [105] and will not be further discussed here. In order to determine the suitability of the MQW concept for the electrical injection, the Hall mobility and the hole concentrations were measured below 80K to ensure the freeze out of the parallel conduction. From this, a hole concentration of $1 * 10^{16}\text{m}^{-2}$ was found with a highest mobility of $0.44\text{m}^2/\text{Vs}$ for the 7nm thick QW which is about a factor 7 higher than previously reported for 10nm samples [106]. From the analysis of the slope of the mobility versus QW thickness plot it was found that for QW thicknesses $\leq$ 4.5nm the interface roughness is the limiting scattering process. Some details about interface roughness scattering was already given in the previous chapter including further reading. For QWs bigger than 4.5nm, the effects of interface roughness are rapidly decreasing and other scattering mechanisms become important. These are scattering by ionized impurities, interfaces charges and strain fluctuation. The effect of the ionized impurities resulting from threading dislocations and/or point defects on the mobility can be diminished by annealing for 15min at 600°C in forming gas. This

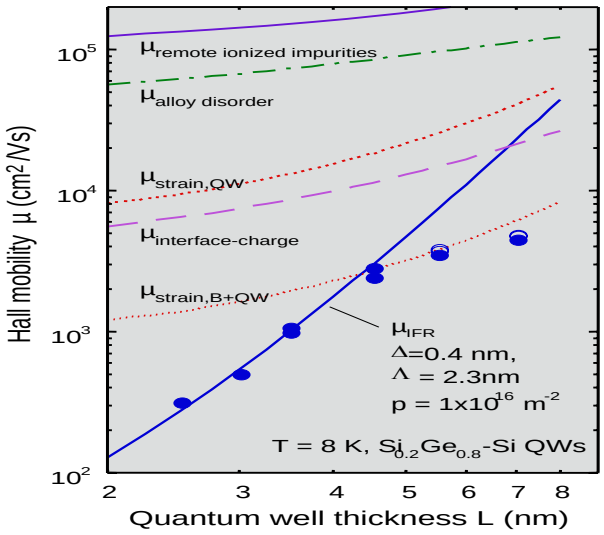

Figure 6.9: Hall mobility versus quantum well thickness at low temperature. The points indicate the experimental values, the solid line shows the calculated interface roughness limited mobility. The dashed lines represent the calculated mobilities limited by impurity scattering, alloy scattering, strain as well as interface charges (from top to down). [104]

increases the mobility slightly by about 10%. The second mechanism considered, the interface charges, contributes a mobility limit of $2\text{m}^2/\text{Vs}$ by assuming a charge density of $0.25 * 10^{16}\text{m}^{-2}$. The last scattering process taken into account, the strain fluctuations induced by interface roughness, are also assumed to have a tremendous impact on the mobility as strain is present in the QWs as well as in the barriers. However, a quantitative analysis is not yet performed. An overview of these different scattering mechanisms and their impact depending on the QW width is shown in Figure 6.9.
As mentioned before (see section 6.3.1), the obtained high inplane mobility ($\sim 0.45\text{m}^2/\text{Vs}$) is needed but not sufficient to obtain efficient current injection. In order to obtain current densities up to $10\text{kA}/\text{cm}^2$ and hence, carry high vertical currents through the MQW structures, also a high vertical conductivity is crucial. For these two requirements a compromise is necessary: A lower Ge content of the contact layers increases the vertical conductance due to a lower activation energy and therefore, a more effective tunnelling process through the barriers. However, the lateral conductance is decreased by the increased alloy scattering and decreased mobility. Therefore, the MQW contacts needed to be optimized regarding the Ge content, the barrier thickness as well as the number of periods. This was done by testing $\text{Si}_{1-x}\text{Ge}_x$ MQWs on 50% SiGe substrates with different quantum well thicknesses. The results obtained are summarized in Figure 6.10. As describe in [99], the lateral conductance necessary for the investigated waveguide structure, is determined by the maximum current density, the waveguide width and the total vertical voltage drop. From this analysis it was found, that for a $10\mu\text{m}$ wide waveguide a 10 period MQW contact structure using 12nm $\text{Si}_{0.4}\text{Ge}_{0.6}$ QWs provides a high enough lateral conductivity by satisfying the requirements to the vertical one at the same time. Moreover, calculations have shown that for this structure the free carrier like absorption

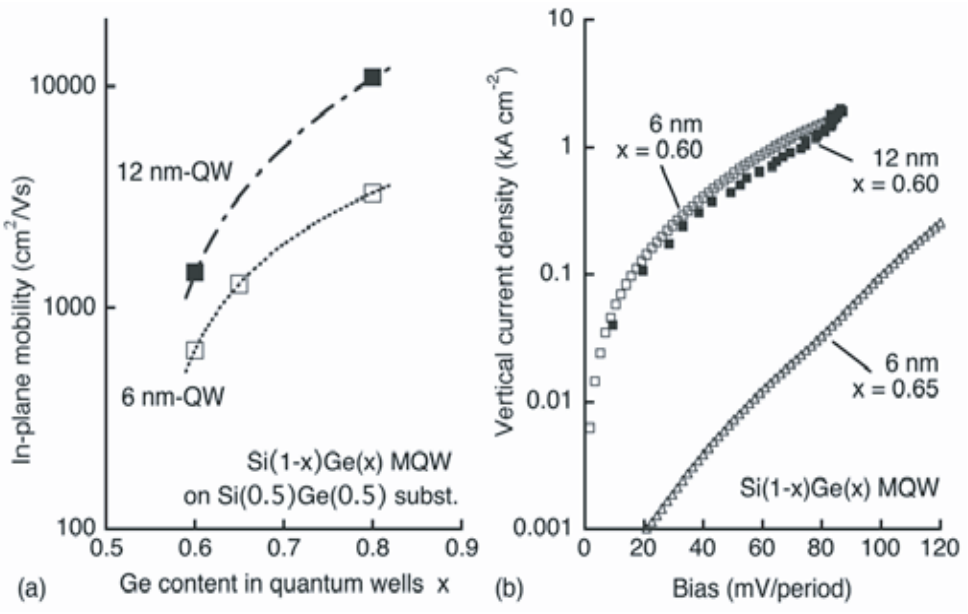

Figure 6.10: (a) Summary of the obtained inplane mobility for 7nm $Si_{0.2}Ge_{0.8}$ QWs, 12nm $Si_{0.4}Ge_{0.6}$ and 6nm QWs with different Ge content. The inplane mobility is clearly increasing with the Germanium content. (b) Vertical conductance for samples with 60% and 65% Germanium. For lower Germanium content a higher current density can be applied. Taken from [99]

may become much lower than for 3D contacts. This can reduce the total absorption and hence, the loss, of a factor $50 - 100$. However, for an experimental confirmation, further measurements are required.

6.4 SiGe Resonant Tunnelling Structures

In this section, the tunnelling process in double barrier SiGe structures is investigated using transport measurements and magneto tunnelling spectroscopy. The aim is to determine the energy levels in the QW and to assign the type of resonances to LH or HH. From this it will be concluded that the efficient injection into the HH states is possible and the conditions for LH tunnelling will be pointed out.

6.4.1 Basic principle

In the previous chapter it was discussed that in any QCL the tunnelling process plays an important role regarding the efficient injection into the upper state in order to achieve population inversion. For the characterization of this process, resonant tunnelling diodes (RTDs) have been employed. The first RTDs realized as a double barrier structure in the GaAs/AlGaAs were reported in 1974 [107]. Later on, similar structures were investigated for n- and p-type Si/SiGe [108], [109]. That kind of structure usually consists of a single QW coupled to the buffer layers by tunnelling barriers. Such simple devices

provide insight in a number of crucial issues regarding to the realization of QCLs: First of all, by applying a voltage, they allow to map out the electronic band structure of the holes within the quantum well. This principle is schematically depicted in Figure 6.11 (for a detailed review see [110] and the references therein): The band diagram for differ-

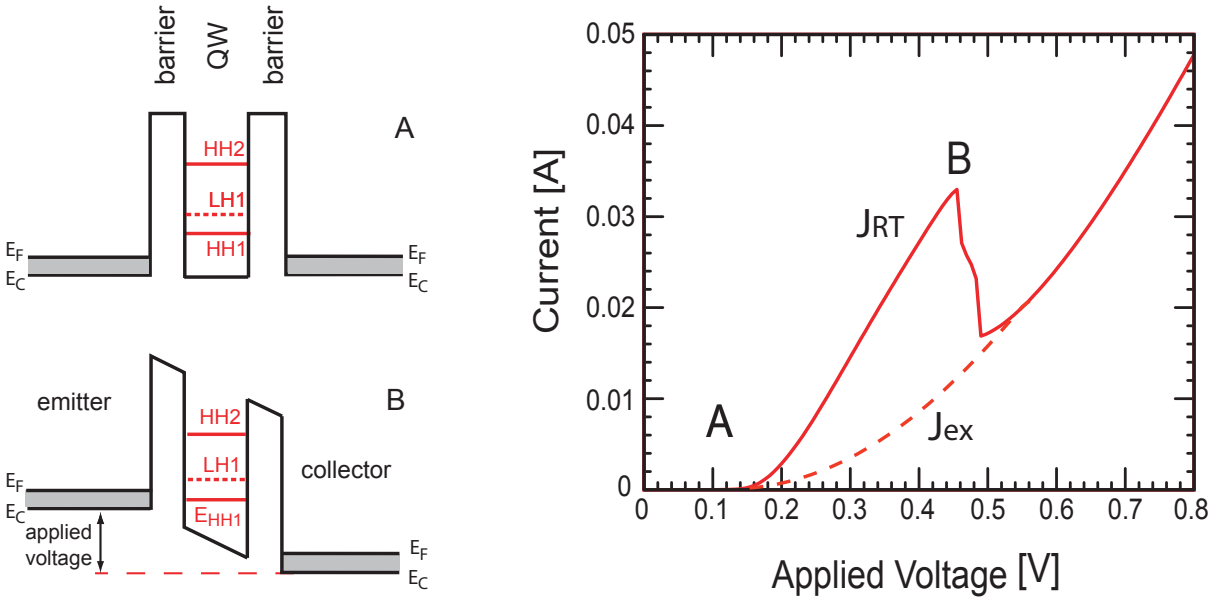

Figure 6.11: Schematic drawing of the band structure with and without applied voltage and a typical IV characteristic of a RTD structure.

ent applied voltages is shown and the corresponding points (A,B) in the Voltage-Current (VI) characteristic are marked. Without a voltage applied (A), the Fermi level E_F of the emitter states is energetically below the quantized states in the well. Thus, no tunnelling through the barriers with momentum and energy conservation is possible which prevents current flow in the structure. When a voltage is applied, a small, exponential current (J_{ex}) starts to flow. The latter one results from tunnelling processes through the whole structure including barriers and QW. It enables to identify current contributions aside the resonant tunnelling like direct tunnelling through the barriers or interface roughness and impurity assisted tunnelling as well as leakage currents. The latter ones permit to draw conclusions regarding to growth quality (interfaces, waviness) and process control. Whenever the Fermi level of the emitter (incident) states (E_F) starts to align with a confined level in the quantum well (e.g. E_{HH1} in Fig. 6.11B), the current J_{RT} increases strongly until resonance (B). At this point, the transmission probability for the carriers to tunnel through the structure is enhanced. This effect can be understood in analogy to the photon transmission in Fabry-Perot interferometers: At resonance, the positive interference of the emitter wave and the wave reflected from the second barrier results in a strong increase of the transmission. This resonance transmission can be orders of magnitudes higher than under off-resonance conditions. With further increased bias, the current suddenly drops as the resonance detunes which leads to a negative differential resistance (NDR) as shown in Figure 6.11. The external voltage V needed to shift the emitter states relative to the confined QW states (e.g. $\Delta E = E_F - E_{HH1}$) gives informa-

tion about the position of the electronic states in the QW. To relate the external voltage to the QW states, the thickness of the different layers as well as space charge effects due to charge accumulation in the emitter and the QW need to be taken into account. In most cases, this is expressed by a linear lever factor c which is discussed in more detail in the next section. Section 6.4.2 summarizes the transport measurements carried out in the frame of this work.
Another important question which can be answered using these structure is the role of the light holes in SiGe quantum cascade structures. As shown by the example of the benchmark structure (section 6.1), the LH states are usually lying in between the HH levels which are used as laser states. For a proper injection into the HH states it is desirable to avoid losses by carriers tunnelling into LH states. Besides using the comparison with calculations, the nature of the peaks observed in the VI characteristics of the RTDs can be identified by employing different sample designs (section 6.4.2) and by performing additional magneto-tunnelling experiments (section 6.4.3).
The investigated samples were grown by MBE on strain compensated $Si_{0.5}Ge_{0.5}$ pseudo-

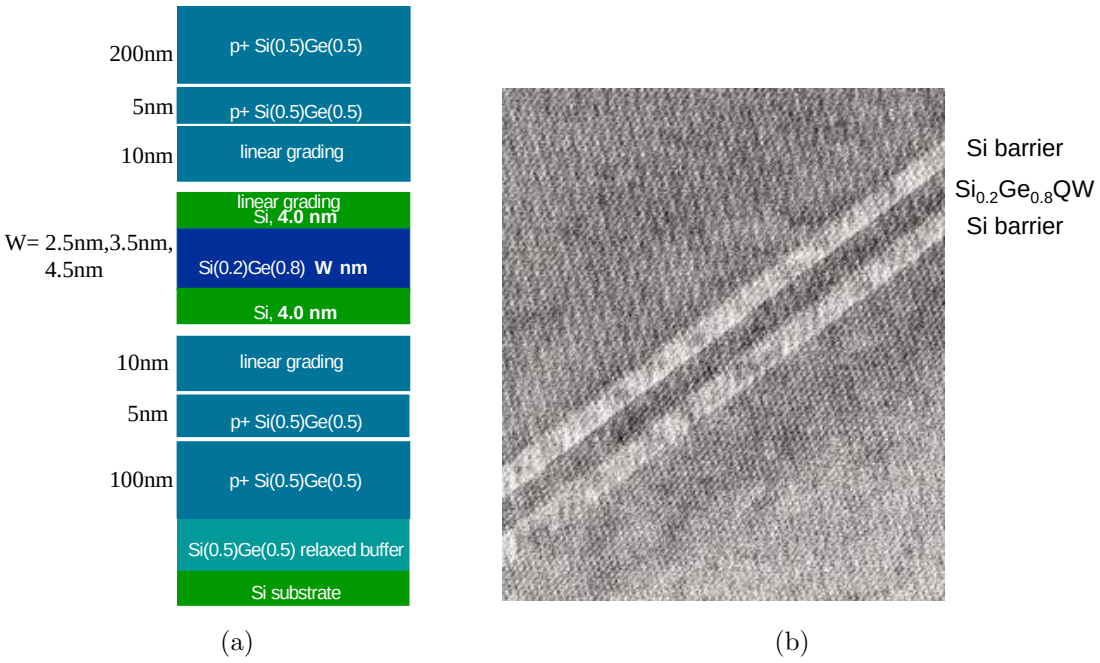

Figure 6.12: (a) Schematic drawing of the RTD structure as grown by MBE. (b) TEM cross section for one samples. The bright areas are the silicon layers, the dark regions indicate the germanium reich layers. The picture shows the good growth quality by uniform layers and sharp interfaces.

substrates of which the top layer is doped at $p = 1 * 10^{19}\text{cm}^{-3}$. The width of the $Si_{0.2}Ge_{0.8}$ QW is varied between 25Å, 35Å and 45Å. The width of the barriers at both sides of the QW was kept to 40Å. This active part was embedded into a 150Å wide emitter region whose Ge content was ramped from 50% to 80% or 60%, respectively. The first 100Å (closest to the barriers) of these ramped layers are undoped spacer layers followed by a 50Å p-doped layer ($p = 1 * 10^{19}\text{cm}^{-3}$). The 2000Å thick cap layer was doped at the same level. A schematic drawing of this type of samples is shown in Figure 6.12a. In the

TEM cross section in Figure 6.12b, the wells and barriers are clearly defined proving the good growth quality achieved for these samples. For the measurements, the samples were processed into small mesas with diameters varying between 10μm to 200μm. For the top and bottom contacts, Al pads were evaporated and annealed for 30s at 350°C in forming gas. The temperature was slowly ramped up in order to prevent thermal stress on the structures.

6.4.2 Transport measurements

In Figure 6.13a, the calculated band structure of the 35Å QW sample with an 80% Ge emitter is shown as an example. In the corresponding IV curves for different sample sizes measured at $T = 77$K (Fig. 6.13b), three well resolved resonances can be observed. The

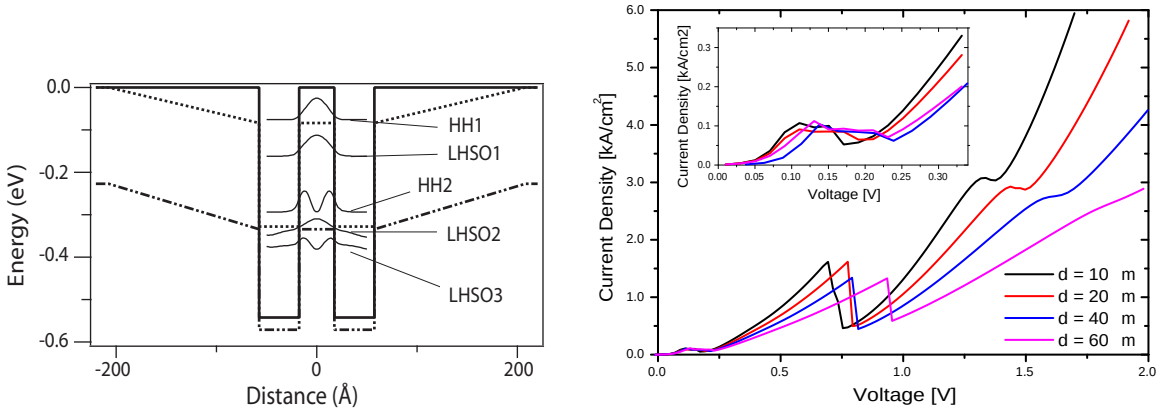

(a) (b)

Figure 6.13: (a) Schematic structure for the 35Å QW RTD as published in [111]. The solid line indicates the HH band edge, the dotted line the LH band edge and the dash-dotted line the split off band. The graded emitter is shown for clarity an the energy states at $k = 0$ are plotted. (b) The size dependent IV characteristics for the same sample. In the inset the voltage area below 0.35V is zoomed out in order to make the first resonance visible.

variation of the resonance voltages with diode diameter are due to the contact layer resistance from the substrate. The zero diameter resonance voltage was determined from the extrapolation of the values for the different sizes. It was found that the resonance voltage for the 10μm diode was only negligibly shifted from the zero-value. Therefore, the comparison of the different samples was performed using the values of the smallest diode. For all samples, injection current densities up to 3kA/cm^2 at resonance could be achieved and a peak-to-valley ratio up to 5 : 1 was found. This result encloses low leakage currents and therefore, proves the good growth quality and the well controlled processing of the small mesas.

In Figure 6.14a, the IV curves of the 3 initial samples with 80% Ge emitter and a QW width of 25Å, 35Å and 45Å are shown. Up to three resonances can be resolved for the two wider samples, only two for the 25Å QW. The measured resonance voltages versus the QW width are plotted in Figure 6.14b (markers with error bars). On the right hand scale,

the corresponding energies are given. The measured resonance voltages can be directly transformed into an energy shift via the so-called lever arm which is calculated using the following assumptions: The voltage drops linear over the structure and the collector. The emitter is considered to be flat except the region right before the first Si barrier (~ 100Å) where a 2DHG is formed as confirmed by magneto-tunnelling experiments with the B-field parallel to the current [111], [35]. The difference between the quantum well energies and the emitter states (ΔE) can be assumed to be proportional to the applied voltage: $\Delta E = c * V$. The factor c is the linear lever arm which describes the ratio between the energy drop between the emitter and the center of the quantum wells and the applied voltage. In [111], different approaches for the determination of the lever arm (like using a self-consistent poisson solver, magnetic measurements or geometrical considerations) have been compared. It was found that the simple geometrical lever arm model is in good agreement with the other two, more sophisticated, methods and therefore chosen in the frame of this work. Using this, the lever arm can be determined from the well, barrier and collector thicknesses, giving a value of about 0.4 in our samples.

In Figure 6.14b, the measured resonance voltages are plotted together with the calculated

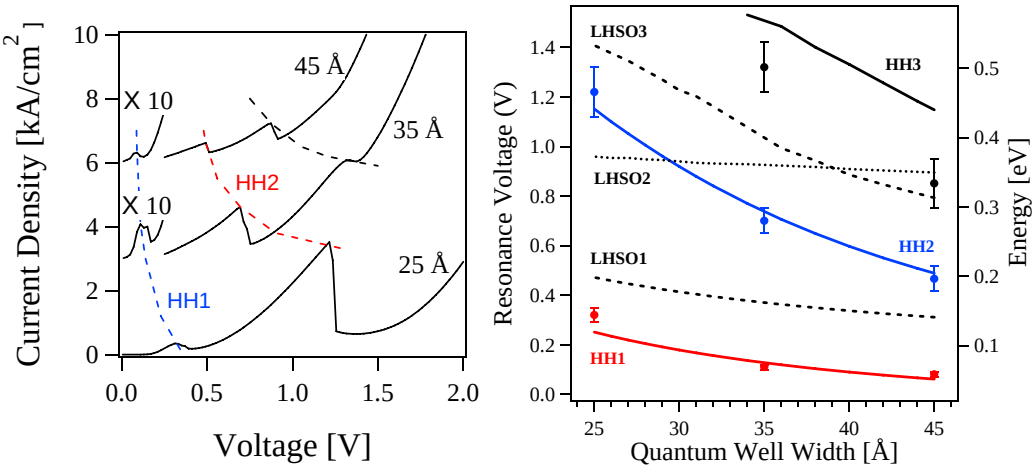

(a) (b)

Figure 6.14: (a) Current-voltage characteristics for diodes with different well width. The curves are shifted for clarity and the lowest resonance is magnified. The dotted lines are guides for the eye to the shift of the resonances (b) Confinement shift of the measured resonances (symbols with error bars) for the three QW widths investigated. The calculated energy levels in the QW are represented by solid/dashed lines. [111]

electronic states (solid/dashed lines). For the different well widths, a clear confinement shift is observable. In the following, the assignment of the observed peaks to the calculated electronic levels is discussed:

The shift of the first (red markers) and the second (blue markers) resonance are in good agreement with the calculated values for the HH1 (red line) and HH2 (blue line) states. Furthermore, the difference between the first two resonances is increasing with decreasing well width what can only be observed for states having different index. This suggests the assignment of the first two resonances to the HH1 and HH2 level, respectively. However,

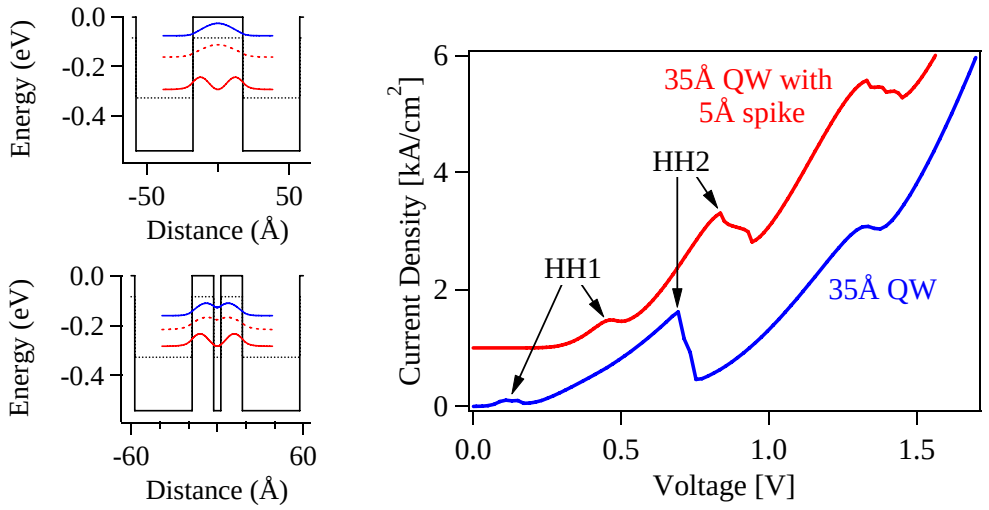

Figure 6.15: (a) Band structure for diode without and with spike, respectively. The blue line indicates the first order level HH1. The dashed red line refers to the LH level, the solid red one to the HH2 state. (b) The corresponding IV characteristics for both samples in comparison at $T = 77$K. [111]

the calculated levels plotted in Figure 6.14b show that the LH states are lying close to the first two HH states. Considering the simplicity of the lever arm model (i.e assuming a voltage independent lever arm), the above assignment to HH1 and HH2 states can only give an indication about the nature of the resonances. Therefore, further evidence for the chosen assignment is desirable. For this purpose, an additional sample with a central potential spike (obtained from a thin Si layer of 5Å) inserted in the middle of the 35Å QW was investigated and compared to the initial 35Å RTD. The schematic band structures for these two samples are shown in Figure 6.15a. The central spike will shift the resonances towards higher energies. However, even symmetry states like HH1 (blue solid line) and LHSO1 (dashed red line) with the maximum of the wave function in the middle of the quantum well will be more affected than odd states (e.g. HH2) [112]. The comparison of the IV characteristics of both samples (see Fig. 6.15b) clearly shows the shift of the resonances. The first resonance shifts of about 0.36V while for the second one a shift of only 0.11V was found. The third resonance however is not affected by the spike. On the basis of this observation, two possible approaches for the assignment of the resonances need to be discussed:
The first approach is using the assignment stated before from Figure 6.14b with the first two resonances as HH1 and HH2, respectively. The calculated shifts expected from the central potential spike are 0.3V for the HH1 level and 0.08V for the HH2 state. This agrees well to the measured values (0.36V for the first resonance and 0.11V for the second one). The third resonance should consequently be assigned to the HH3 state. However, a conclusive experimental and theoretical prove for the latter assignment is still missing.
At that point, another hypothesis of peak assignment needs to be considered. The following one would allow a direct assignment of all three resonances including the third

one observed at 1.35V (Fig. 6.15): The first resonance corresponds to HH1 on which the central spike has most impact. The second one is referring to the LHSO1 state which is only slight influenced by the spike. Finally, the third resonance can be interpreted as HH2 which is not shifted by the Si barrier. With this assignment, the shift expected from the potential spike was calculated. From this, a shift of $\geq$ 0.2V for the LHSO1 level is obtained, which is double as high as the experimental value (0.11meV) obtained for the second resonance.

This discussion shows that a final clear assignment requires improved calculations taking into account a more sophisticated treatment of the electric field, i.e. considering depletion of the structure or accumulation of carriers inside the well. However, from the results obtained so far, the assignment of the first two resonances to HH1 and HH2 is more feasible, especially when the confinement shift (Figure 6.14b) is taken into account. The increasing difference between the first two resonances with decreasing well width clearly identifies states with different index. This behavior can not be explained when the second resonance is assigned to the first LH state. In the following, we therefore apply the first way for the assignment of the resonances to the electronic levels (i.e. first resonance originates from the HH1 state and the second one to the HH2 state).

With the above assignment, the question for the reason of the missing LH tunnelling

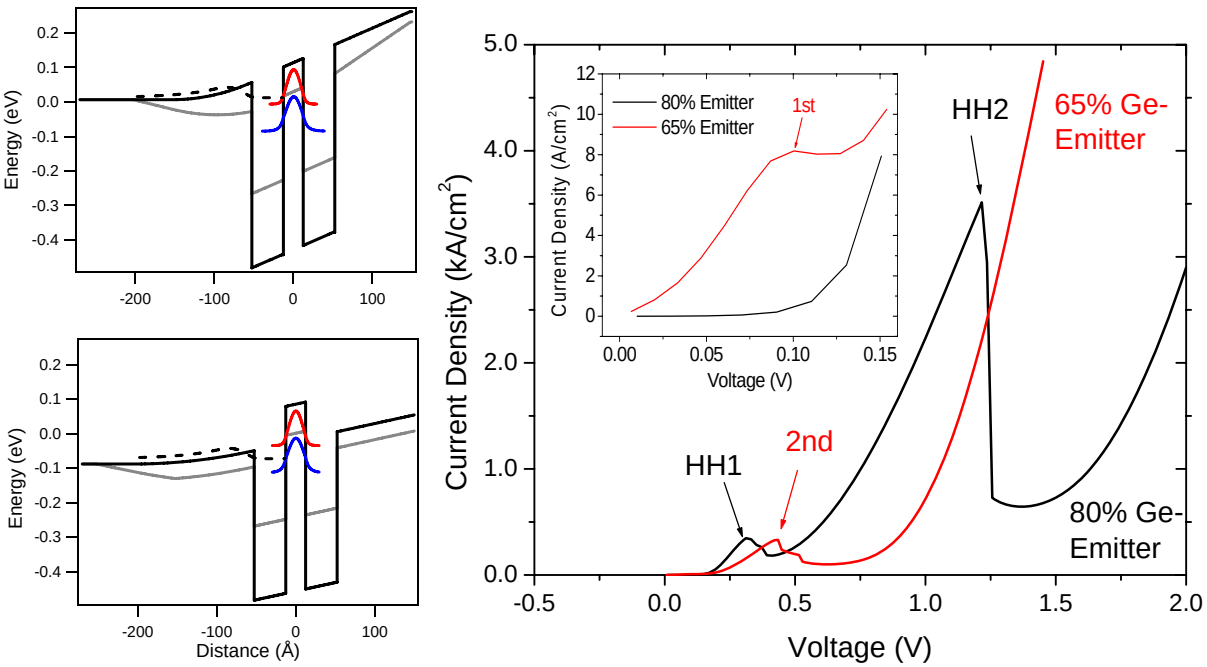

(a) (b)

Figure 6.16: (a) Band structure of the sample with 80% germanium emitter (up) and 65% germanium emitter (down). The HH potential (thick black), the LH potential (thick grey), the HH1 state (red) as well as the LH1 state (blue) are indicated. The dashed line represents the confined emitter state wave function. (b) IV characteristics of both samples at 77K. The inset shows a magnification of the voltage area below 0.15V for the first resonance of the 65% emitter sample. [111]

arises: In former publications (e.g. [113], [114], [115]), tunnelling into LH states has been observed. The question arising from the first way of assignment is: Why should the LH tunnelling be missing? The main difference compared to the former publications can be found in the lower strain of those structures. Therefore, samples having emitter regions with 65% Germanium were grown and compared to the initial samples with 80% Ge emitter as described in the next section.
The calculated band structures and the IV characteristics for the 65% and the 80% emitter sample are shown in Figure 6.16. For the 65% Ge sample, two resonances at ~ 0.1V and ~ 0.47V were observed. The second one compares well to the HH2 level as expected from the calculation while the assignment of the first one is not that straightforward. As shown in Figure 6.16a, the Fermi level of the emitter state is designed to be above the first HH state at zero bias, hence the tunnelling into the latter one should be prohibited by design. On the other hand, one can not completely exclude this process due to the uncertainty in the discontinuity of the bands. However, comparing the difference between the first two resonances ($\sim$ 370meV for the 65% Ge emitter sample and $\sim$ 850meV for the 80% sample) which is a factor 2 different, the first peak is unlikely to be the HH1 resonance. Therefore, this peak was tentatively assigned to carriers tunnelling into the LHSO1 state. To further investigate the nature of this resonance, magneto tunnelling experiments were used as described in the next sections.

6.4.3 Magneto-Tunnelling

For an introduction to the magneto-tunnelling, a brief overview about the effects of a magnetic field on a semiconductor band structure will be given. Subsequently, the magneto tunnelling experiments on the described RTD samples will be discussed.

Magnetic field effects

The effects of a magnetic field applied to SiGe RTDs have been studied e.g. by *Schuberth et. al* [115], *Gennser et. al* [116] and *Zaslavsky et al.* [117]. In that case, the direction of the magnetic field needs to be taken into account. One has to distinguish between parallel and perpendicular field relative to the current. With a magnetic field parallel to the current, the emitter and QW states are split into Landau levels whereas a perpendicular field causes the tunnelling at higher in-plane momentum and allows e.g. to map out the subband dispersion.
In presence of a magnetic field, the Schrödinger equation reads as follows:

$$\Big(\frac{1}{2m_0}(p - qA)^2 + g_j \mu_b m_j B + V(\mathbf{r})\Big)\Psi(\mathbf{r}) = E\Psi(\mathbf{r}) \tag{6.1}$$

with μ_B as Bohr magnetron, g_j the Landé factor, m_j the spin quantum number and A the vector potential of the magnetic field. Assuming the crystal potential $V(\mathbf{r})$ to be constant

(i.e. in the bulk, ignoring crystal effects), the systems eigenvalues of the energy are:

$$E_{n,\pm}(k_y) = \left(n + \frac{1}{2}\right)\frac{e\hbar B}{m_0} + \frac{\hbar^2 k_y^2}{2m_0} \pm \frac{1}{2} g_j \mu_b B \tag{6.2}$$

for a magnetic field in y-direction, $\pm$ for spin up and down and n is a positive integer. Only the motion in y-direction is undisturbed while the motion in the x-z plane is quantized into Landau levels with index n.
When a magnetic field is applied to a QW, the carriers start to move in cyclotron orbits. In the case of a **magnetic field perpendicular to the current** (parallel to the interfaces), the cyclotron orbits are hindered by the well potential. As long as the magnetic energy $e\hbar B/m^*$ is much smaller than the subband spacing, the magnetic field only acts as a small perturbation on the energy levels[1]. At attainable field, the stronger effect in this configuration is the shift in k-space which the holes experience during the tunnelling process due to the Lorentz force (semiclassical picture). This situation is schematically shown in Figure 6.17. The magnetic moment adds a parallel momentum to the holes while

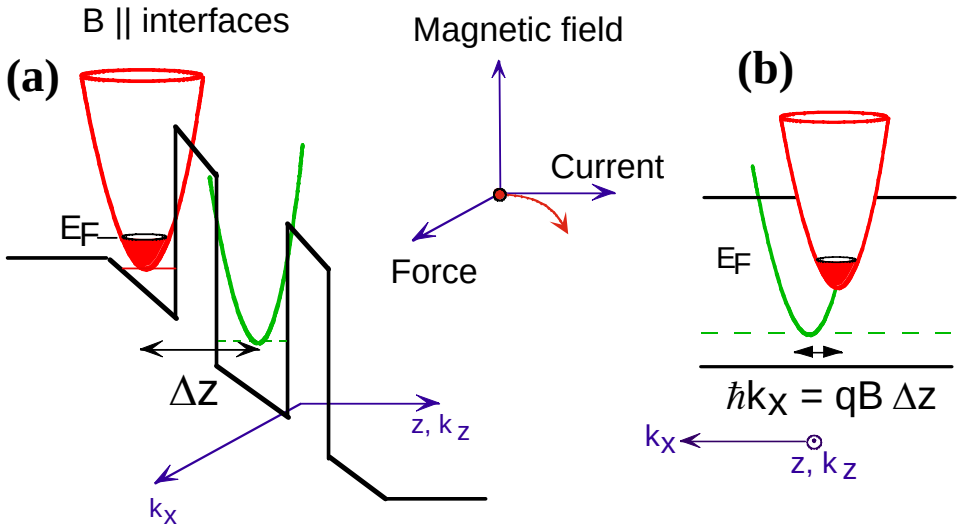

Figure 6.17: Schematic drawing of the effects of a magnetic field parallel to the interfaces. The carriers tunnel from the emitter states to the QW passing a distance Δz (a). Due to the magnetic field, the carriers are shifted in k-space (b).

tunnelling and shifts the emitter k-space parabola relative to he well state dispersion. The shift in k-space due to the B-field is describes by the following term:

$$\Delta k_y = \int \frac{eBv_z}{\hbar} dt = \frac{eB\delta z}{\hbar} \tag{6.3}$$

which gives for parabolic bands:

$$\Delta E = \frac{(eB\Delta z)^2}{2m_0} \tag{6.4}$$

[1]For very high magnetic fields, the cyclotron orbit is of the size of the quantum wells and the B-field effects become important.

where Δz is the tunnelling distance. Therefore, a higher bias voltage has to be applied to match the emitter states with the well states at higher k. In that way, the dispersion of a state in a QW can be mapped [114].
For a **magnetic field applied parallel to the current** (perpendicular to the interfaces) the cyclotron orbit is not restricted by the potential well and Landau level quantization takes place. The in-plane motion is motion of the carriers in a QW is now restricted by the magnetic field itself creating a quasi-zero dimensional system. The density of states in the well consists of delta-like functions which represent the different Landau levels. The conservation rule of the in-plane momentum during tunnelling is transformed into the conservation of the Landau level index n. The separation of these levels is $\hbar * \omega_c(n + 1/2)$ with ω_c the cyclotron frequency determined of the magnetic field $\omega_c = eB/m$. With the sweep of the field, the Landau levels will one by one be emptied as they pass the Fermi energy which makes the currents oscillate with a period $1/B$. These Landau levels are further split up due to the Zeeman (or spin) effect which is depending on the scalar product $\mathbf{J} \bullet \mathbf{B}$ with $\mathbf{J}$ as the total angular momentum. The energy splitting is then given by

$$\Delta E = \mu_B * g_j * m_j * B \tag{6.5}$$

with μ_B as Bohr magnetron, g_j the Landé factor and m_j the spin number. As the Landé factor is depending on the vector $\mathbf{J}$, the latter one defines the splitting.

Magneto-tunnelling Experiments

On the basis of the above theory, the IV characteristics of the 65% and 80% Ge emitter sample with applied magnetic field are analyzed. In these experiments, a magnetic field perpendicular to the current ($B \perp$) was applied. In the following, only the effects on the first resonance will be discussed as the measurements for the second one did not give interpretable data. In Figure 6.18, the shift of the first resonances with the magnetic field is shown. For the 80% emitter sample, a parabolic shift has been observed while for the 65% emitter sample a linear shift was obtained. A log-log plot clearly demonstrates these dependencies (Figure 6.19). The investigation of the first resonances (HH1) of the three initial 80% Ge emitter samples [116] showed a parabolic dependence of the resonance shift on the magnetic field and the deduced effective masses were in good agreement with the calculated dispersion. Hence, the parabolic behavior is due to the bending of the subbands in k space which proves the tunnelling of confined emitter states into the subbands in the QW. However, for the explanation of the linear dependence on $B \perp$ of the 65% emitter sample, the tunnelling of confined carriers is not valid. To verify this, the impact of the above explained effects is discussed in order to find possible linear contributions.

- The formation of Landau levels in the QW or in the emitter well (see e.g. Figure 6.16a and 6.17a; the emitter well is the V-shaped well formed by the electric field and the left barrier) is not possible with a magnetic field parallel to the interfaces as the cyclotron orbit at high fields (up to 23T in our experiments) is much

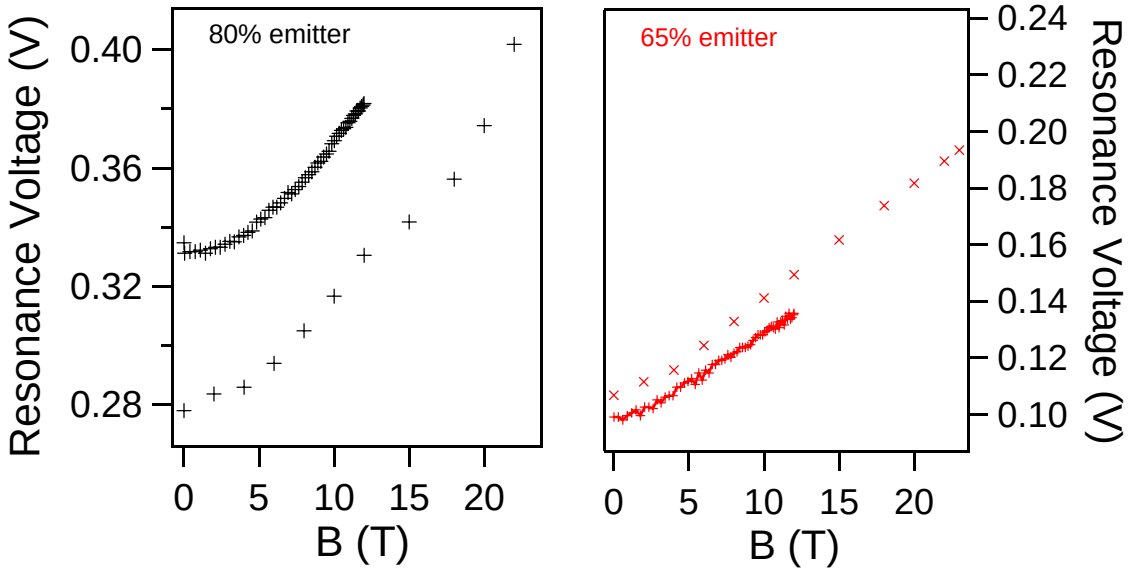

Figure 6.18: Dependence of the first resonance on a magnetic field parallel to the interfaces for both samples. Two measurements for different diodes are shown with magnetic field up to 12T and 23T, respectively. [111]

larger than the width of the wells. Hence, any Landau level effect will be small, perturbing and therefore at least quadratic with B.

- The Zeeman effect was given by $\mathbf{J} \bullet \mathbf{B}$, plus an additional small term proportional to B^2 giving a parabolic contribution only [120]. In our configuration, the **J** vector is frozen in by the confinement and the strain in the growth (z) direction as these two components give much larger energies than the magnetic field. By taking the scalar product, the Zeeman effect will be zero in the QW and the emitter well due to strain and confinement.

- The acceleration in k-space can also be excluded to give a linear contribution as the levels are quite parabolic as confirmed by the calculations.

From these explanations it can be stated, that there are no linear effects in dependence on $B \perp$ as long as the carriers are confined. The linear behavior can only be explained, if one takes into account the carriers tunnelling from the unstrained bulk part ('flat' part, no band bending) of the emitter into the QW states. In that case, both Landau levels and Zeeman effect will give a linear contribution as the **J** vector is free to turn along the B axis and align along the x-axis. Therefore, the quantum well state will see a mixed HH/LHSO state coming from the emitter which will enable the tunnelling into the first LHSO state of the quantum well. Furthermore, the barrier for the bulk holes is smaller due to the lower Germanium content in the emitter so that they can either tunnel directly into the QW states or form hybrid states with the HH emitter states. Calculation of the Landau level separation in the $Si_{0.5}Ge_{0.5}$ bulk gives a slope of ~ 0.6meV/T and the Zeeman energy a

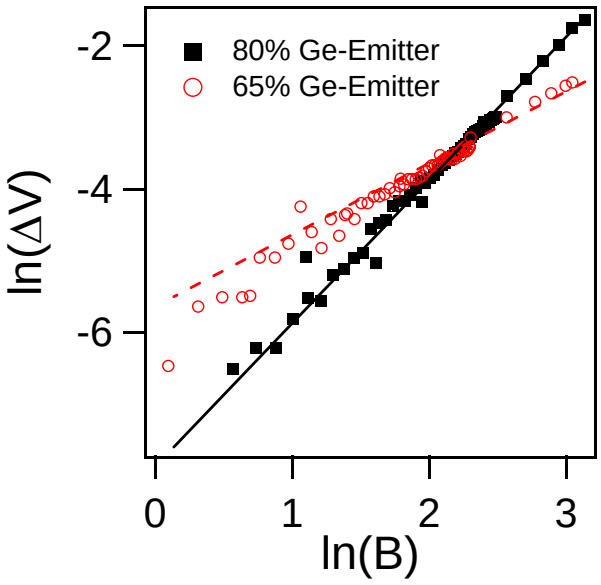

Figure 6.19: Logarithm (ln) of the resonance voltage difference $\Delta V = V(B) - V(B = 0)$ versus log of the magnetic field parallel to the interface, for the 80% (filled dots) and 65% Ge emitter sample (open dots). Lines $d(ln(\Delta V))/d(lnB) = 1$ (black line) and $d(ln(\Delta V))/d(lnB) = 2$ (red line) are shown as guide for the eyes. [111]

factor 2-10 smaller. The big variation of the latter one is due to the interpolation method used between Si and Ge for the material parameters [81]. This compares reasonably well with the measured slope of 4.1mV/T which corresponds to a level increase of 1.4meV/T. From these consideration it is reasonable to assign the first peak in the 65% emitter samples to bulk carriers tunnelling into the LHSO1 state. Furthermore, it shows that the LH tunnelling observed in other p-type RTDs was due to the bulk emitter states and enabled by the lower barriers for the holes resulting from less strain present in these samples.

In summary, the following results were obtained from the resonant tunnelling structures: An effective injection from the confined emitter states into HH states is possible what is proven by the best peak-to-valley ratio of 5 : 1 achieved in our structures. For the 25Å, 35Å and 45Å RTDs with 80% emitter, a clear assignment of the first resonance to the HH1 state could be made. Preliminary calculations suggest the assignment of the second resonance to the HH2 level. This results would imply the absence of tunnelling through LH states in that kind of samples and therefore the possibility of a proper injection into HH states despite interspersed LH levels. Beyond this, conditions for LH tunnelling could be mapped out which gives means for a better control of the role of the LH states in quantum cascade structures.

6.4.4 Barrier Thickness Dependence

The dependence of the IV characteristics on the barrier thickness is of interest in these structures as from the results a conclusion may be drawn regarding to the injection barriers

for quantum cascade structures. The thickness of the barriers defines the coupling between

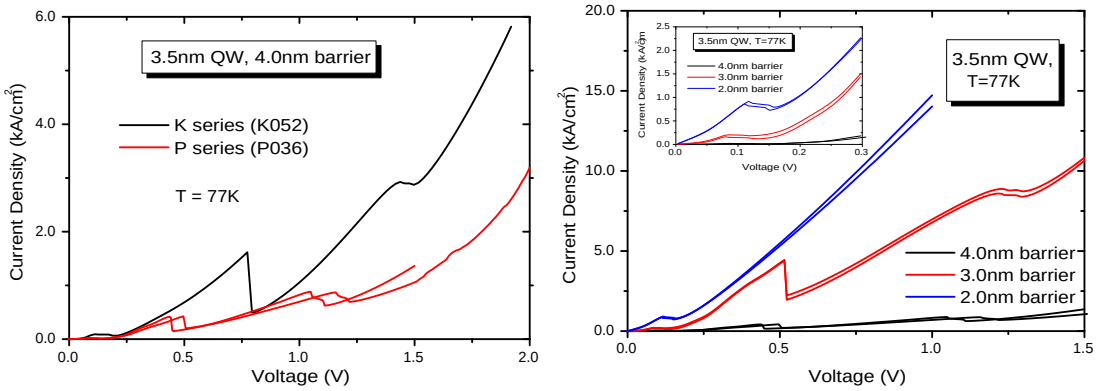

Figure 6.20: (a) Comparison of the IV characteristic of the old (K-series) and new (P-series) 35Å QW RTD with 40Å barriers. The second resonance is down shifted of about 0.3meV compared to the old sample. The peak-to-valley ratio for this resonance is about 3 : 1 in both samples. (b)IV characteristics for the 35μm devices with different barrier thickness at $T = 77$K. The inset shows a magnification of the low voltage area in order to show the first resonance.

the quantum well and the emitter states what can be especially interesting with respect to HH states in the LH continuum. Therefore, a set of RTDs with a 35Å QW and barrier thicknesses of 20Å, 30Å and 40Å was grown. The latter one corresponds to the structures investigated above. However, it has to be mentioned in the beginning that this new sample does not compare to the old one in its performance (see Figure 6.20a). Although the peak-to-valley ratios for both samples were in the same range (~ 3), the total tunnelling current for the new sample was a factor ~ 4 smaller than for the old one. Additional, a shift in the resonance voltage and an asymmetric behavior for different voltage directions indicates bad growth conditions and hence, wavy and non-uniform structures with fields of strain accumulation. Therefore, the following discussion can only be taken as a preliminary result as a confirmation by further measurements is necessary.
In Figure 6.20, the IV characteristics for the three samples for mesas with a diameter of 20μm are shown. For thinner barriers, the total current increases as expected. It is also obvious, that for the thinnest barrier of 20Å the second and third resonance are not visible as additional current components are too high. For the two other samples, all three resonances can be observed and the resonance voltages are comparing well to each other (see Fig. 6.21a). The peak-to-valley ratios however are constantly improved with thicker barriers. From Figure 6.21b it can be found that the reduced coupling to the emitter enhances the pure tunnelling current. This can be understood as thinner barriers enable additional tunnelling processes due to interface roughness and direct tunnelling through the barriers. Further research regarding the optimization of the tunnel barrier thickness and therefore the optimum coupling between emitter and quantum well should be directed to the investigation of thicker barriers. A trade-off needs to be found between injection current densities and the amount of proper tunnelling given by the peak-to-valley ratio.

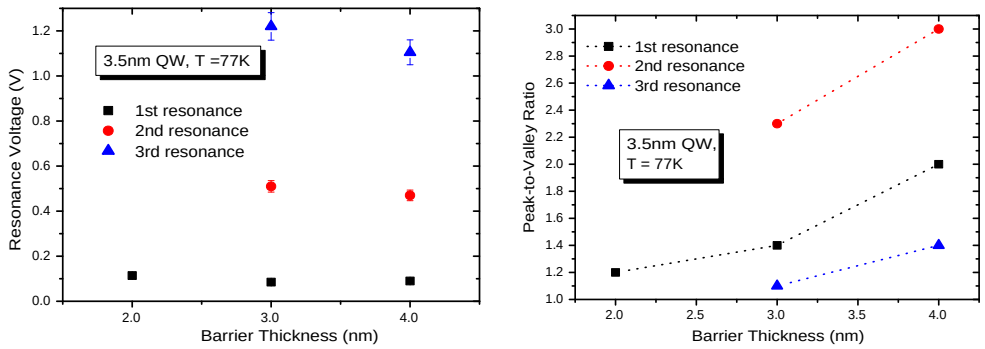

Figure 6.21: Resonance Voltage and Peak-to-Valley ratio versus barrier thickness.

6.4.5 Injection Barrier Thickness

Here, the investigations regarding the influence of the injection barrier on the EL performance are discussed briefly. However, these results can only be taken as preliminary as the EL measurements showed a poor performance. Possible reasons are problems in processing the small finger structures as well as poor growth conditions. Furthermore, the investigated samples were grown in different series with a time difference of more than 1year which makes a comparison even more complicated.

For the influence of the injection barrier thickness on the electroluminescence two addi-

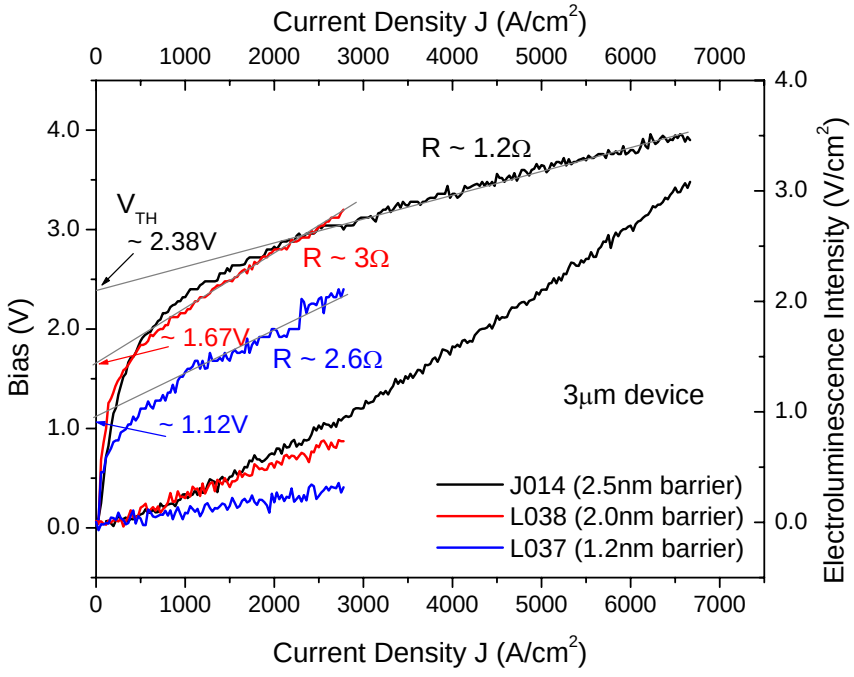

Figure 6.22: Influence of the injection barrier width on the L-I an V-I characteristics. The L-I and V-I curves were taken under similar conditions. The threshold voltage and the serial resistance of the devices are indicated.

tional samples with barrier width changed from 25Å in the benchmark structure (Sample A) (first layer in the growth sequence given in 6.1) to 20Å (Sample B) and 12Å (Sample

C), respectively. The two latter structures consist of 12 repetitions of the active region in contrast to the benchmark structure with 15 periods which has to be taken into account for the threshold calculation. The samples were processed into 3μm finger structures and measured at low temperature. The obtained IV and LI characteristics compared to the initial sample are shown in 6.22. The threshold voltage for the benchmark is $\sim$ 2.4V and $\sim$ 1.7V and $\sim$ 1.1V for the 20Å and 12Å sample, respectively. The calculated onset is 4.25V for the 15 period sample and $\sim$ 3.4V for the 12 period samples. Hence, Sample A and B show a factor 2 difference between the calculated and measured threshold while the threshold for Sample C is a factor 3 lower than expected. It is assumed that the 1.2nm injection barrier is too thin giving rise to additional current components like direct tunnelling through the barriers and interface-roughness assisted tunnelling preventing a proper injection. Besides this, the serial resistance of Samples A and B which is deduced from the slope of the IV curve is a factor 2 to 3 higher than for the initial Sample A probably due to high leakage currents which can result from processing induced or growth related defects. The LI curves confirm this observation: They show a linear behavior up to 3kA/cm^2, indicating intersubband emission. Spectra taken at higher current densities however showed that the emission is mainly due to heating. This heating appears to be stronger in the samples with thinner injection barrier which is another indication for higher leakage currents. For a final conclusion however, more data is needed and further samples have to be investigated.

6.5 Conclusion on electrically pumped structures

As a summary, the characteristic state-of-the-art values of the SiGe bound-to-continuum benchmark structure are given. On the gain side, linewidths of Γ = 45meV, injection current densities of J = 6.5kA/cm^2, upper state lifetimes τ_{up} of 100fs as obtained following the method described in [36] and upper state concentrations $n_{up} \leq 3 * 10^9$cm^{-2} have been determined. This results in a peak gain achievable with our state-of-the-art structures of 2cm^{-1}. This value has to be compared with the losses in the active region material due to the Drude-type absorption implying the ratio of energy and relaxation time $\omega\tau$ ($\sim$ 3) defining the energy dependent Drude mobility, the injection density $N_{inj} = 1.5 * 10^{17} cm^{-3}$ and the effective mass ration m^*/m_e of 0.2 resulting in a material loss of about 15cm^{-1}. This shows that the gain needs to be improved by at least a factor of $\sim$ 10 in order to achieve lasing assuming that the 2D contact layers scheme with a Germanium top layer for guiding is employed. This, in principle should not add much to the Drude absorption in the active layers but reduce the losses in the waveguide. Regarding to this, the main approaches remain the improvement of the linewidth mainly by an optimized growth, longer upper state lifetimes and the optimization of the injection respective resonant tunnelling current.
The realization and optimization of an active region for electrically pumped structures regarding the above mentioned approaches implies several obstacles:

- The need of electrical contacts requires a sophisticated waveguide design and process-

ing.

- The effects of material defects on the electrical properties are difficult to estimate.
- The active region consists of numerous layers which require a very precise growth for a precise band alignment. The MBE growth and optimization of such thick active regions is costly and time consuming.
- The deposition of a high quality Ge layer on SiGe is demanding with respect to interfaces.

To circumvent these substantial hindrances, another approach was chosen at that point, the optical pumping. Here, the injection of carriers into the upper laser state is not provided electrically but by an external laser excitation. This implies several advantages like e.g. no need of electrical contacts and much simpler structures with a reduced number of intermediate levels. The realization of an optical pumping setup, the achieved lasing with III-V DQWs and the design of appropriate SiGe samples will be the content of chapters 7 and 8 which form the main part of this thesis.

Chapter 7

III-V optically pumped Intersubband Lasers

In Chapter 6, the problems regarding the realization of electrically pumped SiGe cascade structures were discussed. To reduce the number of challenges connected to this goal, a new approach was chosen, the optical pumping. This method implies several advantages: Firstly, there is no need of electrical contacts as the excitation of carriers is provided by an external laser source. Secondly, the injection of carriers via a cascade structure is not necessary allowing much simpler structures. As the alignment of the injector states with the upper laser state is critical as shown before, the requirements regarding the growth quality can be relaxed for optically pumped structures as the position of the levels is not that critical. Last but not least the simpler design of these structures which usually consist of a DQW has the advantage of a decrease number of intermediate states less non-radiative paths are present which allows longer upper laser state lifetimes.
In this chapter, the investigations on optically pumped III-V structures are discussed. The first measurements were performed testing an InP based double quantum well system designed for population inversion. However, Raman lasing was obtained and investigated by using samples with slightly different design. Furthermore, time resolved measurements were performed on these DQW structures in order to gather information on the upper state lifetime. The results of the above mentioned investigations are presented in this chapter including a brief introduction to Raman lasers and their theoretical treatment.

7.1 Introduction

The first optically pumped intersubband laser emitting at 15.5μm was demonstrated in 1997 [121] and is termed Quantum Fountain Laser (QFL) since then. In contrast to the QCLs where the upper laser state is populated via resonant tunnelling from an injector region, the carriers in a QFL are excited by using an external laser source. This implies the drawback of an external source but also provides several advantages: A QCL requires a complicated design of the active region grown accurately by MBE, in order to achieve efficient injection and transport through numerous periods. Furthermore, doped injectors

and heavily doped contact layers which are necessary for a proper transport give rise to free carrier losses resulting in high optical loss. In a QFL however, the design of the active region can be simplified: As there is no injector and extraction region needed, a 3-level design is sufficient to obtain lasing. The most common way to realize the 3-level system is a double quantum well (DQW). Since no electrical contacts are necessary, the complex processing for low loss optical waveguides for QCLS can be avoided: Etching of a mesa with a mirror etching and polished facets is sufficient for the realization a QFL. Besides this, no highly doped layers for the carrier transport are necessary which reduces the free carrier loss in the structure. Since the free carrier absorption is dramatically increased towards low frequency, the QFL seemed a promising concept for the longer wavelength range above 10μm. Later on, the possibility to detune these devices from the actual lasing energy ($\hbar\omega_l$) by changing the pump laser energy ($\hbar\omega_p$) attracted interest regarding applications as well as the physical processes involved. In the work of *Lafaye et al.*, the shift of the emission wavelength with the pump energy (tuning) was ascribed to the layer thickness variations but not to a Raman process. This was stated from the fact that for the plot E_{pump} versus E_{laser} a slope of 0.72 was obtained instead of 1 as expected for the Raman gain. Furthermore, they claimed that time-resolved pump-probe measurements proved the population inversion [122]. In a subsequent work of Liu *et al.* [123] in 2001, an intersubband laser working on the Raman process was presented. Therein, a DQW system similar to the one used in [122] was employed. The difference in design was the energy spacing between the ground state and lower laser state E_{12} which was in resonance with an AlAs-like LO phonon. In that system, the Raman shift described by $\hbar\omega_l \simeq \hbar\omega_p - E_{12}$ was found when the pump energy was varied within the linewidth of the E_{13} absorption. This behavior indicates a Raman process as the lasing results from the stimulated Raman

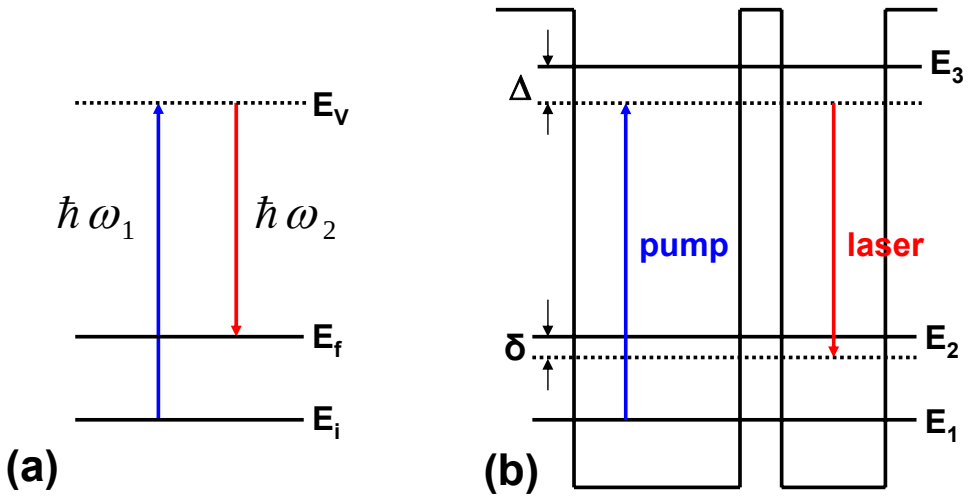

Figure 7.1: (a) Schematic drawing showing the Raman transition from the initial state E_i to the final states E_f via a virtual state E_v. (b) Analogy to the electronic states E_1, E_2 and E_3 in a DQW (solid lines) to the virtual Raman states (dashed lines). The detuning of the pump from the E_3 state (Δ) and of the signal from the E_2 level (δ) are indicated.

scattering which itself is a two-photon process (see Figure 7.1): one photon with the

energy $\hbar\omega_1$ is absorbed and one photon at the Stokes frequency of $\hbar\omega_2$ is emitted while the electron makes a transition from the initial state E_i to the final state E_f. The energy conservation then requires that $\hbar(\omega_1 - \omega_2) = E_f - E_i = \hbar\omega_{if}$. However, this transition is not completely direct but takes place via a virtual state E_v where the electron spends an extremely short time before arriving to the final state. Under certain conditions, e.g. strong pump field and strong, nonlinear coupling between the electromagnetic fields, this Raman type contribution exceeds all other losses and lasing is obtained. In that case, no population inversion in the upper laser state is required in order to obtain laser action. However, it can only be obtained in the presence of a strong optical pumping field. When the optical drive is off, population inversion is required to achieve amplification. A first theoretical comparison between the intersubband population inversion and Raman gain was performed in [124]. Applying this to the DQW structures it was found that narrow linewidths favor the Raman process and that the Raman gain can always be made positive regardless to the lower state lifetime. In the basic analysis of this system as performed in [124], the Raman gain is modelled on the basis of the Stimulated Raman Scattering (SRS). The Raman gain was found to be proportional to the pump intensity as well as to the virtual lifetime of the upper level and the effective lifetime of the lower level. However, this analysis did not take into account the nonlinear contributions of the strong electromagnetic pump field and therefore, saturation effects for high pump powers. A more precise analysis of a three level system including these effects in the solution of the density matrix and Maxwell Equations was performed in [125]. In the following, the theoretical basis for optically pumped structures will be briefly summarized on the basis of the above mentioned literature.

7.2 Theoretical models for a three-level system

The gain calculation for population inversion and Raman lasers summarized below is modelled for a three level system. In a first step the population of the subband has to be determined which are given by the diagonal elements of the density matrix. For a simple three-level system, the rate equations for the population densities in the subbands can be written as follows:

$$\frac{dn_1}{dt} = \beta(n_3 - n_1) + \frac{n_2}{\tau_{21}} + \frac{n_3}{\tau_{31}} \tag{7.1}$$

$$\frac{dn_2}{dt} = -\frac{n_2}{\tau_{21}} + \frac{n_3}{\tau_{32}} \tag{7.2}$$

$$\frac{dn_3}{dt} = -\beta(n_3 - n_1) + \Big(\frac{1}{\tau_{32}} + \frac{1}{\tau_{31}}\Big)n_3 \tag{7.3}$$

Here, τ are the intersubband relaxation times and $\beta = \Omega_p^2 T_2/2$ with the dephasing time $T_2 = 2\hbar/\Gamma$ and Γ the full width at half maximum. The population distribution due to the external pump is described by the terms including the Rabi-frequency of the pump Ω_p which is given by:

$$\Omega_p = ez_{13}E_p/\hbar$$

with e as electric charge, z_{13} the optical matrix element of the E_{13} transition and E_p the peak electric field calculated from the pump intensity:

$$I_P = \frac{1}{2}\varepsilon_0 cn|E_p|^2$$

where ε_0 is the dielectric constant, c the vacuum light speed and n the refractive index. Using the sum rule $n_1 + n_2 + n_3 = 1$ and assuming a steady state distribution in the DQW, the solution for the population of the subbands can be found:

$$n_1 = \frac{\beta + \frac{\tau_{21}}{\tau_{32}^2} + \frac{1}{\tau_{31}}}{\beta\left(2 + \frac{\tau_{21}}{\tau_{32}}\right) + \frac{\tau_{21}}{\tau_{32}^2} + \frac{1}{\tau_{31}}} \tag{7.4}$$

$$n_2 = \frac{\beta\frac{\tau_{21}}{\tau_{32}^2}}{\beta\left(2 + \frac{\tau_{21}}{\tau_{32}}\right) + \frac{\tau_{21}}{\tau_{32}^2} + \frac{1}{\tau_{31}}} \tag{7.5}$$

$$n_3 = \frac{\beta}{\beta\left(2 + \frac{\tau_{21}}{\tau_{32}}\right) + \frac{\tau_{21}}{\tau_{32}^2} + \frac{1}{\tau_{31}}} \tag{7.6}$$

From this, the total number of carriers in the subbands can be calculated by $N_1 = n_1 * N$, $N_2 = n_2 * N$ and $N_3 = n_3 * N$ with N as the carrier density. On the basis of these equations, a brief overview over the theoretical description of the two processes (population inversion and Raman) is given in the following.

7.2.1 Population Inversion Gain

In an optically pumped population inversion laser, the basic process taking place is the absorption of one photon with the energy of the pump and the subsequent emission of a photon with an energy in resonance to the E_{32} transition. As the population inversion laser is bound to electronic states, the emission wavelength is fixed to the E_{32} resonance. The basic requirement for this is the population inversion which is determined by the difference between the population in the upper state and in the lower state. According to [124], the gain in the structure is given by the population difference and the differential cross section σ_{ul}:

$$g_{PI} = \sigma_{32}(n_3 - n_2)$$

where

$$\sigma_{32} = \frac{4\pi\alpha_0}{n}\frac{\hbar\omega_{13}}{\Gamma_{13}}z_{32}^2$$

with z_{32} the optical matrix element of the E_{32} transition, Γ_{13} the measured linewidth of the E_{13} pumping transition and $\hbar\omega_{13}$ the pump energy. $n_3 - n_2$ can be calculated from the subband populations given by the equations 7.6 and 7.5:

$$n_3 - n_2 = \frac{4\pi\alpha_0}{n}\frac{I_P}{\Gamma_{13}}z_{13}^2 * N(\tau_u - \tau^\star)$$

where the upper state lifetime τ_u and the lower state lifetime $\tau^\star$ are determined as follows:

$$\tau_u = \left(\frac{1}{\tau_{32}} + \frac{1}{\tau_{31}}\right)^{-1}$$

$$\tau^\star = \frac{\tau_{21} \cdot \tau_u}{\tau_{32}}$$

This leads to a final expression for the lifetime difference between the lower and upper level given by:

$$\tau_u - \tau^\star = \tau_u(1 - \frac{\tau_{21}}{\tau_{31}}) \tag{7.7}$$

Hence, the final equation for the population inversion gain g_{PI} can be written as:

$$g_{PI} = \left(\frac{4\pi\alpha_0}{n}\right)^2 \frac{I_p}{\Gamma_{13}} \frac{\hbar\omega_{13}}{\Gamma_{13}} z_{13}^2 \cdot z_{32}^2 \cdot N(\tau_u - \tau^\star) \tag{7.8}$$

This set of equations shows that the gain due to population inversion is directly proportional to the pump intensity and the population difference between the lower and the upper state. It is appropriate to determine the expected threshold under the assumption that population inversion gain is the only possible gain contribution. However, as this model does not take into account gain contributions from nonlinear processes related to the presence of a strong optical field, it is insufficient for a description of all relevant gain contributions. In the following section, a summary of a more complete approach for the gain modelling including the Raman process will be given.

7.2.2 The Raman Process

For the theoretical description of the Stimulated Raman Scattering, two approaches are possible [33]: It can be describes by the nonlinear coupling between the drive and the lasing (Stokes) field, hence, as a wave interaction. From that point of view, a two-photon process is a third order process. The SRS is then described as a nonlinear coupling process between the drive and Stokes wave which is characterized by the nonlinear polarization **P**. A second possible approach is to consider the SRS as a parametric process in which the optical drive generates two waves: The Stokes wave and a material excitation wave on the E_{12} (E_{if}) transition. The coupling of these three waves is again described by the polarization **P**. In both cases, the polarization oscillations result in an additional contribution to the laser gain. If this Raman-type contribution exceeds the absorption on the signal transition an all other losses, lasing can be achieved.
In [125], the interaction of the light with an electron subsystem is modelled using the density matrix approach and Maxwell's equations. In the latter one, the intersubband polarization **P** serves as a source of field. In their treatment, they neglect many-body effects due to Coulomb interaction of electrons as well as the effect of the laser field on the electron wave functions and dipole moments of the intersubband transition. Furthermore, the realistic spatial kinetics of electron transport are replaced by rate equations for a set of electrons in order to calculate the population dynamics (diagonal elements of the density

matrix). With these approximations, the analysis is simplified: Firstly, the electron states are calculated solving the coupled Schrödinger and Poisson equation without the impact of the optical field. In a second step, the interaction of the optical fields is taken into account by solving the Maxwell 's equations coupled with the density matrix (i.e. the polarization is calculated as a trace of the density matrix). The dipole moments and electron populations herein are taken from the previous step. This treatment allows to find an expression for the gain in dependence on the intensity of the optical drive.
This procedure was applied to a three level system as shown in Figure 7.1. Under the assumption that all excitation pulses are much longer than all relaxation times and that all relevant intersubband transitions are homogeneously broadened, the following expression for the gain at the Stokes wavelength is obtained:

$$g[cm^{-1}] = Re\Bigg\{\frac{\eta}{\gamma_{32} + |\Omega_p|^2/(\gamma_{21} - i(\Delta - \delta)) + i\delta}\times \Bigg[\frac{|\Omega_p|^2(n_1 - n_3)}{(\gamma_{21} - i(\Delta - \delta))(\gamma_{31} - i\Delta)} - (n_2 - n_3)\Bigg]\Bigg\} \tag{7.9}$$

with

$$\eta = \frac{4\pi\omega_s z_{32}^2 \Gamma_s}{\hbar c n_r}$$

Herein, γ is the half width at half maximum (in frequency units), Γ_S the mode overlap with the Stokes transition at the energy ω_s, n_r the refractive index, $n_{1,2,3}$ the subband population, Δ and δ are the frequency detunings of the pump and the Raman field, respectively. The optical drive is described by its Rabi frequency Ω_p. The derivation of this formula as well as a detailed explanation of it can be found in [125] and will not be shown here. In the following, the different terms of this equation will only be briefly discussed and by this, the contributions to the total gain clarified.
First, the terms in brackets will be considered. If the optical drive is off ($\Omega_p = 0$), the gain is proportional to the Stokes field and hence, to the population inversion $n_3 - n_2$ which is given by the second term in brackets. Positive gain can only be achieved when the population inversion is present. When the drive is on ($\Omega_p \neq 0$), the polarization on the drive transition is excited by the strong field. This polarization itself and its coherent mixing with the lasing field is exciting the polarization on the E_{12} transition. The coupling between the drive field and the E_{12} polarization leads again to a contribution to the polarization on the lasing transition and therefore, to additional gain at the signal frequency. In summary, the polarization on the E_{32} transition is proportional to the intensity of the optical drive (Ω_p^2) and the population difference between E_1 and E_3. Their influence can be found in the first term in the brackets. Finally, the term before the brackets describes the saturation due to the strong drive field which is indirectly proportional to the pump intensity.
As Equation 7.9 includes Raman as well as population inversion contributions, it was used to calculate the gain in dependence on the lifetime ratio τ_{21}/τ_{32}. This ratio enters into the rate equations (Eq. 7.4 - 7.6) and therefore, determines the population of the

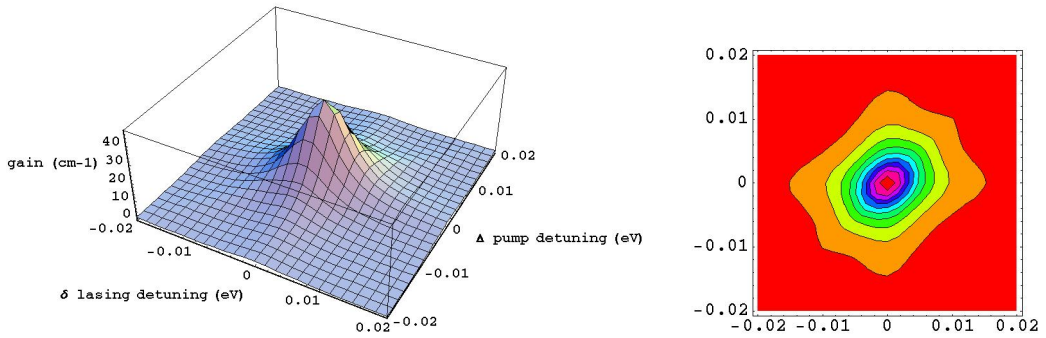

(a) $\tau_{32} \gg \tau_{21}$

(b) $\tau_{32} \gg \tau_{21}$

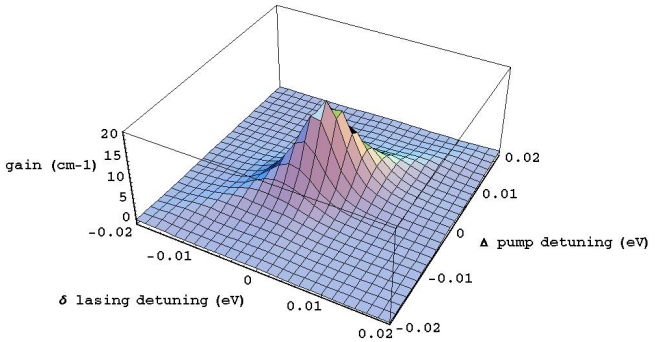

(c) $\tau_{32} > \tau_{21}$

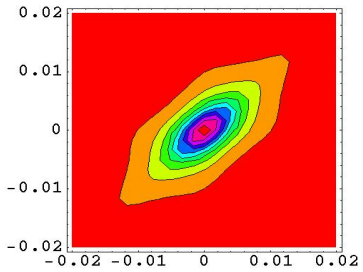

(d) $\tau_{32} > \tau_{21}$

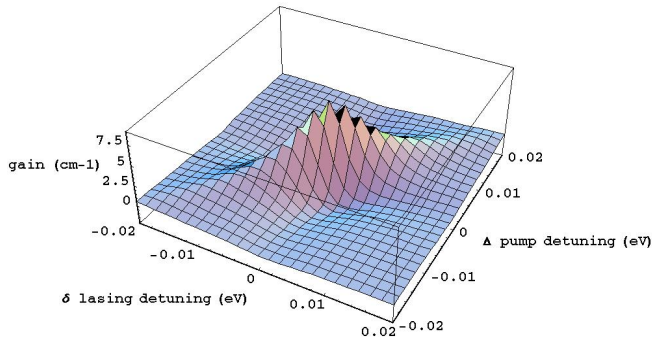

(e) $\tau_{32} = \tau_{21}$

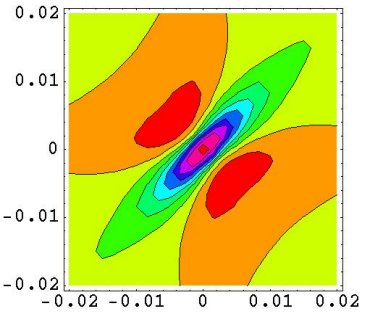

(f) $\tau_{32} = \tau_{21}$

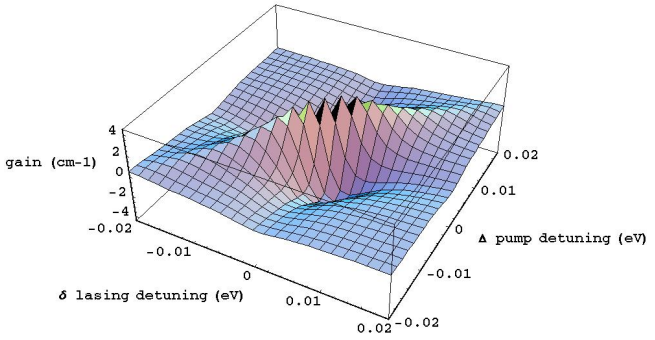

(g) $\tau_{32} < \tau_{21}$

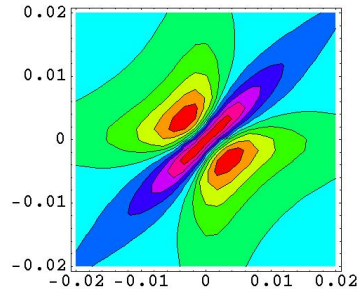

(h) $\tau_{32} < \tau_{21}$

Figure 7.2: 3D plot (left side) and contour plot (right side) of the Raman gain in dependence on the pump and signal detuning for different lifetime ratios τ_{32}/τ_{12} for Sample A. The total internal pump intensity of 250kW/cm^2 calculated from the experiment was used.

subbands. The results of this computation are shown in Figure 7.2 for four different situations: $\tau_{32} \gg \tau_{21}$, $\tau_{32} > \tau_{21}$, $\tau_{32} = \tau_{21}$ and $\tau_{32} < \tau_{21}$. A pump intensity of 250kW/cm^2 was chosen with respect to the experiments. All other parameters were taken from the first investigated III-V sample (Sample A) which is described in the next section. In the first case, $\tau_{32} \gg \tau_{21}$, the population inversion is the dominating process: The lasing energy is almost constant for all pump detunings. There is only a comparably small contribution from the Raman process which is sitting on top of the population inversion gain (Fig. 7.2a,b). The total gain achieved at $E_{pump} = E_{13}$ is about 40cm^{-1}. The situation changes for a reduced lifetime τ_{32} (Fig. 7.2c,d). The population inversion gain is decreasing as the difference in the population of the upper and lower laser state is diminished and the Raman-type contribution gains influence. This results in a higher tunability of the laser what is well visible in the contour plot on the right hand side. When $\tau_{32} = \tau_{21}$ is reached (Fig. 7.2e,f), only Raman gain is present. The total gain is decreased to 7.5cm^{-1} which is about a factor 5 lower than in presence of population inversion. Now, the laser follows the pump energy with a slope = 1 and a detuning within the entire linewidth of the pumping transition is possible. From this, one can conclude that the conditions for a vanishing population inversion are the tunability over the entire linewidth and the unity slope. In the last situation, $\tau_{32} < \tau_{21}$ (Fig. 7.2g,h), the Raman gain is decreasing and a negative g_{PI} is developing. Lasing under these conditions becomes improbable, as the remaining gain is too small to exceed common waveguide losses.
The calculations are summarized in Figure 7.3 where the maximum gain is plotted versus the lifetime ratio τ_{32}/τ_{21}. As the maximum gain is obtained for excitation at the E_{13}

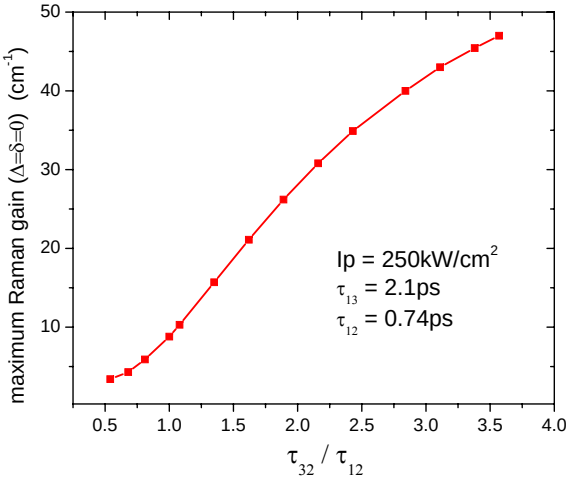

Figure 7.3: Maximum Raman gain calculated after Eq. 7.9 in dependence on the lifetime ration τ_{32}/τ_{12} for Sample A.

resonance, equation 7.9 is proportional to $\frac{z_{13}^2}{\Gamma_{13}} \times \frac{z_{32}^2}{\Gamma_{32}}$ for this special case.
With the above theory, the lasing obtained in the samples presented in the next section was analyzed and compared. The discussion of the laser characteristics with respect to the theory can be found in Section 7.3.2.

7.3 Experiment

7.3.1 Sample Characterization

Three GaInAs/AlInAs DQW structures were grown on an undoped (100) oriented InP substrate by molecular beam epitaxy. The initial sample (Sample A) was grown lattice matched while for the other ones (Sample B and C) a 0.5% strain was introduced. For this purpose, the composition of the AlInAs layer was changed to $Al_{0.532}In_{0.468}As$ and for the InGaAs layer to $In_{0.603}Ga_{0.397}As$. The waveguide structure for all samples, starting from

	Sample A	Sample B	Sample C
AlInAs	3.0nm	3.5nm	3.5nm
InGaAs	3.5nm	3.8nm	3.0nm
AlInAs	1.0nm	1.2nm	1.0nm
InGaAs	4.7nm	5.0nm	4.7nm
AlInAs	3.5nm	3.5nm	3.5nm

Table 7.1: Layer sequence for one period of the active region for the three samples. Each double quantum well was repeated 60 times forming a 1.1μm thick active region. The single periods were separated by a 3nm thick AlInAs layer, n-doped at $3 \cdot 10^{17}\text{cm}^{-3}$.

the substrate, consists of a 0.6μm GaInAs cladding layer, a 50nm AlInAs core layer, the 1.1μm active region, a 50nm AlInAs core layer and a 1.1μm GaInAs cap layer. The layer

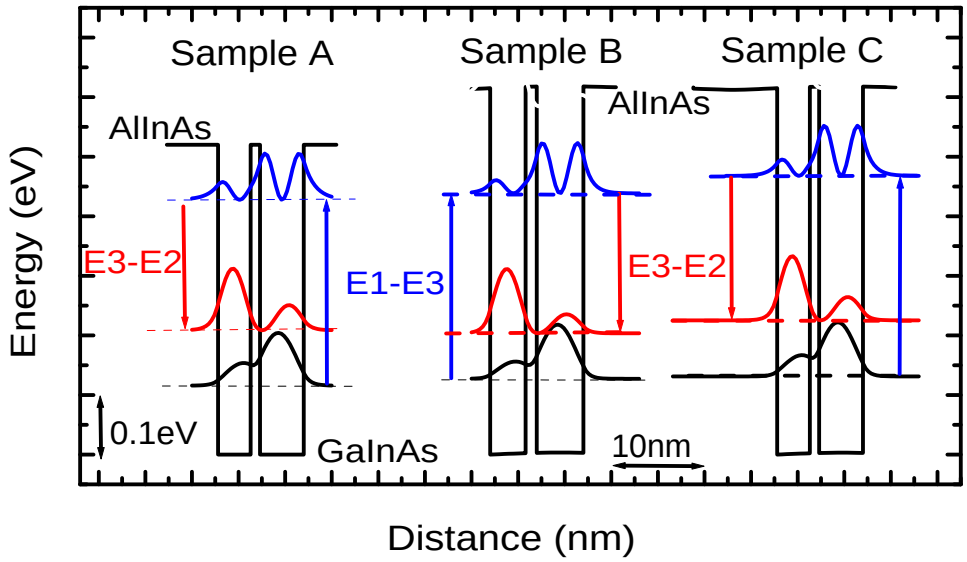

Figure 7.4: Calculated band structure for the initial lattice matched sample and the strained samples.

sequence of the different active regions is given in Table 7.1. The calculated band diagrams for all samples are shown in Figure 7.4. The higher band offsets in Sample B and C are due to the 0.5% strain introduced for these sample. By this, a better confinement of the upper states is achieved. Besides that, the three samples were designed to have a different

	Sample A	Sample B	Sample C
E_{12}	91.98meV	76.3meV	94.1meV
E_{13}	311.5meV	311.2meV	336.6meV
E_{32}	219.5meV	234.9meV	242.5meV
z_{12}	22.75Å	23.01Å	22.04Å
z_{13}	5.21Å	7.2Å	5.82Å
z_{32}	18.76Å	16.73Å	17.26Å
τ_{21}	0.74ps	0.69ps	0.75ps
τ_{31}	2.1ps	1.8ps	1.94ps
τ_{32}	2.64ps	3.29ps	2.82ps
$(\frac{1}{\tau_{32}}+\frac{1}{\tau_{31}})^{-1}$	1.17ps	1.16ps	1.15ps
$U_{th}PopInv$	14.0kW/cm^2	16.5kW/cm^2	15.5kW/cm^2

Table 7.2: Calculated parameters for the three investigated samples at 77K. The carrier concentration in the structures is $9 \cdot 10^{10}$cm^{-2}.

depopulation energy E_{12}. This should give an indication if the Raman process in our structures is due to phonon processes or associated with the subbands in the DQW and therefore a pure electronic process. The calculated energies (E_{12}, E_{13} and E_{32}), lifetimes (τ_{21}, τ_{31} and τ_{32}) and matrix elements (z_{12}, z_{13} and z_{32}) are listed in Table 7.2 for all three samples.

In order to characterize the samples and approve the calculated energies, absorption

	Sample A		Sample B		Sample C	
	70K	300K	70K	300K	70K	300K
E_{12}	95.7meV	92.1meV	-	76meV*	100.4meV	95.5meV
E_{13}	313.1meV	305meV	302meV	295meV	337.5meV	330meV
E_{32}	217.4meV*	213meV*	-	219meV	237.1meV*	234.5meV*
Γ_{12}	9.8meV	16meV	-	-	5.8meV	7.7meV
Γ_{13}	10.1meV	14meV	13meV	17meV	11meV	19.1meV
$-ln(TM/TE)$	0.22	0.12	1.5	0.9	0.78	0.44
α_{peak}	0.55cm^{-1}	0.3cm^{-1}	2.1cm^{-1}	1.3cm^{-1}	1.3cm^{-1}	0.7cm^{-1}

Table 7.3: Transition energies, linewidth and peak absorption obtained from the spectra shown in Figure 7.5. The values marked by * are calculated from the measured values as they could not be measured directly.

measurements were performed using the setup described in Chapter **??**. For this purpose, the samples were cleaved into 4mm, 7mm and 6mm (Sample A, B and C) long samples with two parallel 45° facets and a thickness of $\sim 250\mu$m. The obtained spectra are shown in Figure 7.5 for 70K and 300K. From these data, the peak absorption α_{peak} can be deduced which is given by:

$$-ln(TM/TE) = \alpha_{peak} \cdot L_s$$

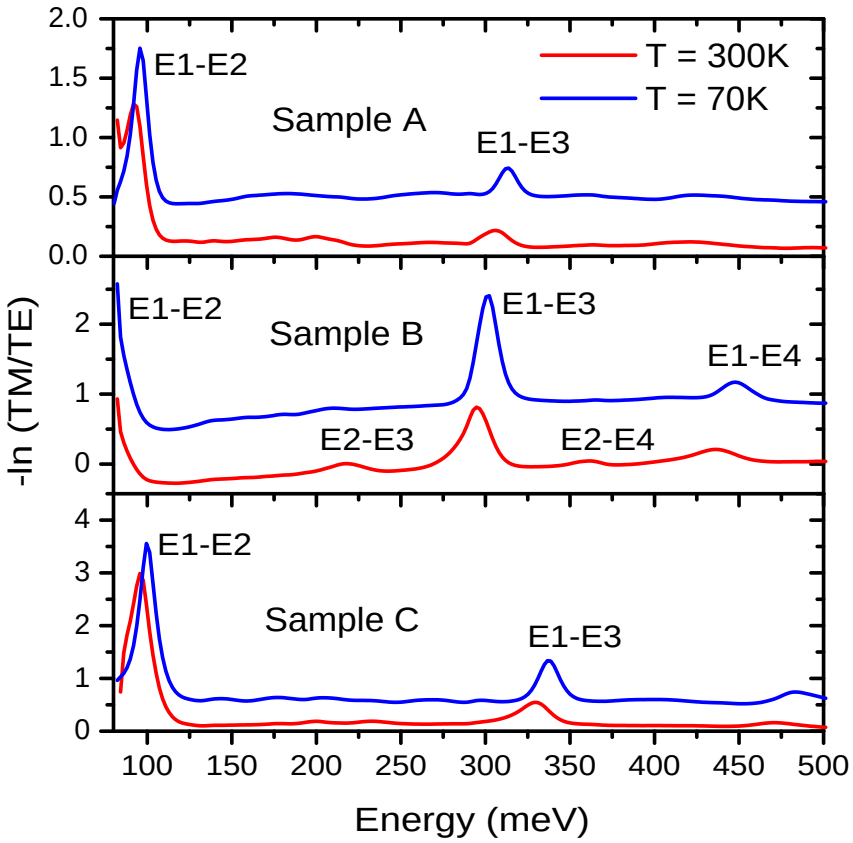

Figure 7.5: Waveguide absorption measurements for the three samples at different temperatures. The E_{12} transition of Sample B could not be measured as it is below the cutoff of the MCT detector. However, at 300K, it can be calculated from the difference of the measured E_{13} and E_{23} transition.

where L_s is the sample length and $-ln(TM/TE)$ is obtained from the measurement. The resulting peak absorption as well as energies and linewidths determined by fitting are shown in Table 7.3. Using these values, the population inversion threshold was calculated by equating the predicted gain (see equation 7.8) with the expected losses. For the loss, one has to consider the free carrier absorption which was calculated for the employed waveguide structure to $\alpha_{fc} = 1.7\text{cm}^{-1}$ using the Drude model. Furthermore, the reflection losses at the facets have to be taken into account which are given by:

$$\frac{1}{2L_s} ln \frac{1}{R_{m1} \cdot R_{m2}}$$

with the reflectance of the both facets $R_{m1} = R_{m2} = 0.3$. Adding these two components, the total loss of each structure can be determined. Equating this to the expected gain (Eq. 7.8), the population inversion threshold values calculated for the three structures are 16kW/cm^2, 14.3kW/cm^2 and 14.4kW/cm^2 for Sample A, B and C, respectively.

7.3.2 Laser Characteristics

Details of the setup used for the optical pumping and the sample geometry are given in chapter 5. The samples were measured in a Helium cooled cryostat at a temperature of 70K, unless otherwise stated. For excitation near the peak absorption energy ($E_{pump} = E_{13}$), lasing was found for all samples. A characteristic spectrum for Sample A is shown in Figure 7.6a. The lasing wavelength was found to be $\sim$ 217meV ($= 5.71\mu$m) with a linewidth of about 1meV. The values for Sample B are $\sim$ 220meV ($= 5.59\mu$m) for an excitation at 302meV and for Sample C $\sim$ 233meV ($= 5.32\mu$m) at an excitation of 333meV. Comparing these values with the data obtained from the absorption measurements (see Table 7.3), a good agreement between the lasing energy and the E_{32} transition can be found. For an estimation of the total internal conversion efficiency, the total integrated lasing output and its spatial distribution was measured for Sample A. From this, an output pulse power from a single facet of up to 2nJ was obtained. In order to find the internal value, the losses from the windows of the cryostat and the focussing lenses need to be considered giving a factor of 0.95 and 0.8, respectively. Furthermore, the same

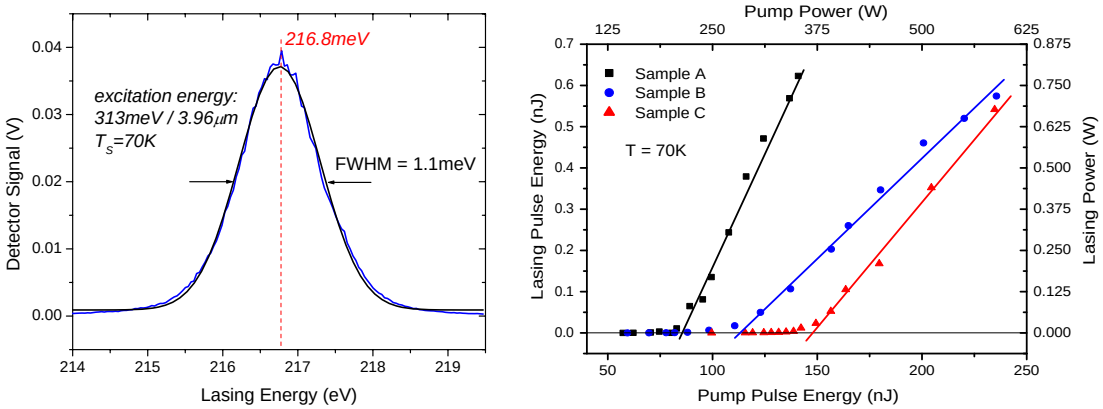

(a) (b)

Figure 7.6: (a)Spectrum of Sample A at resonance energy and a temperature of 70K. The excitation energy was 313meV corresponding to a wavelength of 3.96μm. (b) Lasing threshold for all samples at $T = 70$K. The threshold characteristics are taken at resonance excitation $\hbar\omega_p = E_{13}$.

output is expected from the second facet (factor 0.5) which leads to a total loss factor of 0.38 and hence, to a total output pulse power of 5.3nJ ($\sim$ 14W). Besides this, the losses on the incoupling side have to be taken into account: As the pump beam is at least travelling twice through the cavity, the reflection at the facets (factor $r = 0.3$) as well as the absorption along the cavity needs to be considered. The reflection loss is then calculated by $R = 1 - \left(\frac{1-r}{1+r}\right)^2$ giving a factor of 0.7. The absorption strength is given by $1 - Exp(-2\alpha_{peak} \cdot L_s) = 0.36$ where α_{peak} is the peak absorption at the pumping energy obtained from the absorption measurement (see Table 7.3). The pump pulse power as determined in chapter 5 was $\sim 1.7\mu$J. Correcting this with the incoupling loss factor of 0.25 gives an internal pump pulse energy of 0.42μJ. The resulting internal conversion

efficiency is therefore 1.3%. The highest operation temperature is found to be $\sim$ 190K for Sample A and C and $\sim$ 120K for Sample B.
The threshold characteristics are shown in Figure 7.6. All samples show a linear increase of the lasing pulse energy with the pump energy above threshold. A saturation effect was not detected for any of those samples. For Sample A, the internal threshold pump pulse energy is found to be 86nJ which corresponds to an internal power of 208W for a pulse length of 0.4ns. The threshold intensity is obtained using the lasing area defined by the length of the lasing cavity (L_s = 0.5cm) and the spot size of the pump laser (100μm). The latter one was determined in a separate experiment using a pinhole. This leads to a threshold intensity of 52kW/cm^2. For Sample B (Sample C), the values are in analogy 113nJ (148nJ), 283W (370W) and 57kW/cm^2 (67kW/cm^2) with a sample length of L_s = 0.5cm (L_s = 0.55cm). Comparing the measured threshold values of the different samples to the calculated ones (see Table 7.3), Sample A and B show a reasonable agreement. For Sample C the threshold was expected to be lower than for Sample B which was not confirmed by the measurement. Possible reasons for this behavior may be found in less perfect facets and/or particles on the sample surface as well as measurements

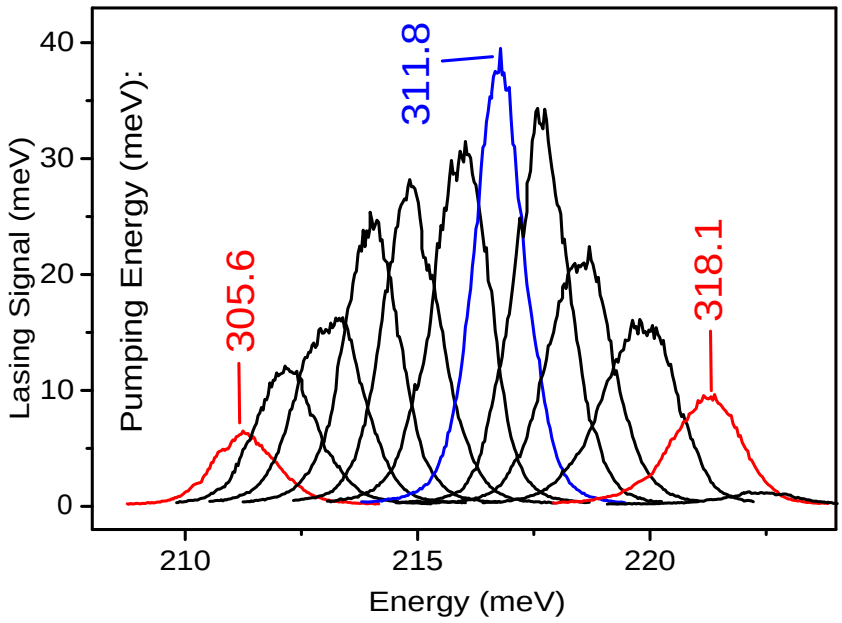

Figure 7.7: Spectra over the whole tuning range for Sample A.

uncertainty. The factor $3-4$ higher threshold obtained in the measurements is within tolerance. It originates either from upper state lifetimes shorter than calculated or losses which are higher than in the estimation used above.
For further investigation, the pump laser energy was detuned from resonance and the dependence of the lasing wavelength on the excitation energy was studied. The spectra taken over the entire tuning range are shown in Figure 7.7 for Sample A. The maximum detuning from resonance is about 7meV towards lower and higher energies. The peak energies of the lasing spectra versus the pumping energy are plotted in Figure 7.8. For all samples, the shift with the pump energy can be approximated by a linear dependence

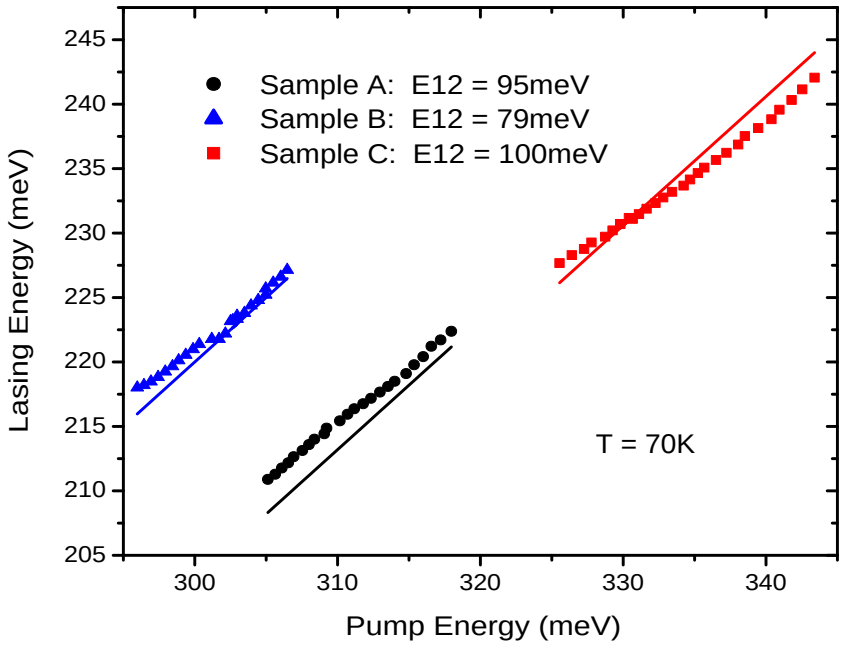

Figure 7.8: Peak positions of the emission spectra versus pumping energy. The solid lines are the shifts expected from the absorption measurements for $E_{32} = E_{13} - E_{12}$. The different tuning ranges of the three samples are mainly due to the pump laser characteristics which shows a significant increase of power above 300meV.

with unity slope which proves the Raman process. The offset between pump and laser energy is around the corresponding depopulation energies E_{12} for each sample as indicated by the solid line in Figure 7.8. This result is an indication that in these samples the Raman process is of pure electronic nature as the depopulation energy is tuned off-resonant to LO-phonon energies. However, the double phonon resonances for the LO phonons of AlAs (47meV), GaAs (36meV), InAs (30meV) and the triple phonon resonance of InP (43meV) are quite close to the designed E_{12} transitions. Hence, a final proof of the pure electronic nature of the Raman gain would require further samples with a smaller grading of the E_{12} transition. However, for excitation below resonance the slope diverges from the unity value for all samples. There are two approaches of explanation. The first one is based on an experimental observation: As the deviation for Sample B and C which were grown with a 0.5% strain is larger than for Samples A, the nonlinearity can be assigned to inhomogeneities within the sample structure. On the other hand, the fact that this behavior is also present for Sample A which shows a very good agreement to the theory for all other measurements, gives rise to the assumption that this nonlinearity originates from a physical process within the structure. Possible mechanism which induce a nonlinearity are a high carrier temperature and with it the distribution in k-space. Hence, the nonparabolicity of the subbands has to be taken into account which causes a shift in the transition energies and therefore, a deviation from the values calculated at $k = 0$ or measured at low intensities.

From the measurements shown above, we can state that the gain mechanism present in

these structures is an electronic Raman process. From the lifetime values listed in Table 7.2 however, one can calculate that the ratio τ_{32}/τ_{21} is about 3.5 for Sample A, which suggests strong population inversion. Hence, population inversion gain should be the dominating process and the emission wavelength should be fixed to E_{32}. Another important feature is reported in Figure 7.9, where the absorption peak of the E_{13} transition is plotted versus the tuning range of the laser. The center of the tuning curve is in reason-

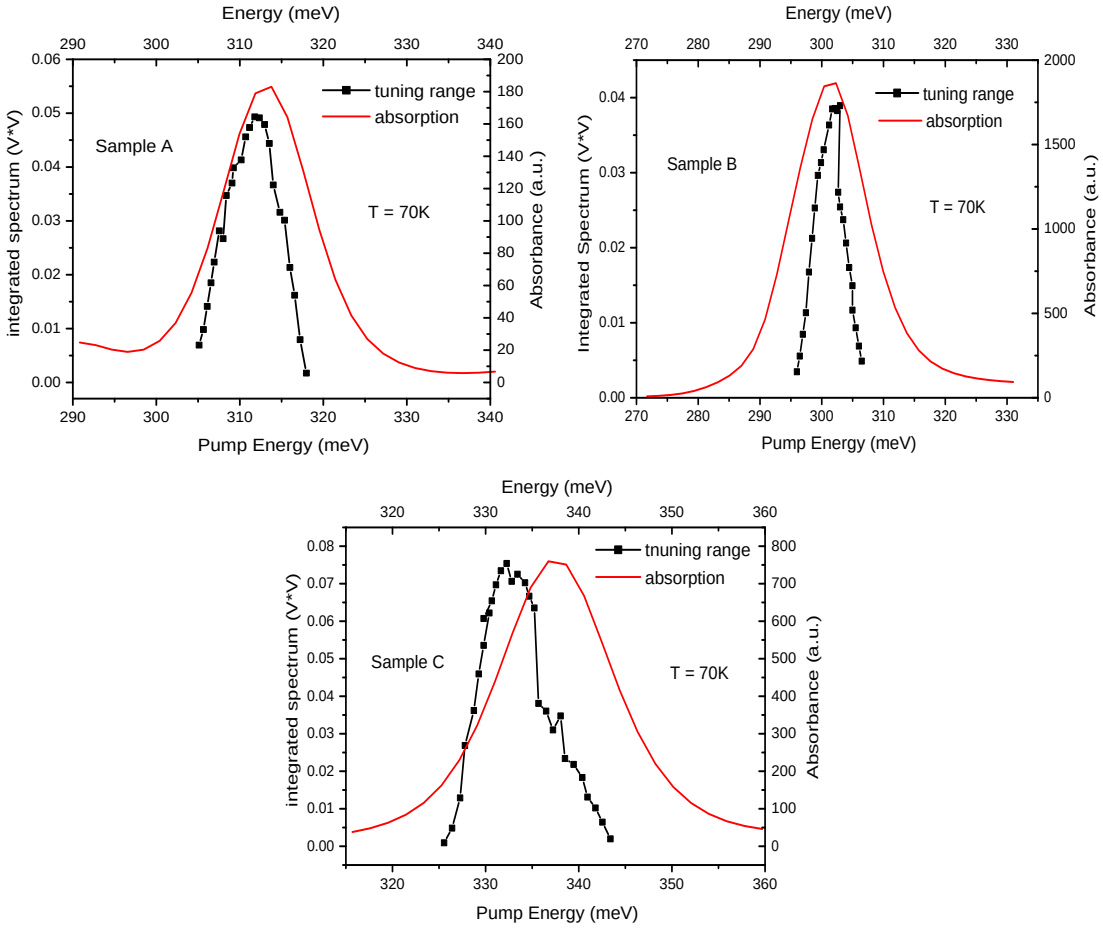

Figure 7.9: Absorption measurement versus integrated spectra over the whole tuning range plotted for Sample A, B and C.

able agreement with the peak of the absorption for Sample A and B. The tuning curve is shifted about 5meV for Sample B. From the calculations performed in Section 7.2.2, it was stated that tuning range indicates the amount of Raman gain with respect to the population inversion. Together with the unity slope found in the plot E_{pump} versus E_laser, the tunability over E_{13} linewidth suggests a vanishing population inversion in these samples. This corresponds to the situation $\tau_{32} \approx \tau_{21}$ as shown in Figure 7.2e,f. This result can only be understood if the electron dynamics are taken into account: Electrons which leave the third subband at $k = 0$ will scatter to the first (or second) subband with a high kinetic energy and therefore, they will be distributed in k-space. Calculating the intersubband lifetime at such large inplane momentum for example for Sample A gives a lifetime $\tau_{21} = 1.6ps$ instead of $\tau_{21} = 0.7ps$ at $k = 0$, the first contribution for a re-

duced population inversion. For a further understanding of the dynamics present in these structures, time resolved pump-probe spectroscopy was employed.

7.3.3 Time resolved pump-probe spectroscopy

The measurements were carried out at the physical-chemical institute of the University of Zürich. The samples were thinned down to $\sim 200\mu$m and mounted into a helium cooled cryostat. The incident laser was at Brewster angle which allowed to work in a single pass configuration. The measurements were performed at a temperature of 70K. For the excitation generation, the laser beam obtained from a Ti:sapphire regenerative amplifier operating at 1kHz at a wavelength of $\sim$ 800nm was downconverted: First, in a KTP, parametric oscillations of a signal and idler were generated by the $\sim$ 800nm beam. In a second step, the difference frequency of these pulses was generated in a $AgGaS_2$ crystal. By this, $\sim$ 150fs long pulses with a pulse power of about 3μJ were obtained. For detection of the probe signal, the pulses were dispersed in a grating spectrometer and detected by a LN2-cooled 64-channel MCT detector (see Figure 7.10). In Figure 7.11 the

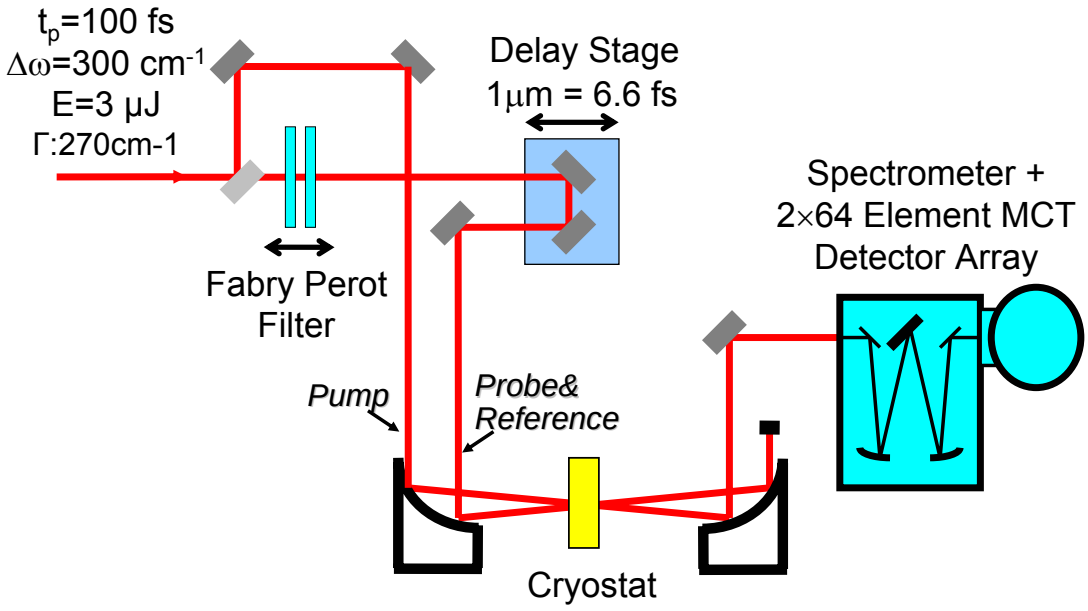

Figure 7.10: Schematic drawing of the pump-probe-setup at the Physical-Chemical Institute at the University of Zürich. The picture was provided by V.Botan.

obtained spectra for Sample A and B at increasing delay times between pump and probe signal are shown. For short delay times ($\tau_{delay} = 200fs - 400fs$), the linear absorption is reproduced well by the time resolved spectrum. The latter one thereby consists of the absorption signal (here the bleach) and a stimulated emission component. For times up to 1000fs, the low energy tail of the signal recovers while the peak only decreases slightly. At later times, the peak signal starts to disappear until the thermal equilibrium of the ground state is reached [126]. The final cooling to the lattice temperature of 70K is reached for times longer than 10ps. These different processes can be well distinguished

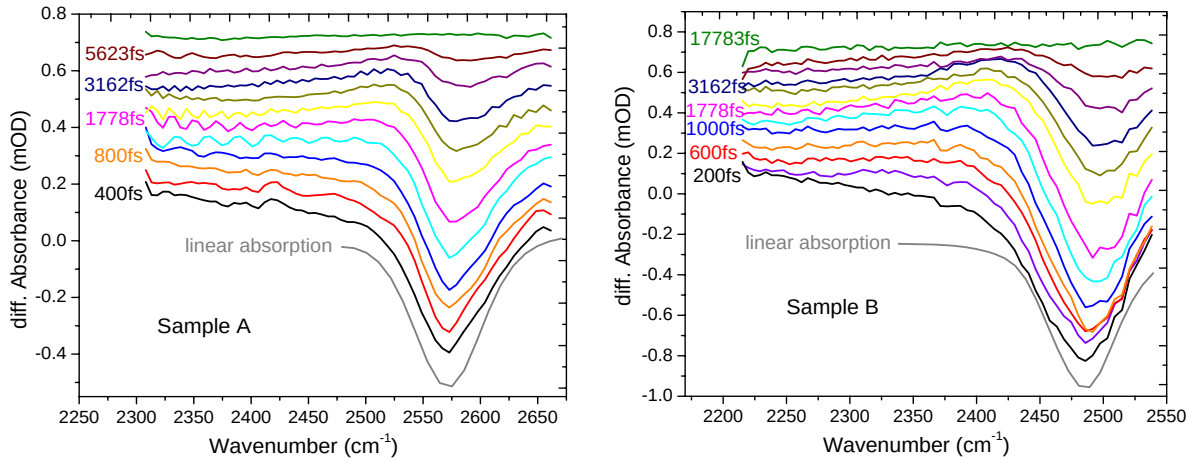

Figure 7.11: Time resolved pump-probe difference spectra of the pumping transition E_{13} for Sample A (a) and Sample B (b) at different delay times. Every spectra is shifted by +0.06 for clarity. The black curve is the linear absorption, shown as comparison.

when the integral of the spectra is analyzed. The integrated spectra for all three samples are shown in Figure 7.12(a). The slight decrease in the beginning, the fast decay as well as the almost constant integral during carrier cooling can be identified. The relaxation time to the ground state in thermal equilibrium is obtained from an exponential fit of the data points. These times are $\sim$ 1.1ps for Sample A and C and about 1.3ps for Sample B. The slightly higher relaxation time for the latter one may be due to the better confinement of the state (as there is a fourth level above the upper state E_3 which is not the case for Sample A and C) and therefore, the reduced carrier escape to the continuum. Comparing the times obtained from the fit of the measurement to the calculated ratio $(\frac{1}{\tau_{32}} + \frac{1}{\tau_{31}})^{-1}$ in Table 7.3, a good agreement is found. However, it has to be noted, that these times include two processes and consequently, the lifetime of the upper state is shorter than 1.1ps or 1.3ps, respectively. These processes are the relaxation from subband 3 to the first (or second) one as well as the intraband scattering by phonon emission and Auger-type electron-electron scattering in the lower state from higher k-states towards $k = 0$ and hence, thermal equilibrium. Due to the relatively high carrier density of $0.9 * 10^{11}\mathrm{cm}^{-1}$ in these structures, electron-electron interaction is possible and the Auger process needs to be considered [127]. During this scattering process carriers remaining in the ground state are excited out of the cold Fermi sea to higher k which results in a decrease of the signal at short times. As in these measurements difference spectra of $t(\infty) - t(x)$ are taken, this leads to an increase of the bleach. At the same time, carriers from the third subband scatter into the lower subbands at an inplane momentum $-k$ as requested by the momentum conservation. By this, the stimulated emission from the upper level is decreased which partly reduces the increase of the bleach. This behavior is more pronounced for lower intensities (see Figure 7.12b) as at high intensities saturation effects prevent this observation. Further analysis of the spectra at short delay times and additional two color pump-probe experiments could allow to distinguish between phonon and Auger-type scattering.

The comparison in Figure 7.12b for the different intensities clearly shows the decrease of

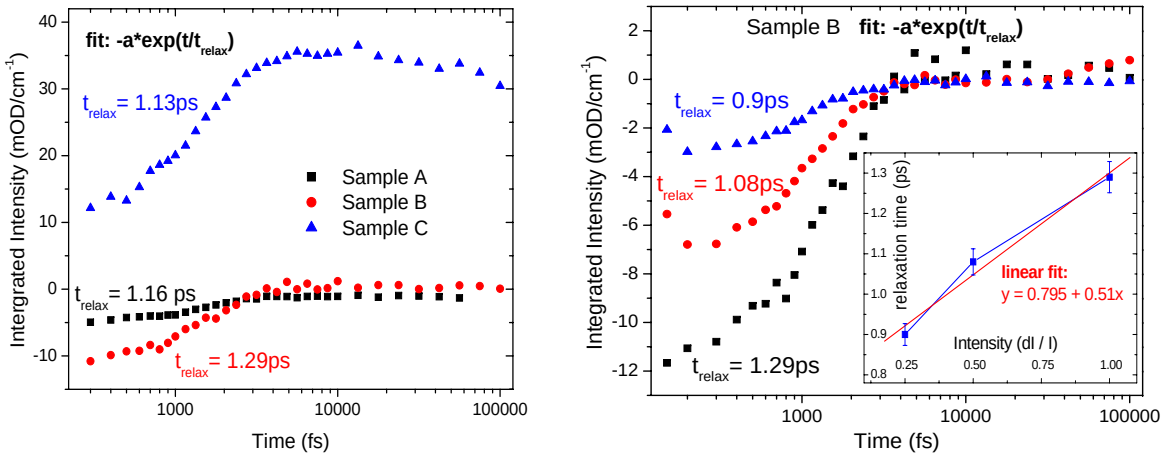

Figure 7.12: Time dependence of the integrated intensity on a log-lin scale for all three samples at full pump intensity (a) and the integral of the spectra for Sample B taken at full ($I = 1$, black curve), middle ($I = \frac{1}{2}$, red curve) and low ($I = \frac{1}{4}$, blue curve) intensity (b). The relaxation times from subband 3 to subband 1 obtained from the fit are indicated for each curve.

relaxation times for lower intensities. At full intensity, a lifetime of $\sim$ 1.3ps was obtained which reduces to 1.08ps at half intensity and to 0.9ps at $\frac{1}{4}$ intensity. This result confirms the scattering picture: carriers excited with lower intensity obtain a smaller kinetic energy and hence, scatter to smaller k vectors than at higher intensities which reduces the distribution in k-space. As a consequence, the time for the intraband scattering needed to reach the thermal equilibrium is shorter which is reducing the total relaxation time. As a preliminary result, the upper state lifetime was deduced using a simple linear fitting procedure (see inset of Figure 7.12b). Using the assumption that at zero intensity all carriers remain at $k = 0$ and no distribution to higher k values takes place, an upper state lifetime of $\sim$ 0.8ps can be found. However, this very simple picture needs to be confirmed with additional data for more intensity points and different samples.
These measurements suggest, that the upper state lifetimes in our structures are shorter than expected from the calculations, which is mainly due to the high kinetic energy of the carriers. To finally compare the obtained results with the calculations, the extraction of the lifetime τ_{32} from the measurements would be important. For this investigation, two color pump-probe experiments need to be employed. For a better practical understanding of the interaction between population inversion and Raman gain and the influence of the lower state lifetime, a superlattice structure using a b2c design will be investigated. In that kind of structures, the depopulation of the lower state is provided via a miniband using optical phonons. As this process is very fast, it should be possible to achieve population inversion and compare to the contributions of the Raman gain.

Conclusion on the III-V Raman Laser

In this chapter, the investigated III-V samples were presented. For all samples, lasing was found which confirmed the functionality of the setup and the suitability of the approach. Furthermore, the gain process in these structures was found to be Raman-type: For a detuned pump energy, the lasing energy followed the pump with a constant offset which is about the energy of the E_{12} transition. This leads to an almost unity slope in the lasing versus pump energy plot. From the calculations performed for this kind of system it was found that these features indicate a vanishing population inversion and dominating Raman gain. This is only obtained for lifetimes $\tau_{32} = \tau_{21}$. To investigate the upper state lifetime in these structures, time-resolved measurements were performed. By this, a reduced upper state lifetime was found. Together with the expected increased lower state lifetime at higher in-plane momentum k, possible reasons for the missing population inversion were found.
Finally, it has to be mentioned, that the Raman process is a promising way in order to achieve in SiGe QC structures as population inversion is not required. This is an important advantage regarding the low lifetimes in SiGe structures. From Equation 7.9, one can derive the basic rules for a suitable SiGe design: narrow linewidths, strong matrix elements z_{13} and z_{32} and a low loss waveguide. The work carried out regarding to this goal is the topic of the next chapter (Chapter 8).

Chapter 8

SiGe Structures for Optical Pumping

The basic requirement for an optically pumped intersubband laser can be satisfied by an adequate three level design. Further requirements are strong optical matrix elements, small linewidth broadening and a low reabsorption loss. For the III-V material, Double Quantum Well (DQW) structures were employed to match this condition. The laser wavelength is set in the range of 5μm where the free carrier absorption is comparably low which is of importance in particular for the SiGe system. For the pumping wavelength, values between 3μm and 4μm were chosen to match the excitations available from the setup (see chapter 5). To realize such a system in the SiGe material system, one could make use of the complexity of the valence band structure. In Figure 3.6 in Chapter 3, it was shown that already in a single SiGe quantum well more than three well confined levels are formed due to the splitting into HH, LH and SO bands. It was found by calculation that the alternate use of these levels for the single QW with adequate thickness would allow to obtain the transitions at the required wavelengths. However, calculations have also shown, that this simple kind of design is not suitable as reabsorption processes from the ground state are present. The way to avoid this reabsorption is to work with an asymmetric design which suppresses these processes. In this work, two designs were chosen (see also [128]): A DQW structure similar to the III-V design and a Step Quantum Well (StepQW). For the StepQW, a pure germanium layer was introduced on one side of a 50% SiGe quantum well in order to obtain asymmetry. In the following, these two designs will be theoretically analyzed and compared with respect to their optical properties and expected gain (Section 8.1). In the subsequent sections, the experimental investigations for the DQW (Section 8.2.2) and the StepQW (Section 8.2.3) are discussed.

8.1 Theoretical Framework

In the theoretical discussion, both samples will be first investigated as single period samples. In a second step, the effects of additional periods will be shown. For the StepQW, the influence of the pure Ge and the SiGe thickness on the oscillator strength is studied. Finally, a comparison between the two structures regarding the expected gain will be carried out.

For the calculations, a 6-band $\mathbf{k} \cdot \mathbf{p}$ model was used as described in chapter 3.3. This simulation tool was developed by Soichiro Tsujino and Mathilde Rüfenacht within the frame of this project. For the absorption and emission spectra, the strength of the transition is expressed as differential cross section σ_{ij}. From this, the absorption coefficient α_{ij} between the states i and j can be determined from:

$$\alpha_{ij} = \frac{\sigma_{ij} N_S}{L_P}$$

where the L_P is the thickness of one period and N_S the sheet carrier density. The gain was calculated using the expressions presented in the previous Chapter.
The calculations were carried out at an in-plane wave vector $k = 0.18\text{nm}^{-1}$. For a complete analysis, summation over all k states would be necessary. By this, the dispersion is taken into account accurately which influences oscillator strength and transition energies. For a reduction of the complexity, calculations were carried out a k value which refers approximately to an average value and is expected from the doping. To take into account the in-plane anisotropy expressed by the argument of the k vector, the average value over the whole in-plane area should be used. Due to the symmetry of the crystal structure by 90° rotation, this can be approximated by using the average values for the differential cross section of arguments between 0° and 90°. This symmetry also includes that the x- and y-polarization contribute equally to the absorption. In the following, the x- and y-polarized absorption is summarized as in-plane contribution in the calculated absorption and emission spectra.

8.1.1 Double Quantum Well

The design of the DQW is shown in Figure 8.1 for one period. In order to match the required wavelengths, the layer sequence was designed as follows: A 26Å thick $Si_{0.2}Ge_{0.8}$ well doped at $1 \cdot 10^{18}\text{cm}^{-3}$, a 4Å Si barrier and a 18Å thick $Si_{0.2}Ge_{0.8}$ well. This DQW was embedded into 11Å thick Si barriers. The structure was designed for an average Germanium concentration of 50% and hence, for the growth on $Si_{0.5}Ge_{0.5}$ relaxed buffer. The calculated band diagram and wave functions are shown in Figure 8.1a. As lasing states, only HH levels are employed. The pumping transition E_{13} between HH1 and HH3 is designed at an energy of 308meV ($\sim 4\mu$m). The lasing energy E_{32} is designed to 240meV ($\sim 5.2\mu$m) involving the transition between HH3 and HH2. The calculated absorption and emission spectra for all polarizations[1] can be found in Figure 8.1b[2]. As the employed transitions are mainly z-polarized, a TM mode excitation is required for this structure.
From this calculation, some advantages and problems of this design can already be pointed out. In the DQW, the two quantum wells are coupled via a thin barrier (see Figure 8.1).

[1]The z-polarization is defined parallel to the growth direction and therefore, perpendicular to the layers. The x- and y-polarization are the inplane components.

[2]The absorption is calculated under the assumption that carriers occupy the ground state (HH1) only. For the calculation of the emission spectrum it is assumed that carriers occupy the upper laser state (HH3 or LH2) only.

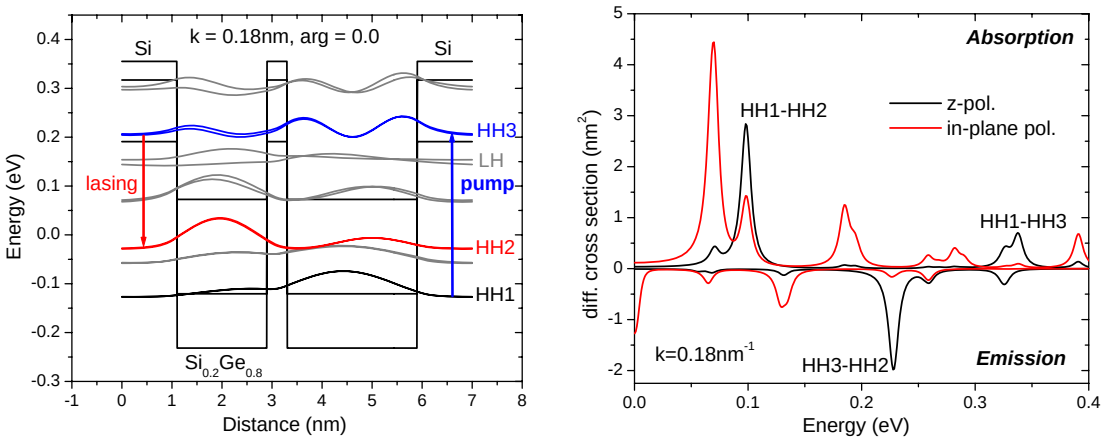

(a) (b)

Figure 8.1: (a) Band diagram and wave functions for the DQW structure. The HH states forming the laser levels are marked as follows: HH1 serves as laser ground state (black line), HH2 as lower laser state (red line) and HH3 as upper laser state (blue line). The interspersed LH states are plotted as gray lines. (b) Calculated absorption and emission spectrum of the DQW structure for all polarizations. According to the doping, an in-plane wave vector of $k = 0.18\text{nm}^{-1}$ was assumed.

This allows a strong coupling of the states formed in each well and therefore, gives a high oscillator strength between the levels. The problem of reabsorption is avoided by the diagonal transition for the depopulation. From this, high intersubband gain can be expected. Furthermore, the DQWs with a maximum germanium content of 80% in the SiGe wells were grown on 50% SiGe buffer which is a well controlled growth process. However, this structure also shows some disadvantages: First of all, the only 4Å thick Si barrier is at the border of the precision of state of the art silicon MBE growth (see Chapter 4). Therefore, the accurate growth of this structure is questionable as even small derivations of the required fluxes during growth can strongly influence the optical properties. Beyond this, these structures should be sensitive to interface roughness as very thin layers and several interfaces are involved. As interface roughness results in broader transition linewidths, the intersubband gain in the structure can be reduced. Another problem arises from the interspersed LH states (gray lines) which are located between the HH laser states (colored lines), see Fig. 8.1. These intermediate levels give rise to non-radiative transitions resulting in a reduction of the upper laser state lifetime which diminishes the gain. However, these possible problems are difficult to implement in the calculations and can therefore not be quantified here.

Another point of discussion arises when the coupling between several periods is considered. As an example, a structure composed of 3 periods (see Figure 8.2a) was investigated. The calculated emission spectrum in Figure 8.2b shows that for an increasing number of periods the lasing transition is broadened due to miniband formation. Although the integrated cross section for this transition increases as expected of a factor of three, the peak differential cross section of this transition only slightly increases due to the broadening of the transition. Reason for this is the thickness of the Si barriers which needs to be

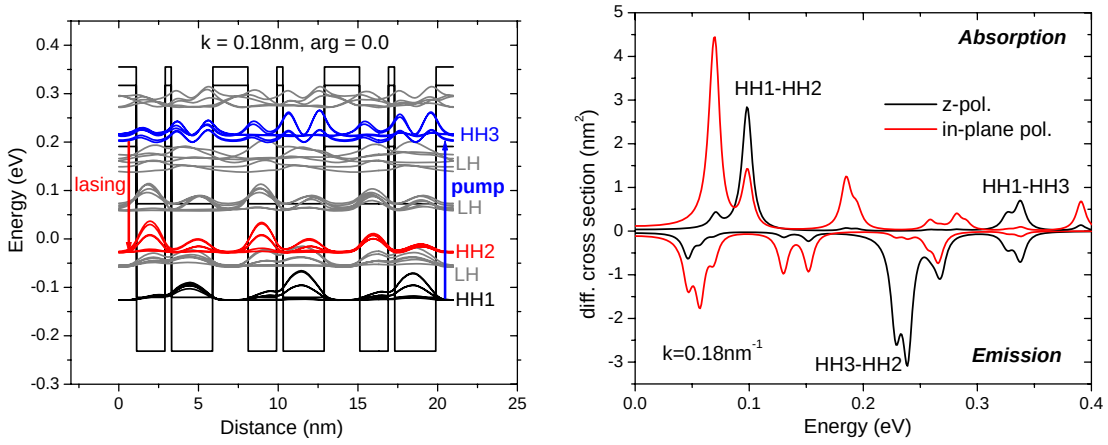

(a) (b)

Figure 8.2: (a) Band diagram and wave functions for the DQW structure with 3 periods. The laser levels are marked as in Figure 8.1. (b) Calculated absorption and emission spectrum for all polarizations.

adjusted with respect to strain compensation. In our case, 11Å barriers are required to obtain a total Ge concentration of 50%. For the decoupling of the neighboring periods, barrier thicknesses in the range of 20Å to 30Å would be necessary. At that point, this design is limited by the SiGe material system. A possible way to circumvent this problem, could be found in the growth on relaxed buffers with a lower germanium content. Within this work however, the structure presented above was exclusively grown on relaxed buffer with 50% Germanium. The results on this approach can be found in section 8.2.2.

8.1.2 Step Quantum Well

The second approach for the realization of a three level system in SiGe was a StepQW design as shown in Figure 8.3. The asymmetry was achieved by introducing a pure Ge spike on one side of a $Si_{0.5}Ge_{0.5}$ QW. In order to obtain the desired pump and lasing wavelength, this structure was grown on $Si_{0.75}Ge_{0.25}$ substrate which provides the necessary higher band offsets between barrier and well. The initial design consists of a 12Å pure Ge well and a 36Å $Si_{0.5}Ge_{0.5}$ well embedded into 36Å Si barriers. The band structure is shown in Figure 8.3a. As pumping transition the HH1-LH2 transition is employed. From the calculated absorption spectra (Figure 8.3b) it is found that this transition has mainly in-plane components as it is also expected from the selection rules (see chapter 3.3). This requires pumping using a TE polarized excitation. The designed lasing transition is LH2-LH1 which is mainly z-polarized (TM).
From the band diagram, one can find some advantages of this design: With respect to the population inversion gain the following points can be found:

- There is only one intermediate level (HH2) between the laser states which reduces the loss of carriers due to non radiative transitions and with it the upper state lifetime.

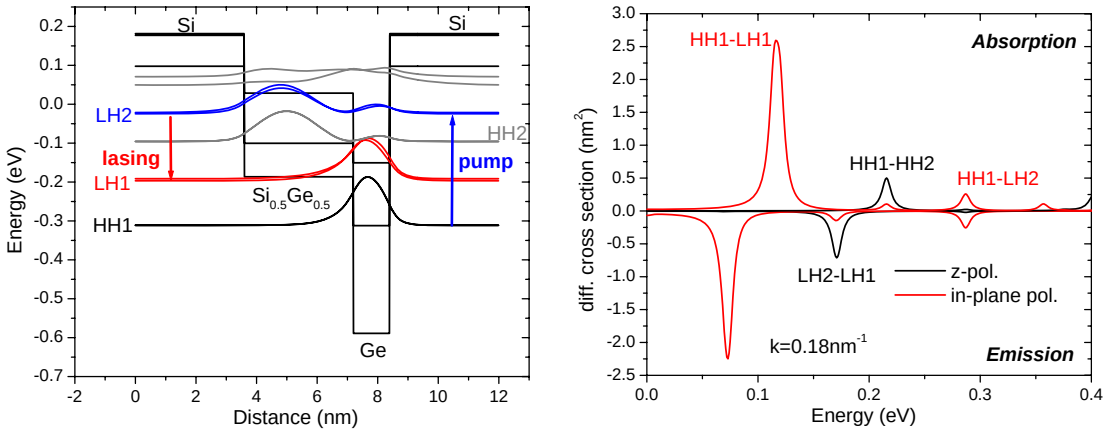

(a) (b)

Figure 8.3: (a) Band diagram and wave functions for the StepQW structure. The TE pumping transition and the TM lasing transition are indicated. The involved laser states are marked as follows: HH1 serves as laser ground state (black line), LH1 as lower laser state (red line) and LH2 as upper laser state (blue line). The interspersed state (gray line) corresponds to the HH2 state.(b) Calculated absorption and emission spectrum of the StepQW structure for all polarizations. According to the doping, a k vector of 0.18nm^{-1} was assumed.

- The reabsorption from HH1 to HH2 is well detuned from the lasing wavelength (see also Figure 8.3b). As this transition is mainly z-polarized, the absorption for TE excitation is improbable but can not be excluded for higher in-plane momentum.

The advantageous feature for the Raman gain is:

- Asymmetric StepQW structures provide advantages of large optical nonlinearities as stated for n-type systems in [129]. As nonlinear processes are the basis of the Raman gain, this structure is favoring a Raman-type gain contribution.

Because this structure is rather simple, it has the advantage of a robust design: Thickness variations of the Germanium well thickness mostly have influence on the lowest state (HH1) and may therefore slightly change the pump energy but does not have a big impact on the lasing energy and the oscillator strength between the states. On the other hand, the thickness of the $Si_{0.5}Ge_{0.5}$ well has strong influence on the lasing energy as shown in Section 8.1.2. This includes the possibility of an independent tuning of excitation and lasing energy.

However, also for this structure, drawbacks have to be taken into account: On the one hand, the samples have to be grown on 25% Ge relaxed buffers. As the growth conditions on these buffers appeared to be less established than for the 50% buffer, optimization of the structure in terms of growth condition, resulting transition energies and their coupling strength is necessary. On the other hand, the growth of pure Ge on Si (or the other way around) is challenging. Germanium grown on pure silicon has strong tendency to form islands when a certain thickness is exceeded. Deposition at high temperatures

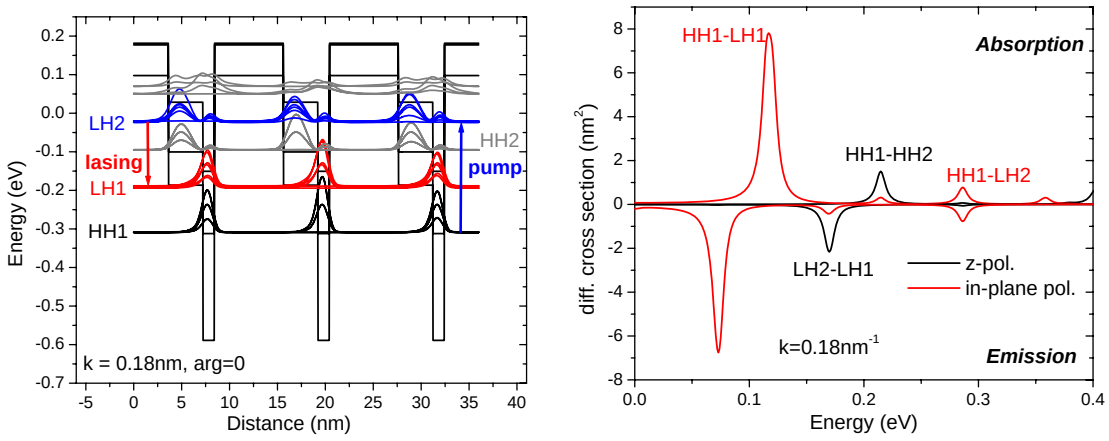

(a) (b)

Figure 8.4: (a) Band diagram and wave functions for the 3 period StepQW structure. The laser levels are marked as in Figure 8.3. (b) Calculated absorption and emission spectrum for all polarizations.

is supporting this process and the window for a well controlled growth may be rather narrow. The main experiments are summarized in Section 8.2.3.
The fact that the structures were designed for 25% buffer allows to use thicker Si barriers than for the DQW as the average germanium content is decreased. This turns out to be advantageous for the decoupling of multiple periods. The band diagram of a 3 period structure as well as the calculated absorption and emission spectra are shown in Figure 8.4. We find, that the peak emission is increased by a factor of three compared to the single period sample as expected for decoupled QC structures. Due to the better confinement of the states, the splitting of higher order levels is smaller preventing additional linewidth broadening for the multi period structures as observed in the DQW. In that respect, this kind of design is less restricted by the material limitations (barrier thickness for decoupling) and can be adjusted for high performance.
However, regarding to this discussion, it has to be mentioned that the band structure for asymmetric SiGe QWs is rather complicated. The dispersion in the valence band may lead to additional coupling effects (i.e anticrossing between states). Above this, including the splitting of states, the determination of the total matrix element for one transition is not as straight forward as for n-type III-V structures. This implies that a direct comparison between single and multiple period structures in terms of the expected gain comes along with some incertitude. Due to this, the comparison to the DQW structure as performed in Section 8.1.3, is carried out for the multiple period sample as it reflects best the experimental situation. For the comparison between measured absorption and theory (see Section 8.4), the single period parameters are used for simplicity. This approximation is valid, as the measurement incertitude exceeds the one of the calculations.

Influence of the Ge and SiGe thickness

By using the StepQW, the pump and lasing energy as well as the transitions oscillator strengths can be influenced by changing the thickness of the pure germanium layer and the SiGe layer. In Figure 8.5 this dependence is plotted for the matrix elements of the pumping and lasing transition and the pump energy. The lasing wavelength is not considered in this plot as its influence on the gain is small and its energy is not crucial regarding experimental constrictions. The thickness of the germanium well has most influence on

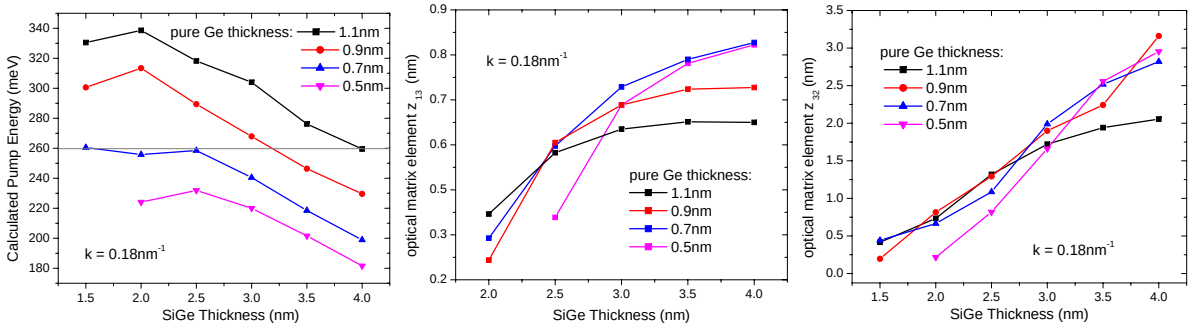

(a) (b) (c)

Figure 8.5: Sample parameters in dependence on SiGe thickness and thickness of the pure Ge well: Pumping energy (a) and optical matrix elements for the pumping transition (b) as well as the laser transition (c). The optical matrix element z_{13} corresponds to the pumping transition HH1-LH2 and z_{32} is the optical matrix element of the LH2-LH1 lasing transition.

the pumping wavelength (Figure 8.5a): For a fixed SiGe thickness of 30Å, the pumping wavelength changes from $\sim$ 310meV to $\sim$ 240meV for a Ge thickness decreasing from 11Å to 7Å. Because of desired excitation energies larger than 300meV, the need of thicker Germanium layers is evident. In contrast to that strong dependence, the Ge thickness has only little influence on the optical matrix elements z_{13} (Fig. 8.5b) and almost no effect on the LH2-LH1 coupling expressed by z_{32} (Fig. 8.5c). The reason for this behavior is the fact that a variation in the Ge thickness only changes the position of the first HH state while the higher lying states are almost not affected. On the other hand, a thicker SiGe layer lowers the pumping energy as the LH2 state shifts to lower energies. Due to the resulting better confinement of the upper laser state, the optical matrix elements of the pumping transition increase. Regarding to the optical matrix elements of the LH2-LH1 lasing transition, the SiGe thickness has tremendous influence (Fig. 8.5c). For a SiGe thickness of 20Å for example, the matrix element is in the range of 0.5nm. This can be improved to 3.0nm by changing the layer thickness to 40Å, hence gaining a factor of six. As the matrix elements go quadratic into the gain formulas, this has a huge impact on the expected gain. For an estimation of the expected gain, the Raman gain was calculated in dependence on the pure Ge and SiGe thickness using formula 7.9. The results of this calculation are summarized in Figure 8.6a. The Raman gain can be improved by an order of magnitude using thick SiGe layers and comparably thin pure Ge layers. But as plotted in Figure 8.6b, one has to take into account the reabsorption losses in the structure. These are given by the amount of absorption at the lasing wavelength. As with thinner

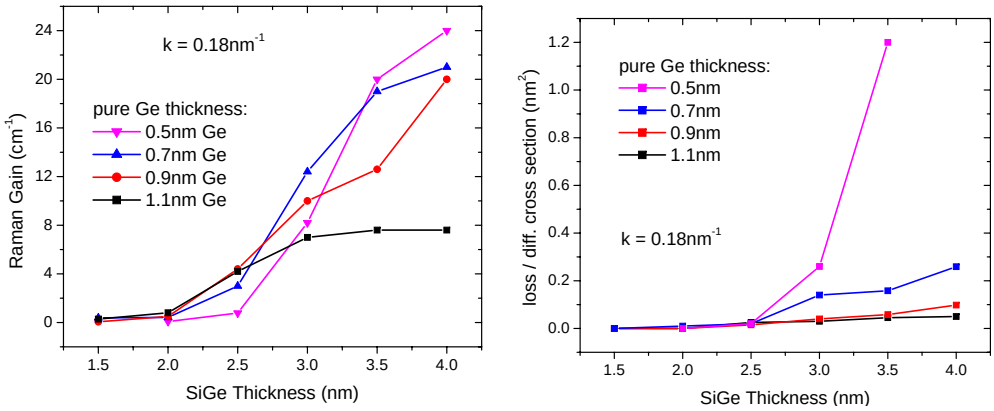

(a) (b)

Figure 8.6: (a) Calculated Raman gain in dependence on the SiGe and the Ge thickness. (b) Loss due to reabsorption calculated from the emission and absorption spectra for each structure.

pure germanium layers and thicker SiGe layers the asymmetry of the structure is more and more broken, the reabsorption losses increase. The choice of the optimum structure therefore has to take into account both effects. For a final proposition of an adequate design, the basic conditions can be summarized as follows: In order to achieve pumping energies between $\sim$ 300meV and 410meV and to keep asymmetry, the SiGe and Ge layers need to be as thick as possible. Structures fulfilling these requirements are composed of 9Å to 11Å thick germanium layers and SiGe layers with a thickness of about $\sim$ 30Å. However, as mentioned before, the realization of this kind of structures is not straight forward as the growth of pure germanium layers is involved. For characterization of the pure germanium growth, four samples were grown in a first step with variations of the Ge thickness between 5Å and 11Å. The discussion of these structures can be found in Section 8.2.3.

8.1.3 Gain Comparison for StepQW and DQW

To summarize the theoretical work, a comparison between the DQW and the StepQW will be given. The discussion is focussed on the Raman gain as lifetime measurements performed in SiGe structures (see e.g. [95],[96]) predict a small population inversion due to short upper state lifetimes of about 100ps. As the Raman gain does not require population inversion, it is the more probable gain mechanism in these structures. The comparison is carried out for a one and a three period structure because the coupling of periods influences the performance of these structures. In Table 8.1, the calculated parameters are summarized. For the single period, the DQW shows a clearly better performance. The matrix elements for both, lasing and pump transition, are larger than for the StepQW. This leads to a Raman gain of 27cm^{-1} for the DQW which is a factor 6 higher than the one for the StepQW (4.5cm^{-1}). Taking into account multiple periods, this factor reduces to 3.5 as the gain per period for the DQW is reduced to 17cm^{-1}. Reason for this is the coupling between the periods. In the DQW, a proper decoupling is not possible as

the barrier thickness is limited by strain compensation requirements. This influences the oscillator strength of the transitions and with it the matrix elements. Besides that, the linewidths are broadened by the coupling between wavefunctions of different periods [3]. In that respect, the StepQW offers the advantage of thicker Si barriers between each period as the total Germanium content is lower. This allows a complete decoupling between the periods. Therefore, the gain per period in the StepQW is not influenced by the number of repetitions and the gain proportional to the number of periods as expected for a well designed QC structure.

The Raman gain was calculated using Equation 7.9. For resonant excitation ($E_{Pump} = E_{13}$),

	DQW		StepQW	
	1per	3per	1per	3per
E_{32}(meV)	227	227	171	171
E_{13}(meV)	325	325	288	288
E_{12}(meV)	98	98	116	116
z_{13}(m)	$0.8 \cdot 10^{-9}$	$0.68 \cdot 10^{-9}$	$0.565 \cdot 10^{-9}$	$0.565 \cdot 10^{-9}$
z_{32}(m)	$2.46 \cdot 10^{-9}$	$2.3 \cdot 10^{-9}$	$2.1 \cdot 10^{-9}$	$2.1 \cdot 10^{-9}$
z_{12}(m)	$2.98 \cdot 10^{-9}$	$4 \cdot 10^{-9}$	$3.34 \cdot 10^{-9}$	$3.34 \cdot 10^{-9}$
Γ_{13}(meV)	60	60	60	60
Γ_{12}(meV)	20	20	20	20
Γ_{32}(meV)	60	60	60	60
N_S(cm^{-2})	$5 \cdot 10^{11}$	$5 \cdot 10^{11}$	$5 \cdot 10^{11}$	$5 \cdot 10^{11}$
k(nm^{-1})	0.18	0.18	0.18	0.18
L_P(nm)	$0.7 \cdot 10^{-8}$	$0.7 \cdot 10^{-8}$	$1.2 \cdot 10^{-8}$	$1.2 \cdot 10^{-8}$
n_{refr}	3.68	3.68	3.55	3.55
Raman Gain (cm^{-1})	27cm^{-1}	17cm^{-1}	4.5cm^{-1}	4.5cm^{-1}

Table 8.1: Table including the calculated sample parameters and calculated Raman gain per period. The Raman gain was calculated assuming all lifetime to be equal ($\tau = 0.1$ps) and the pump intensity of 1MW/cm^2. L_P is the thickness of the active region.

this expression is proportional to the ratio $\frac{z_{13}^2}{\Gamma_{13}} \times \frac{z_{32}^2}{\Gamma_{32}}$. Using this, a fast comparison between theoretically predicted gain and the gain expected from the absorption measurements can be drawn. The Raman gain curves for different detunings are shown in Figure 8.7. For these computations, transition linewidths for the lasing and pump transition as shown in Table 8.1 were assumed. The tuning range which is relatively broad compared to the III-V samples is due to the larger linewidths of the SiGe samples.

For a straight-forward comparison with the experiments, the specification of an expected threshold for the Raman process would be convenient. To do so, a profound knowledge of the waveguide losses in the structure would be necessary. However, as no successful waveguide measurements could be performed by now, this value can not be estimated in

[3] This is not included in the calculations as the impact of this effect on the broadening is not clearly definable.

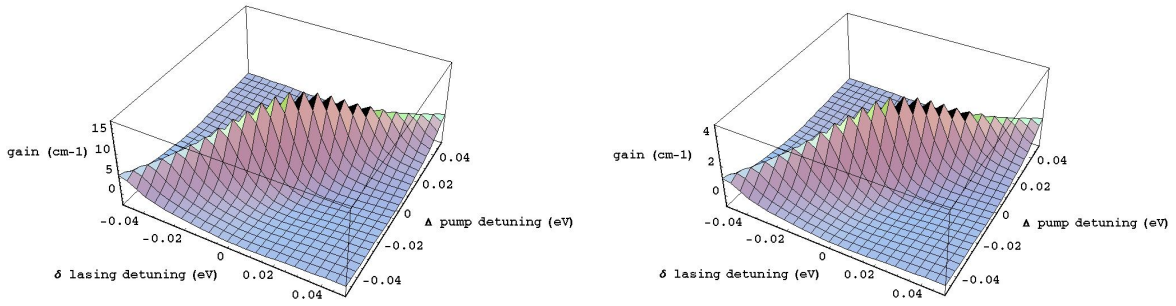

(a) (b)

Figure 8.7: Raman gain in dependence on the detuning of the pump and laser energy for both 3 period structures: (a) DQW structure (b) StepQW structure.

a reasonable way. Therefore, a specification of a Raman threshold at that point would be meaningless. That's why, only the Raman gain expected for the discussed structures is given which can later on be compared to the waveguide losses.
In conclusion, each approach is a trade-off between advantages and challenges: The DQW shows strong coupling between the laser states and the growth on 50% SiGe buffers is well known. Problems of this structure are found in the very thin coupling barrier of about 4Å which gives rise to interface roughness and requires very precise growth. As this design is very sensitive to variations in the layers thickness, an adequate growth of this structure is the biggest challenge. For the StepQW, the growth of the pure Ge on 25% Ge relaxed buffer is the problem which has to be overcome. However, this structure is relatively robust against layer fluctuations and the design can be simply tuned.
In the following sections, the experimental data for the DQW and the StepQW will be shown and analyzed. The design for the DQW was kept as calculated above while the StepQW was investigated in dependence on the pure Ge thickness. The predicted transition energies and corresponding absorption strengths will be experimentally verified and compared to the theory.

8.2 Experiment

Before the discussion of the experiment, some general aspects of the measurements and the data interpretation will be defined. This includes the consideration of the geometrical sample parameters in order to compare theory and experiment. For an interpretation of the absorption in the waveguide structures, the standing wave pattern formed by the interference of the incident light and the light reflected at the surface of the cavity have to be taken into account. In the following, the absorption measurements for the DQW and StepQW will be analyzed. This includes the electrically modulated absorption measurements as well as the direct measurements (see Chapter 5) for the waveguide structures.

8.2.1 General Considerations

In the III-V material system, where the conduction band is employed, all intersubband transitions have a z-component only and are therefore TM polarized. In TE polarization, no intersubband transitions take place. This enables to take absorption measurements as the ratio between the two polarizations (TM and TE) where the TE mode serves as a good reference. In the SiGe material system the valence band is employed and therefore, the polarization of the transitions is much more complex. From this, the need for an appropriate reference spectrum arises. One approach to this problem is the use of the electrically modulated absorption measurements (see Chapter 5). The difference signal between the accumulation of carriers in the active region and the depletion is detected using lock-in technique. Regarding the waveguide structure, the transmission through the substrate without the active region was taken as reference. For this purpose, the outer part of the sample which was covered during the MBE growth was used.
For the measurement, the sample was sandwiched in a copper holder. The two plates of this holder were adjusted in a way, that only the incoupling 45° facet was exposed to the incident light whereas top and bottom surface of the samples were covered by the holder. Using this method, any stray light giving additional transmission signal was excluded.

Geometrical Factor

The absorption calculations presented in the previous section were done for single and triple period samples. For the comparison to the experimental data, the single period calculations will be used. For a quantitative analysis one has to take into account the mode pattern and samples geometry. A schematic drawing is shown in Figure 8.8 for the

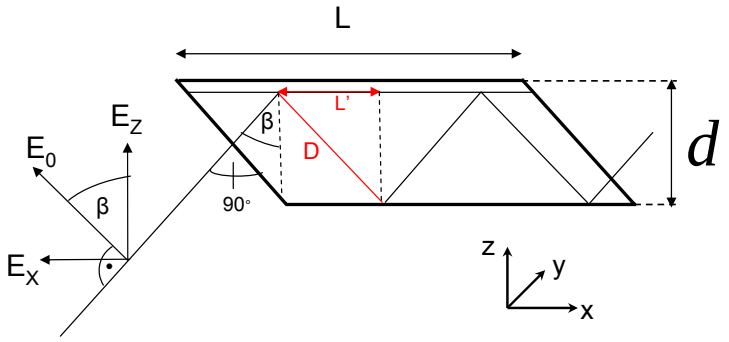

Figure 8.8: Sample geometry employed for the absorption measurements. For the electrically modulated measurements the length $L = 4$mm is defined by the top contacts. For the waveguide measurements, the length could be chosen. The samples were usually thinned down to a thickness of 250μm.

case of TM (or s-) polarized excitation. d and L are the thickness and the length of the structure, respectively. E_0 is the incident electrical field vector at the sample facet and E_Z and E_X its z- and x-polarization components. β is the angle of the incident light. For TE excitation, the incident electric field vector has an y-component only. As the samples

facets are polished at 45°, $\beta = 45°$ in all described measurements. In such a configuration, the light undergoes multiple passes and the interaction length is increased by:

$$\frac{d}{D_{45°}} = \frac{1}{\cos(\beta)}$$

Together with the number of passes $M = L/d$, the total path length of the light in the sample is determined. Besides this, the intensity ($I = n\epsilon_0 c|E_0|^2$) of the incident light needs to be corrected with respect to the incident angle. For this, one has to consider the polarization directions of the electric field separately. For the z component of the electric field in TM mode we find:

$$E_Z = E_0 \cos(\beta); \left|\frac{E_Z}{E_0}\right|^2 = \cos^2(\beta)$$

The x component of the electric field is determined as follows:

$$E_X = E_0 \sin(\beta); \left|\frac{E_X}{E_0}\right|^2 = \sin^2(\beta)$$

In TE mode, the y-component is equal to the incident electric field: $E_Y = E_0$. These three values give the so-called geometrical factor G of the considered structure. Summarized, this reads in z-polarization:

$$G_Z = M \times N \times \frac{1}{\cos(\beta)} \times \cos^2(\beta) = M \times N \times C_1$$

and for the x component:

$$G_X = M \times N \times \frac{1}{\cos(\beta)} \times \sin^2(\beta) = M \times N \times C_2$$

For the y-component in TE mode one finds:

$$G_Y = M \times N$$

N is the number of periods which needs to be taken into account as the calculations were done for one period only. Using the differential cross section σ from the calculations, the expected absorption can be calculated:

$$Abs = \sigma \times M \times N \times C \times N_S \tag{8.1}$$

where N_S is the sheet carrier density. For the electrically modulated measurements, N_S is the carrier density modulated by the applied voltage.
Using the 45° geometry, the calculation is simplified as the factor $C = C_1 = C_2 = \frac{\sqrt{2}}{2}$ becomes equal for all polarizations. It has to be noted, that for the calculation of the differential cross section a certain linewidth was assumed. Therefore, the ratio between assumed and measured linewidth has to be considered for a detailed analysis. The last factor which should be included is the overlap factor of the incident light with the concerned waveguide mode in TM or TE. For the electrically modulated measurements the

situation is defined by the metal contacts on top and the active layers very close to the sample surface. The metal will influence the TE mode in the way that it has a node at the surface since $E_{X,Y}(z = 0) \sim 0$ for a good conductor. Consequently, the TM mode of the standing wave has a crest at the surface. As the QWs are located directly underneath the surface, the z overlap factor (which is the main TM component) is considered as 1 while the overlap with the x and y polarization (and hence with the TE component) is very small. This leads to a weak TE intensity and a pronounced TM absorption. In the case of direct transmission measurements as performed for the waveguide structures with a thick and buried active region, the overlap factor can not be defined in such a general way. The discussion on the treatment of the overlap factor and its wavelength dependent effects for these measurements is discussed in the next subsection.

Standing Wave Pattern

The following discussion is of interest for the waveguide structures only. In the electrically modulated absorption measurements, contributions from the wavelength dependent overlap factor of the active region with the standing wave pattern formed in the cavity are negligible as the active region close to the surface simplifies the situation. For the waveguide structures however, the thick cladding layer on top of the active region makes this technique unsuitable. Therefore, the absorption is measured via a direct transmission measurement. This implies that no modulated differential measurement as the lock-in method is used. Because of this, effects due to the wavelength dependence of the overlap factor need to be taken into account. Our approximate approach is briefly introduced in the following.

The incident light which enters the sample via the 45° facet (see Figure 8.8) is reflected

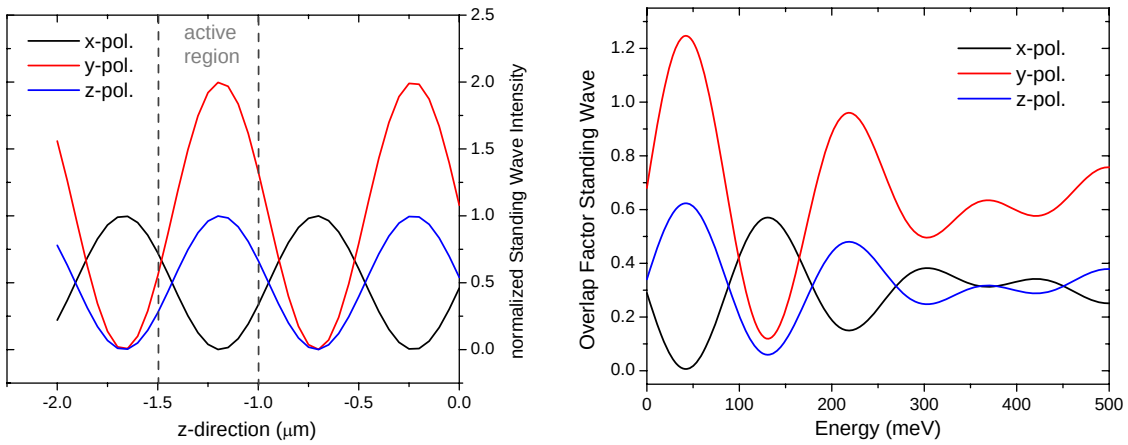

(a) (b)

Figure 8.9: (a) Standing wave pattern for the 45° geometry calculated at wavelength of 5mum. The surface of the sample is at $z = 0$, the negative z-direction goes into the sample volume. The dashed lines indicated the active region. (b) Overlap with the active region in dependence on the energy.

at the sample surface. The incident and reflected beam interfere and form a standing

wave pattern with a period of $\frac{\lambda}{2n}\cos\beta$ involving the wavelength λ and the refractive index n. The position of the nodes have to be determined from the boundary conditions as can be found for example in [130] and [131]. A calculation of the intensity pattern on the basis of the above mentioned literature is shown in Figure 8.9a. In the example, the refractive index $n = 3.68$ of a 50% SiGe buffer was taken. $z = 0$ corresponds to the top surface of the sample. An active region of 0.5μm with a 1μm cladding on top and a total sample thickness of 250μm was assumed. The calculation shows that the intensity of the standing wave in y- and z-polarization are almost in phase and are shifted about 180° with respect to the x-polarization. In y-polarization, the strongest intensity within the active region is achieved. As for the analysis of the absorption only the intensity in the active region is of interest, the overlap factor of the standing wave with the active region was calculated in dependence on the wavelength (Figure 8.9b). The resulting overlap factors are strongly wavelength dependent and show strong modulation in the wavelength range between 0meV and 300meV which is also the energy range for the expected intersubband transitions. For the analysis of the waveguide structures, these calculations were performed for each sample using the appropriate parameters. The results of this can be found in the corresponding sections.

8.2.2 Double Quantum Well Structure

The Double Quantum Well structure was grown on 50% SiGe relaxed buffer. The first sample consisted of 300 periods (2.1μm) active region with only a thin 50% SiGe cladding layer of 300Å on top. On this sample, electrically modulated absorption measurements were performed. In a second run, a 60 period sample with a 1μm cladding layer was grown which was used for waveguide absorption measurements. Both samples were thinned down to a thickness of 250μm and polished in the 45° geometry.

Electrically modulated Absorption measurements

The absorption spectra shown in Figure 8.10 for TM and TE polarization were taken at a temperature of 70K. The voltage for the carrier modulation was varied between −1V and +2V. The setup for this measurement was described in Chapter **??**. A well pronounced peak at $\sim$ 100meV was found in the TM polarization. By comparison to the calculated spectrum, this peak was assigned to the HH1-HH2 transition. The expected pumping transition (HH1-HH3) around 325meV can not be identified. The same behavior was observed in the TE polarization. The low energy peak at around $\sim$ 100meV is identified as the HH1-HH2 transition mixed in TE. Higher lying states however are either shifted from their calculated energy or not present. This suggest that the growth of the 4Å barrier causes problems as the thickness of this barrier mainly influences the position of higher lying states.
To compare the peak absorption to the calculation, the HH1-HH2 in TM polarization was analyzed: The sample thickness is $\sim$ 250μm and the length 4mm. This gives a total of 16 passes of the light within the sample. With the applied voltage of $-1V/+2V$, a total

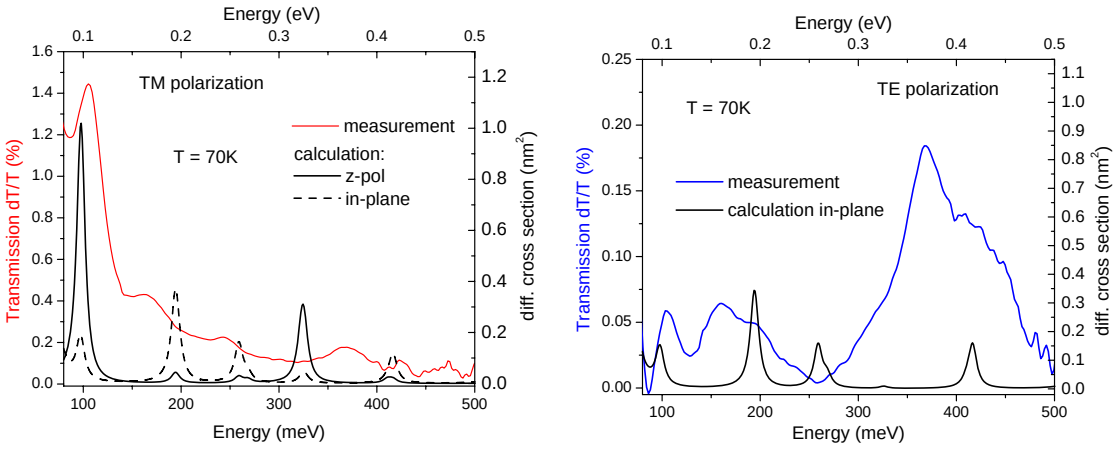

(a) (b)

Figure 8.10: Electrically modulated absorption spectra in TM (a) and TE (b) polarization compared to calculation the DQW structure. The applied voltage was varied between $-1V/+2V$ with 1kHz.

carrier density of $1 \cdot 10^{12}\text{cm}^{-2}$ in the whole active region is modulated (see Chapter 5). From the calculations, a differential cross section of 1.1nm^2 was obtained. This cross section is a sum of the z-polarization (1.0nm^2) and the x-polarization (0.1nm^2) as these are the TM components (see calculated spectra in Figure 8.10). It has to be noted that the mixing with the TE mode can be neglected for this configuration because of the metal contacts on the surface. Using the above values in equation 8.1, an expected absorption of 12% can be found. Taking into account the ratio between the linewidth assumed for the calculation (5meV) and obtained from the measurement (30meV), the final absorption expected from the calculations is 2.1%. From the measurement, an absorption of 1.3% was obtained. This deviation can probably be ascribed to the incertitude of the incident angle, linewidths, sample thickness and the modulated carrier density. Despite of this fair agreement between theory and experiment, the missing HH1-HH3 peak indicates growth problems.

Waveguide Absorption

The results of the direct transmission measurement at a temperature of 70K are shown in Figure 8.11. For the TM polarization, the spectrum looks comparable to the one obtained in the electrically modulated absorption measurement except for the broadened lines. A well pronounced peak at about 100meV is observed while the HH1-HH3 peaks is missing. In TE polarized spectrum, two clear but very broad peaks are observed. The third one below 100meV is only indicated in the spectrum due to the cut off of the detector. Compared to the calculation, the peaks at $\sim$ 200meV and 400meV seem to be in agreement with the predictions. However, as mentioned in the previous section, for this kind of measurements the overlap of the standing wave patterns of the incident light with the active region can not be neglected. In Figure 8.12 this overlap factor calculated for the corresponding sample parameters is shown together with the absorption data. As the

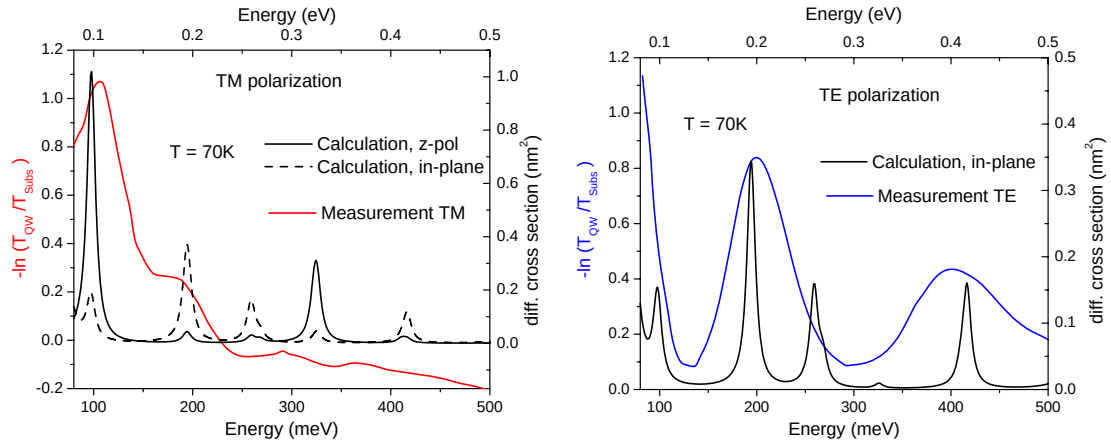

Figure 8.11: Waveguide absorption spectra in TM (a) and TE (b) polarization. As comparison, the calculated absorption spectrum is plotted.

TM polarization consists of equal parts of x- and z-polarization, no immediate analysis between standing wave intensity and absorption data can be given. In the TE polarized data, the similarity between overlap function and observed absorption is striking as peaks and valleys of both spectra coincide to a large extend. An attempt of interpretation was performed in which the measured absorption was referenced to the overlap factor. As the TE polarization consists of an y-component only, the measured spectrum can be directly divided by the overlap factor of the standing wave. The spectrum obtained by this procedure is shown in Figure 8.13b. To obtain the x correction, one has to take into account the y-polarized part mixed to the TM absorption. Therefore, half of the pure TE

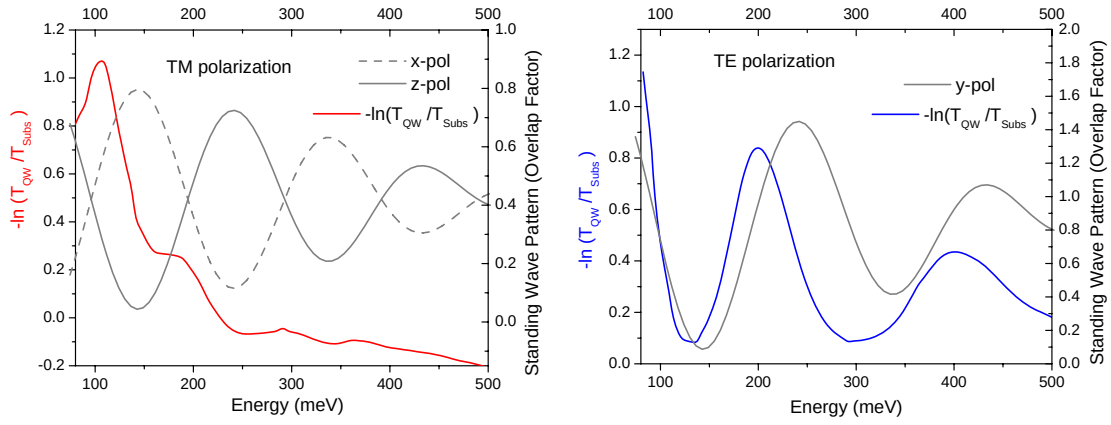

Figure 8.12: Waveguide absorption spectra in TM (a) and TE (b) polarization. The wavelength dependent overlap factors of the standing wave with the active region for the corresponding polarization are also plotted.

absorption calculated above was multiplied with the x-polarization overlap factor. This part was then subtracted from the TM absorption and the result finally divided by the z-polarized overlap. The resulting absorption spectrum is shown in Figure 8.13a. Here,

the weak points of this analysis become evident. Large peaks of the spectrum become negative as the truncated spectrum is obviously larger than the measured TM spectrum. This problem arises from an insufficient accuracy of referencing the active region signal to the substrate. As a consequence, any additional background signal induced error may

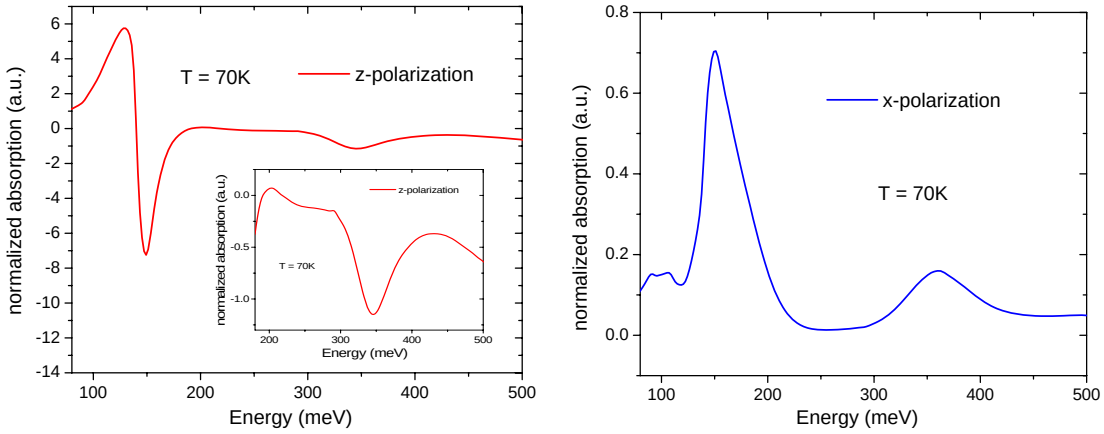

(a) (b)

Figure 8.13: Corrected absorption spectra in z and x polarization. For the x-polarized part of the absorption, the TE measurement was first divided by the overlap factor in y-polarization and then corrected for the x-polarization. The TM was corrected for the TE part and referenced to the overlap factor for z-polarization which gives the z-polarized contribution to the absorption. The inset shows the zoom of the energy range between 200meV and 500meV.

cause a change in sign for the corrected absorption. The following conclusion are thus to be taken with great care. First, the observed peak at 100meV in TM may indeed originate from the HH1-HH2 transition. Considering the other peaks at 340meV in TM and at 150meV and $\sim$ 400meV in TE, a comparison to the peaks of the overlap factor is necessary in order to decide about their interpretability. From Figure 8.12, one finds that these values are close to the overlap maxima and minima (145meV, 240meV, 340meV and 430meV) obtained in the calculations. This remaining features may mainly be caused by a broad background absorption modulated by the standing wave intensity. The reasons for this very broad absorption are probably inhomogeneities and waviness within the grown structure or additional absorption in the cladding layer. As neither electrically modulated absorption spectra nor the waveguide absorption showed the presence of three well defined levels, it has to be concluded that this type of design is not suitable for our purpose. The most obvious reason for this is that the growth quality necessary for a promising three level system using this kind of system can not be achieved with our MBE. Consequently, our attempts to achieve lasing by optical pumping on these structures had to fail.

8.2.3 StepQW structure

For the StepQW design, the growth of pure germanium on 25% Ge relaxed buffers was first characterized using samples with different thicknesses of the germanium well. The germanium thickness was varied between 5Å and 11Å. A set of absorption samples for

electrically modulated measurements was grown. These structures were composed of 5 periods of the StepQW (i.e.: 26.5Å Si, 11Å Ge, 20Å $Si_{0.5}Ge_{0.5}$, 26.5Å Si) and a cap layer of 500Å. The samples were prepared and measured in the multi-pass configuration (see Chapter 5).
For the waveguide samples, the active region was repeated 60 times and a cap layer of 1μm was added. The doping concentration was kept around $4 \cdot 10^{11}\text{cm}^{-2}$ per period. The samples were thinned down to a thickness of about 250μm and the facets polished at 45°. The absorption measurements were taken in the same way as for the DQW structures, i.e. using the transmission through that part of the sample which was shadowed during MBE growth as reference measurement.

Electrically modulated Absorption measurements

The first electrically modulated absorption measurements were performed on the 7Å sample. The thickness of the Si barriers was adjusted to 20.5Å in order to ensure the strain compensation which allows a total Ge amount of 25% for the growth on $Si_{0.75}Ge_{0.25}$ buffer. The upper Si barrier was Boron doped at a level of $2 \cdot 10^{18}\text{cm}^{-3}$ which results in a sheet carrier density of $4 \cdot 10^{11}\text{cm}^{-2}$ per period. The absorption spectra shown in Figure 8.14 was taken at 70K with a modulation signal of $-1V/+2V$ at 1kHz. In the TM polar-

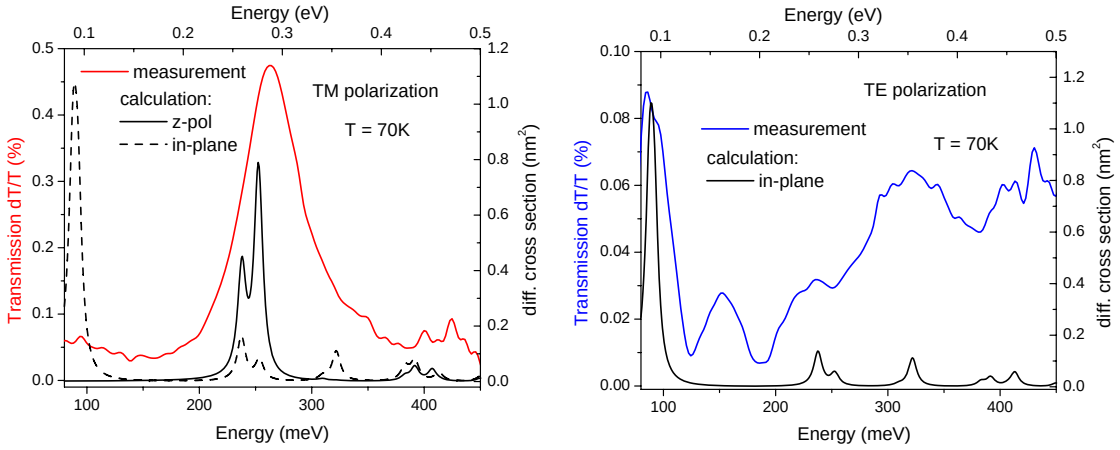

(a) (b)

Figure 8.14: Electrically modulated absorption spectra in TM (a) and TE (b) polarization compared to calculation for the StepQW with 7Å pure Ge. The applied voltage was varied between $-1V/+2V$ with 1kHz.

ization, the data are in very good agreement with the calculation. The peak at 264meV corresponds well to the value predicted in the simulations and is assigned to the mixed HH1-HH2/LH2 transition. The peak absorption for this transition is 0.43% (corrected for the background). As the sample geometry is the same as discussed for the electrically modulated absorption of the DQW structure, the factors in Equation 8.1 for the calculation of the absorption from the calculated differential cross section are: $M = 16$, $C = 0.707$ and the TM overlap factor is 1. The number of modulated carriers in the

active region is $1 \cdot 10^{12}\text{cm}^{-2}$. From the calculated spectrum, we find a peak differential cross section of 0.9nm^2. Adapting this to the sample geometry using the geometrical factor including the above values, a peak absorption of 10% is expected. The measured linewidth is $\sim$ 60meV which gives a factor 0.08 with respect to the assumed linewidth of 5meV. Taking this ratio into account, the absorption expected from the calculation is 0.8% which is in reasonable agreement with the measurement. In the TE absorption, the HH1-LH1 transition at 100meV and probably the mixed HH1-HH2/LH2 transition at $\sim$ 250meV can be resolved. The quality of the obtained spectrum in TE is worse than for the TM measurement because of the low TE overlap factor.
Based on these measurements it can be concluded that the growth of a 7Å germanium well on 25% buffer is possible. However, regarding to the optical pumping experiment, the obtained energy of $\sim$ 250meV for the HH1-LH2 pumping transition is too low. To shift this to higher energy, thicker germanium layers are necessary. As obtained from the calculations (see section 8.1), thicker Ge wells are also advantageous for the gain in the active region. Therefore, a structure with an 11Å pure Ge well was investigated. The obtained absorption spectra are shown in Figure 8.16. In the TM polarized spectrum we

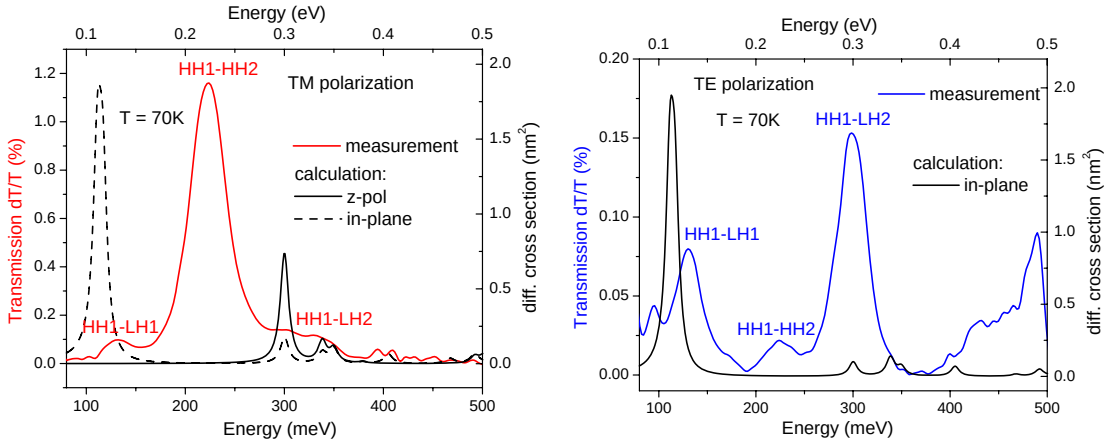

Figure 8.15: Measured Absorption in TM (a) and TE (b) polarization for the StepQW structure with 11Å pure Ge. The measurements were taken at 70K and the applied voltage was $-1V/+2V$ modulated at 1kHz.

find a strong absorption peak at around 220meV. Furthermore, a small peak at 130meV is found and a plateau at 300meV in the high energy tail of the strong peak. In TE, we find strong peaks at 130meV and 300meV and a small one at 220meV. Comparing the peak energies in the two polarization directions allows to assign the obtained peaks as follows: The absorption at 130meV originates from the HH1-LH1 transition which is strongly mixed in TM and TE. The strong peak at 220meV is more pronounced in the TM polarization and can be assigned to the HH1-HH2 transition. Finally, the absorption at 300meV which is mainly TE polarized can be identified as the pumping transition HH1-LH2. In this comparison one has to keep in mind that the TE mode is much less pronounced in these structures due to the metal contacts on top. As all peaks are mixed

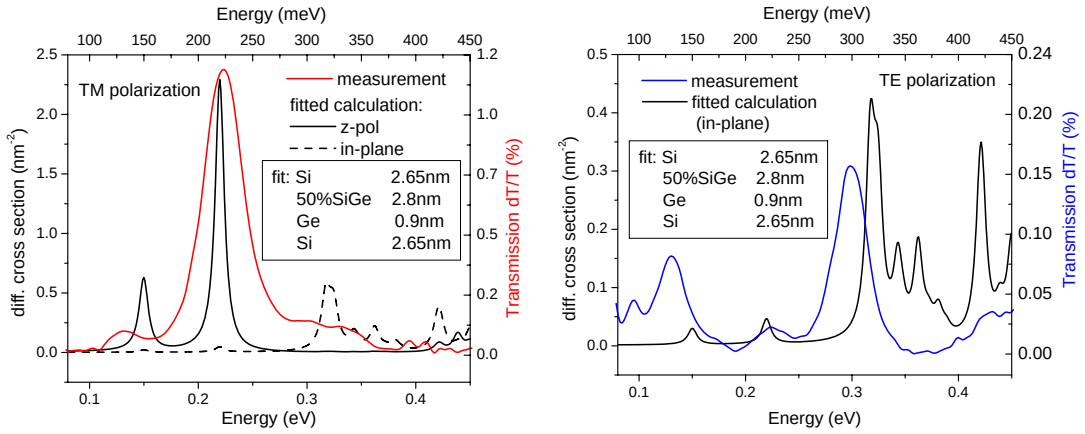

Figure 8.16: Fit of the measured absorption spectra in TM (a) and TE (b) polarization for the StepQW structure with 11Å pure Ge.

in TE and TM polarization, the carriers are distributed to high inplane k-vectors. The comparison of these data to the theory however shows a clear disagreement. The HH1-HH2 peak is shifted of about 80meV towards lower energies while the LH1 peak is shifted about 20meV higher and the HH1-LH2 peaks agrees to the expected energy. By fitting of the measured absorption spectra it was found that the shift of energies is due to a slight change of the layer thicknesses: Assuming a thickness of 9Å for the germanium layer and 28Å for the SiGe layer, the measured transition energies can be modelled. However, this result only corresponds to an averaged value as the spot size of the glowbar light $\sim$ 1mm is much bigger than possible variations in the layer thickness. This includes, that the actual deviations in the layer thickness are probably bigger. The TEM pictures shown in Figure 8.17 support this interpretation: In the overview picture in Figure 8.17, one can

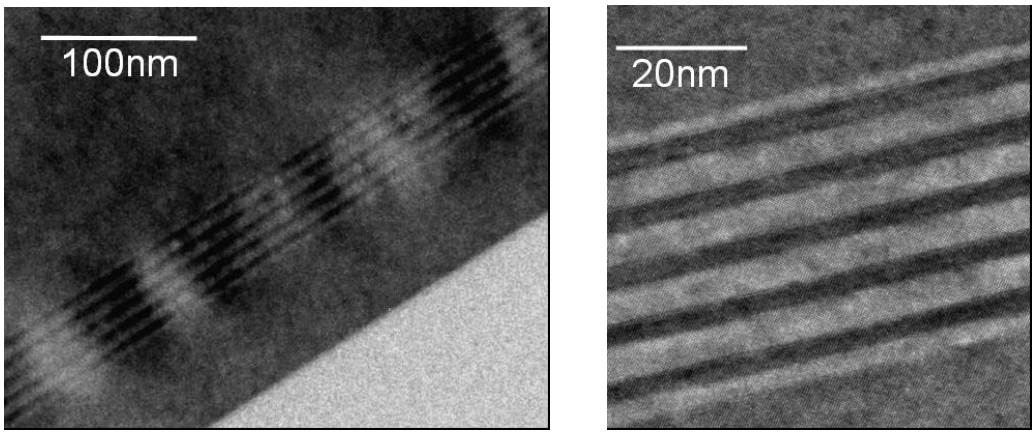

Figure 8.17: TEM pictures of the 11Å pure germanium sample: Overview (a) and zoom (b) of the 5 period active region. The bright lines are the Si rich layers, the dark lines the Ge wells. The bright and dark areas in the overview picture indicate strain fields due to germanium island forming.

identify darker (Ge rich) and brighter (Si rich) regions in the area of the 5 period active region which indicate a wavy structure. Above a critical thickness, the Germanium starts to form islands and dots which leads to an inhomogeneous and wavy structure. This indicates that the growth of such thick pure Ge layers is difficult to control and one is limited by the material conditions. The analysis of the peak absorption however proves the robustness of this design. The measured peak absorption of the HH1-HH2 peak is 1.2%. The differential cross section for this transition is calculated to 0.8nm^2. Using the same values for geometrical factor, overlap and modulated carrier density as for the 7Å sample, this converts into an expected absorption of 0.9% which is in very good agreement with the experiment. For the TE polarized HH1-LH2 peak, a factor 2 difference between measured and predicted value is obtained. This good agreement regarding to the absorption strength shows that this kind of design is quite insensitive to slight changes in layer thicknesses which is a clear advantage compared to the DQW structures.

The electrically modulated absorption measurements for StepQWs with different germa-

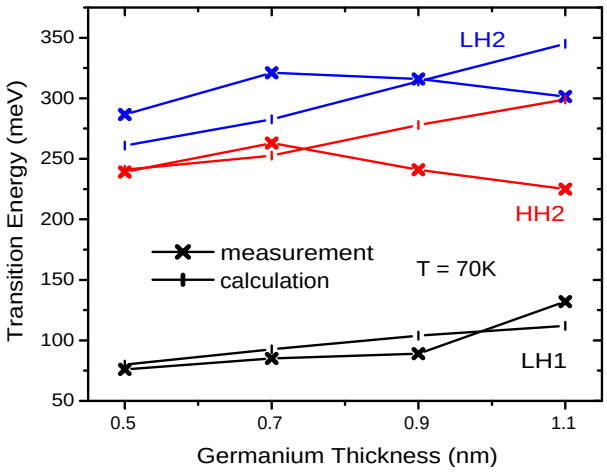

Figure 8.18: Summary of the transition energies for StepQWs with different pure Ge thickness: The measured and calculated transition energies are plotted versus the Ge thickness.

nium thickness are summarized in Figure 8.18. The transition energies are plotted versus the width of the germanium wells. For the smaller Germanium thicknesses, calculation and experiment are in good agreement. For Ge layers $\geq$ 9Å, the experimental and calculated energies differ from each other. This shows that Ge thicknesses up to 9Å on 25% buffer can be grown well controlled. A possibility to grow even thicker Germanium layers in a controlled way is the use of buffers with lower germanium concentration. When the average germanium content is decreased, the germanium can be grown thicker without the formation of Ge islands because the layers are less strained. A series similar to the one discussed above was grown on the 20% buffers. However, the quality of the data taken for those samples did not allow a conclusive statement and is therefore not presented here.

Waveguide Absorption

For the investigation of waveguide structures, samples with a 7Å, 9Å and 11Å pure Germanium layer were grown. For the detailed discussion, the 7Å sample will be presented here. In Figure 8.19, the absorption measurement taken at 70K is shown in comparison to the calculations. In the TM polarization, we find a strong peak at 260meV which is

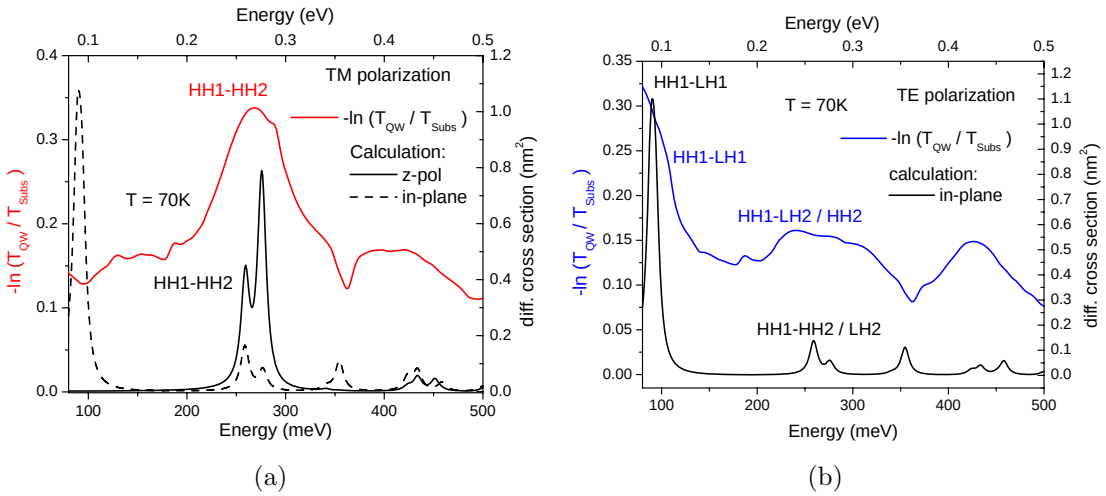

Figure 8.19: Waveguide absorption spectra in TM (a) and TE (b) polarization for the 7Å pure Ge sample. The main resonance in TM is the HH1-HH2 transition and in TE the HH1-LH1 transition. The pumping peak HH1-LH2 around 260meV is comparably weak. For the comparison with theory, the calculated absorption spectrum is plotted.

in good agreement with the calculated value and with the peak energy obtained from the electrically modulated measurement. In the TE polarization, the first peak (HH1-LH1) is slightly down-shifted and the mixed HH1-HH2/LH2 peak is in a good position but very broad. Both spectra seem to be superimposed on a big background absorption of up to 12%. For the comparison of the measured peak absorption to the predicted value, the background signal was subtracted from the spectrum. For the strong TM peak, an absorption of 22% was obtained. The geometrical factor is obtained from the number of passes $M = 26$, the coupling factor C of 0.707, the number of periods $N = 60$ and the doping per period $N_S = 4 \cdot 10^{11}\text{cm}^{-2}$. The experimental linewidth is 75meV which gives a factor of 0.07 with respect to the linewidth of 5meV assumed in the calculations. With the calculated total differential cross section of 1nm^2 taking into account z- and x-polarized light, the peak absorption of 31% is predicted. These values seem to be in reasonable agreement with the measured peak absorption of 22%. However, as already discussed for the DQW waveguide structures, the wavelength dependence of the overlap factor of the standing wave pattern formed in the cavity has to be taken in to account. The plot of the measured absorption spectra with the overlap factor is shown in Figure 8.20. It is obvious that the absorption spectra are strongly influenced by the intensity modulation of the overlap factor. In TE mode, the absorption peaks coincide with the peaks of the standing wave pattern. From these data, the pumping transition could not be clearly resolved. In TM, the well resolved peak agrees with an intensity maximum of the z-polarized over-

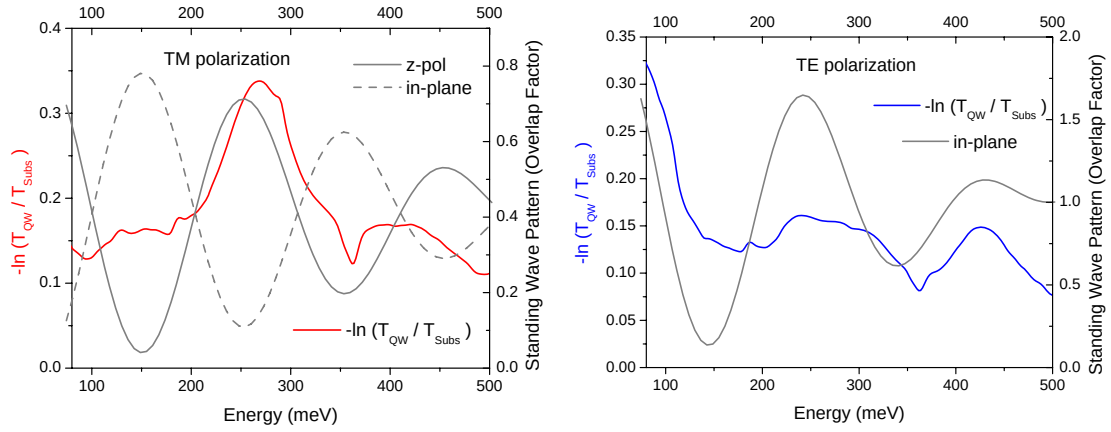

(a) (b)

Figure 8.20: Waveguide absorption spectra in TM (a) and TE (b) polarization for the 7Å pure Ge waveguide structure. The wavelength dependent overlap factors of the standing wave with the active region for the corresponding polarization are also plotted.

lap factor. This suggests that it is mainly due to the intensity modulation. However, in comparison to the electrically modulated absorption measurements as well as to the theory, an intersubband transition is predicted at this energy. Hence, it can be stated that part of this transition is probably originating from an intersubband transition. A quantitative analysis however is impossible due to the big impact of the standing wave intensity modulation.
The same kind of problem was found for the other waveguide structures grown on 25% buffer. Also the tested waveguide structures grown on 20% buffers showed similar behavior. None of them showed features which could be clearly attributed to intersubband resonances.

8.3 Conclusion on SiGe optically pumped structures

In this chapter, two different approaches for the realization of a SiGe structure for optical pumping were investigated. In the first design, the necessary asymmetry was achieved using a double quantum well coupled via a thin barrier (DQW). In the second design, a pure Ge layer was inserted on one side of a $Si_{0.5}Ge_{0.5}$ quantum well giving a step profile in the band diagram (StepQW). The theoretical comparison of these two structures showed that for a multiple period sample the StepQW is clearly advantageous with respect to the expected gain.
The electrically modulated absorption measurements of both structures were discussed. For the DQW, the pumping transition could not be resolved. The measurements for the StepQW showed good agreement with the theory regarding peak position and absorption strength. For the StepQW, a linewidth of about 60meV for the pumping as well as the HH1-HH2 transition was obtained. This suggest the same linewidth for the lasing transition. Correcting the assumed values in Table 8.1, this leads to an around six times

lower Raman gain than expected. For the DQW, the correction on the gain values must be even higher as the pumping transition could not be clearly resolved.
The subsequent measurements of the absorption in thick waveguide structures with a 1μm cladding on top did not allow a clear interpretation of the data. This is due to the strong impact of the energy dependent overlap factor of the standing wave pattern with the active region. Reason for the tremendous impact of the standing wave pattern on the absorption is the presence of a very broad background absorption up to 12% which is spread over the whole considered energy range. This includes, that for the SiGe structures no absorption peaks exceeding 12% were observed. For the origin of this background absorption, two possible explanations were given: First, the 1μm thick cladding layer on top of the active region which is not taken out by referencing to the substrate. Another possible reason for a broad absorption may be found in the inhomogeneity of the thick waveguide structure causing an intersubband absorption which is distributed all over the considered wavelength range. As one has to consider TM and TE polarized absorption as well as mixing of the both, the interpretation of these data is not conclusive. In order to improve these measurements, the origin of the background absorption has to be clarified. Here, absorption measurements on waveguide structures with an etched cladding layer should be performed.
The absorption experiments in waveguide geometry clarify that basic requirements for optical pumping structures could not be fulfilled: It was not possible to realize a proper 3-level waveguide structure in the silicon-germanium material system. No well resolved pumping transition above $E > 250$meV was obtained. Observed transitions were rather broad and a distributed background absorption results in strong losses as discussed before. An investigation on the nature of this background is necessary in order to give a conclusive answer on the quality of the grown structures.
Finally, it has to be mentioned that the SiGe samples were tested in the optical pumping setup. With a pump pulse power of 0.42μJ on the samples facet, lasing could not be achieved for any of those samples. This shows, that the threshold of the SiGe samples is at least a factor 5 higher than for the III-V devices. A conclusive statement is hard to give as lifetimes and waveguide losses are difficult to predict. However, only taking into account the 6 times broader linewidths of the SiGe samples compared to the III-Vs, lasing can not be expected at this power. In that respect, one of the most important requirements to achieve lasing is to improve the linewidth of at factor 2 to 4. Besides this, the precondition for lasing, a well defined absorption peak at the pumping transition and low losses, needs to be fulfilled. As these requirements could not be achieved with the present samples, no lasing action was obtained.

Chapter 9

Summary and Conclusion

Since their first demonstration in 1994, quantum cascade lasers have attracted lots of scientific interest as they offer great potential applications in, e.g., data communication and molecular spectroscopy. Lasing action has been demonstrated in several III-V material systems like InGaAs/InAlAs, GaAs/AlGaAs, InAS/GaInSb/AlSb. In terms of applications, a quantum cascade laser realized in the Si/SiGe system is of special interest because of its possible compatibility to the state-of-the-art silicon technology for most electronic components. This would connect two requirements: the silicon light emitter with a wavelength which can be adjusted by design to cover the mid-infrared wavelength range. As QCLs are based on intersubband transitions, they present the advantage of not being limited by the indirect band gap of the silicon material.
The goal of the present thesis has been to explore the approach of an optically pumped SiGe quantum cascade laser. Within the work on electrically pumped SiGe QC structures, achievements regarding injection current densities, contact and waveguide design for a better carrier mobility and lower free carrier absorption have been made. For example, injection current densities of $J = 6.5\text{kA/cm}^2$ were demonstrated. By using Multiple Quantum Wells (MQW) as electrical contacts, the carrier mobility could be improved to $0.44\text{m}^2/\text{Vs}$ while the expected free carrier losses are reduced to 5cm^{-1}. A sophisticated waveguide design was developed in which contact and optically active region are laterally separated and therefore, losses are reduced. However, despite this progress, the performance of the SiGe QC structures still needs to be improved by a factor of 10 in order to overcome the calculated losses. The main approaches for this are improving linewidth, injection current density as well as upper state lifetimes. As these requirements are difficult to overcome with respect to the growth (interface roughness, accuracy) and the physical limitations of the material (i.e. intermediate states which reduces upper state lifetime), the optical pumping was chosen as approach towards the SiGe light emitter. This implied several advantages like i.e. simplified design including less intermediate states, no electrical contacts and a less critical growth as the injection of carriers is provided by an external laser source. The latter one is of course a drawback with respect to possible applications but well suitable for the test of the idea of a SiGe QCL.
The setup for an optical pumping experiment was built up and tested using III-V double quantum well structures. All investigated samples showed lasing action which confirmed

the functionality of the setup and the suitability of the approach. Lasing with an output power of about 14W and a conversion efficiency of 1.3% was found. The gain process in these structures was found to be Raman-type which was indicated by the shift of the lasing wavelength with the pump wavelength as well as the low conversion efficiency. However, it was found that this kind of gain mechanism is promising for the SiGe material system as it is a nonlinear two photon process and therefore, does not depend on long upper state lifetimes. This was also shown by the calculation of the Raman gain in dependence on the lifetime.

For the SiGe structures, two designs were investigated: a double quantum well (DQW) structure similar to the III-V samples and a step quantum well (StepQW) structure for which a germanium well was introduced on one side of a 50% SiGe layer. It was found from the calculations, that for the growth of multiple periods, the double quantum well is limited due to strain compensation requirements. Furthermore, the StepQW seems to be advantageous with respect to the linewidth and the number of intermediate levels. The designed emission wavelength was in the range of 5μm while a pump energy between 300meV and 400meV is required by the setup. The DQW structures were grown on 50% SiGe relaxed buffer while for the StepQW pseudosubstrates with 25% germanium were used. As a first characterization, electrically modulated absorption measurements were performed. Peaks at higher energies (above 200meV) could not be resolved for the DQW which implies that the peak of the pumping transition was not detected. For the StepQW, samples with different width (5Å - 11Å) of the Ge well were grown. It was found, that the growth of pure germanium on 25% relaxed buffer is well controllable up to a width of $\sim$ 7Å. The obtained transition energies agree well with the theory in that case. For thicker germanium layer, the transition energies deviate from the theory but the absorption strengths are still in reasonable agreement with the theory. This proves the robustness of this design.

After these preliminary investigations, absorption measurements on samples containing a thick active region and a 1μm cladding layer as waveguide were grown. However, neither the DQW structure nor the StepQW samples showed clearly interpretable spectra. This was due to a huge background absorption of up to 12% which was modulated by the intensity of the incident light. The reason for this background can either be found in a constant absorption in the cladding layer or in a not controllable growth of the 60 period structures. The latter one leads to wavy structures which can result in a small but very broad absorption peak distributed over the whole wavelength range. To clarify the origin of the background absorption, measurements on samples with etched cladding layer will be performed.

Finally, it has to be noted, that all samples tested in the optical pumping setup did not show any lasing action as expected from the above results.

In conclusion, the goal of the thesis, the realization of an optically pumped SiGe laser could not be achieved. For a successful realization of a SiGe optically pumped laser, different issues need to be clarified or respectively improved. This is on the one hand the origin of the absorption background which needs to be identified. Furthermore, the transition linewidths have to be improved of a factor 2 to 4. This requires detailed analysis

of the substrate quality and improved growth conditions. A laser will be realized as soon as well resolved absorption in waveguide structures can be demonstrated.

Appendix A

Samples on new SiGe pseudosubstrates

In this appendix, the latest SiGe samples are briefly described. For those samples, the step QW design was optimized using the results in Section 8.1: A 9Å wide Germanium well was grown followed by a 30Å thick SiGe layer. Those layers were embedded into Silicon barriers whose thickness was adjusted to the germanium content of the substrate in order to achieve strain compensation. Samples on 20% and 25% germanium relaxed buffer substrates were grown with barriers thicknesses of 28.5Å and 40.5Å, respectively. This active region was repeated 60 times. In order to clarify the influence of the cladding layer (as suggested in Section 8.3), a sample with and without a 1μm cladding layer was grown on each substrate. The results obtained from these structures are summarized below.

A.0.1 Substrates

For the growth, new pseudosubstrates from CEA-LETI were used. The X-Ray measure-

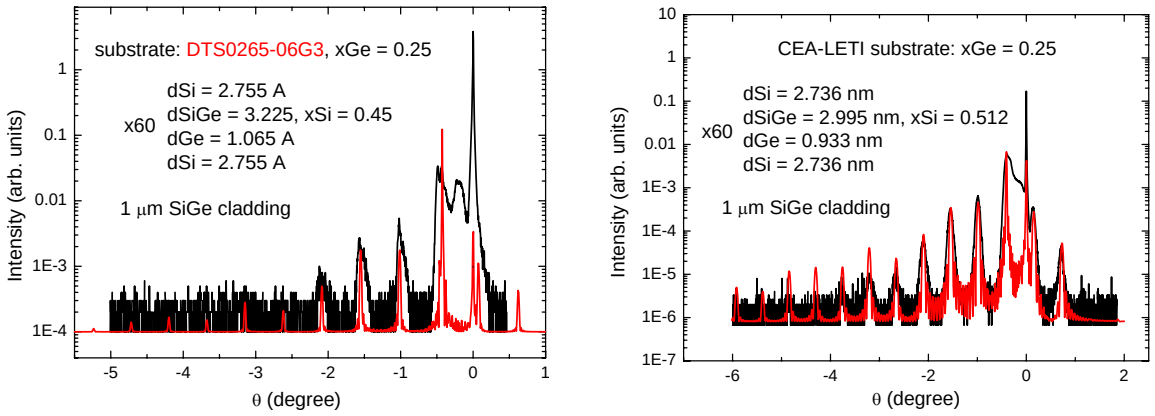

(a) (b)

Figure A.1: Angle-resolved X-Ray diffraction pattern of samples grown on STMicroelectronics substrates (a) and CEA-LETI substrates (b).

ments carried out by Gregor Mussler at the RWTH Aachen showed a significant difference compared to the structures grown on old STMicroelectronics substrates (Figure A.1). The XRD data of the sample using STM substrates show few and broad satellite peaks (Fig. A.1a). In comparison to this, the XRD of the structures grown on CEA-LETI substrates show many satellite peaks which are well pronounced and narrow. This includes that the latter substrates show a clearly better structural quality which has an intermediate influence on the quality of the epitaxial layer grown afterwards. Further measurement of the reciprocal space map for those samples confirmed the results. The CEA-LETI substrates showed a clearly smaller width of the pseudosubstrate peak which indicates a smaller dislocation density. On the basis of those results, all the samples described in the following were grown on CEA-LETI substrates.

A.0.2 Theory

For completeness, the band structures of the 20% and 25% germanium sample are shown in Figure A.2a and b. The difference in the germanium concentration of about 5% causes

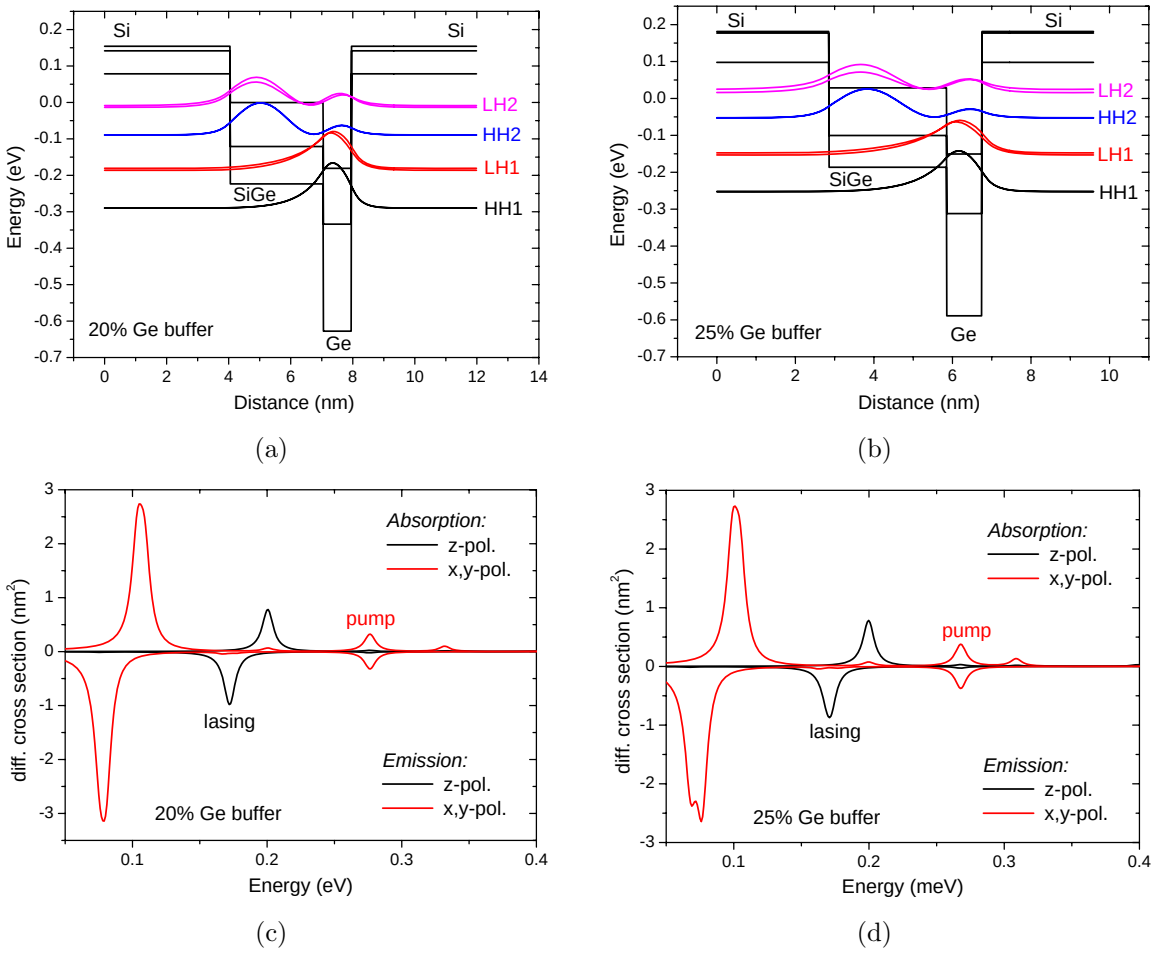

Figure A.2: Band structure for the samples grown on a 20% (a) and a 25% (b) germanium relaxed buffer. The corresponding absorption spectra (c,d) were calculated at an in-plane k-vector of 0.18nm^{-1}.

a different LH-HH splitting in the structure which leads to slightly different transition energies between the states. The calculated absorption and emission spectra for those samples are shown in Figure A.2c and d. For clarity, the absorption from the ground state (HH1) is plotted with positive sign and the emission from the upper laser state (LH2) with negative sign. For the 20% sample, the energy of the pumping transition is predicted at 277meV and the lasing at 172meV. For the sample with 25% Ge total Ge content, those values are slightly down-shifted to 269meV and 170meV, respectively. The re-absorption losses are expected to be negligible small as the lasing transition is well shifted from any absorption from the ground state.

A.0.3 Waveguide Absorption Measurements

The direct transmission measurements were carried out at a temperature of 20K. The preparation and measurement of the samples was carried out as described in Chapter 5. The results are described in the following.

Samples on 20% Ge buffers

The absorption measurements of the 20% Ge samples are shown in Figure A.3. For each polarization (TE and TM), the sample with cladding is compared to the one without cladding. It has to be noted that the peak at 400meV appearing in both polarizations is due to some monolayers of oil in the cryostat and is not discussed in the following.

In TM polarization we find a strong peak at 214meV and 223meV with and without

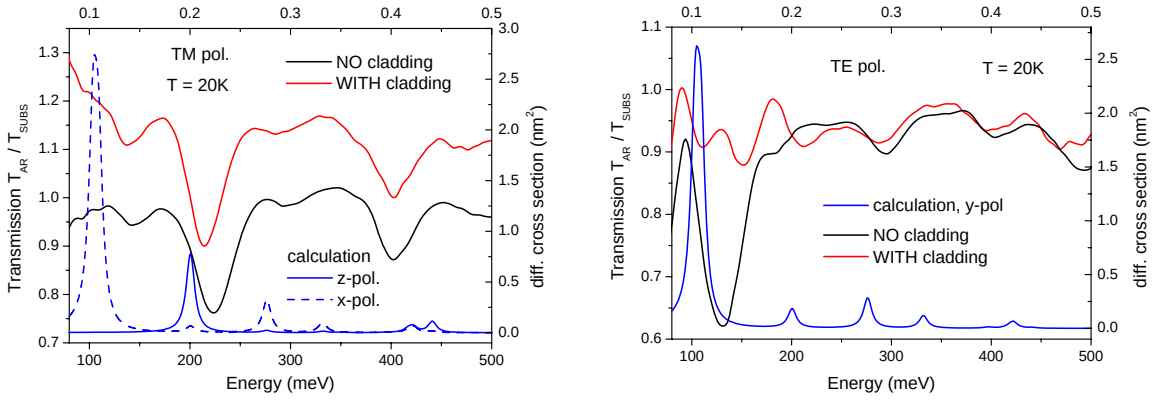

(a) (b)

Figure A.3: Absorption spectra for the samples grown on 20% germanium relaxed buffer in (a) TM polarization and (b) TE polarization. For comparison to the theory, the calculated absorption spectra are shown.

cladding, respectively. This peak is in reasonable agreement with the HH1-HH2 peak which is theoretically predicted at 201meV. The linewidth (which was more than 60meV for the samples reported before), is reduced to 36meV. The measured absorption of 28%

(with) and 24% (without cladding) is about $10\% - 15\%$ lower than predicted from theory[1] Besides the strong HH1-HH2 peak, two more features can be identified: The HH1-LH1 peak (mixed from TE) at about 140meV and the mixed part of the HH1-LH2 peak at 295meV. Those peaks are reproduced in the TE spectra of the sample without cladding. The pump transition HH1-LH2 has an absorption strength of about 10%. However, these results are not the same for the sample with cladding. Here, one mainly observes a wavy baseline without well resolved peaks. This difference in performance is probably due to the overlap factor of the standing wave pattern with the active region. In TE polarization, the HH1-LH1 peak can not be resolved for the sample without cladding. Comparison to the overlap factor of this structure shows that the coupling to the incident beam is almost zero. Therefore, no resonance is expected at this point. For the pumping transition HH1-LH2 however, a well pronounced resonance is expected which can not be clearly resolved due to the wavy baseline. This can not be explained by the overlap factor but by differences in the growth. Possible reasons are the different background pressure and/or some strain which is introduced during the growth of the cladding. Furthermore, the higher temperature at which the cladding is grown (450° instead of 300° as for the active region) may enhance relaxation processes in the structure.

However, the fact which can be stated from these samples is that the background ab-

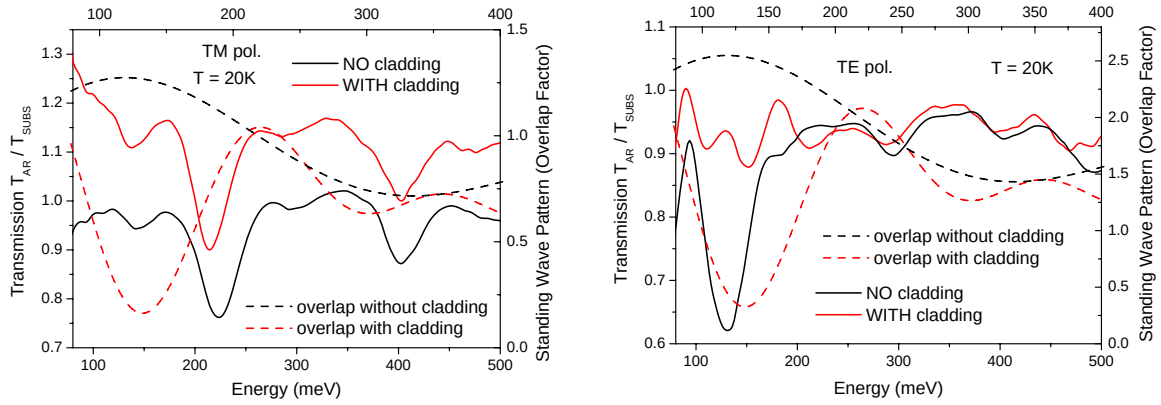

(a) (b)

Figure A.4: Absorption spectra for the samples grown on 20% germanium relaxed buffer compared to the overlap factor with the standing wave pattern in (a) TM polarization and (b) TE polarization.

sorption is strongly reduced. By comparing the calculated standing wave pattern (formed by the interaction of the incident beam with the beam reflected at the surface) to the absorption spectra (see Figure A.4), the strong influence of the incident beam is missing. This includes that observed peaks are not due to a modulation of the broad background but are indeed originating from the intersubband transitions. Furthermore, one can draw the conclusion that the strong influence of the standing wave in the previous samples was

[1]The theoretically predicted percentage of absorption was calculated by multiplying the differential cross section with the number of passes, the coupling factor for the 45° geometry, the number of periods, the doping and the ratio between assumed and measured linewidth.

due to growth problems. The latter ones caused an intersubband resonance as broad as the whole spectrum and did therefore not allow to determine a well defined peak. The new samples show that it is possible to obtained well resolved intersubband absorption spectra from direct transmission measurements from SiGe samples.

Samples on 25% Ge buffers

The good results obtained for the 20% Ge samples are also confirmed by the 25% Ge ones. The obtained absorption spectra in TM and TE polarization are shown in Figure A.5. For those samples, the one without cladding shows clearly stronger absorption peaks than the one with cladding. In the TM spectra, the HH1-LH2 peak can be resolved for both

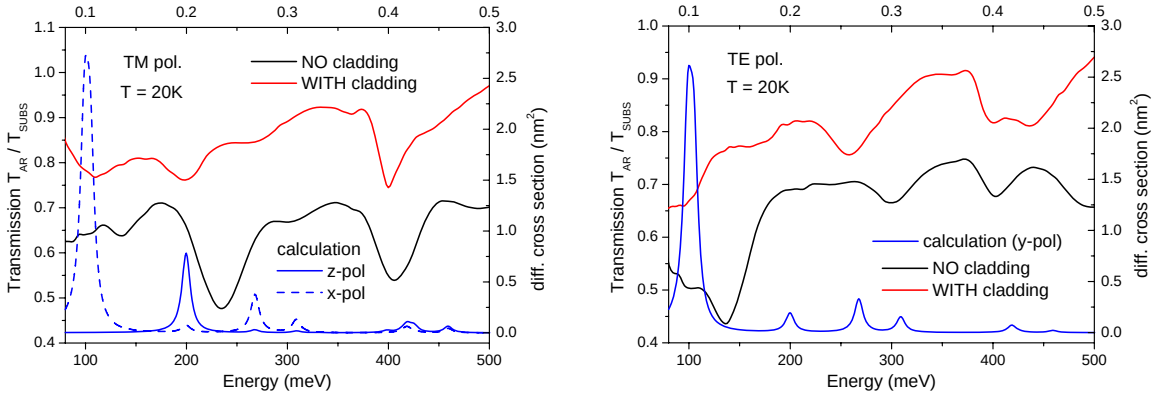

(a) (b)

Figure A.5: Absorption spectra for the samples grown on 25% germanium relaxed buffer in (a) TM polarization and (b) TE polarization. For comparison to the theory, the calculated absorption spectra are shown.

samples at 235meV and 200meV (without and with cladding) but the peak of the sample without cladding is three times stronger than the one from the sample with cladding. However, the peak position of the sample with cladding fits to the calculated value of 199meV while we find a deviation of 36meV for the sample without cladding. The origin of this behavior is not clarified.
In the TE polarization, the HH1-LH1 transition can only be detected for the sample without cladding at an energy of 136meV which is again at higher energy than expected. For the other sample, the resonance is downshifted into the cut off of the detector. The pumping transition was resolved for both samples at 300meV (without) and 258meV (with cladding), respectively. Comparison to the theory shows an analogous behavior as in the TM polarization: The absorption peaks of the sample with cladding coincide with the calculated values but shows less pronounced peaks and a clear sign of free carrier absorption in the low energy tail. However, comparison of the overlap factor of the standing wave pattern with the active region does not show a coincidence between smaller absorption in the sample with cladding (see Figure A.6) which could explain the above behavior.

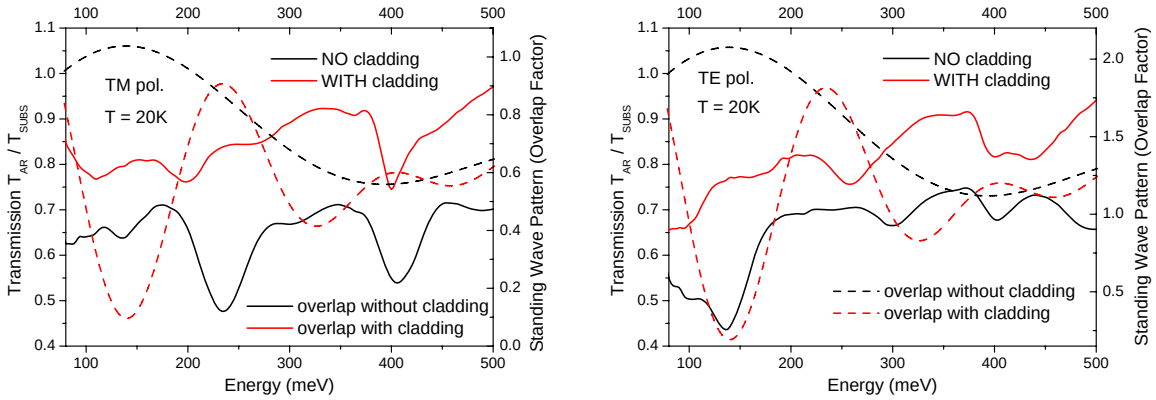

(a) (b)

Figure A.6: Absorption spectra for the samples grown on 25% germanium relaxed buffer compared to the overlap factor with the standing wave pattern in (a) TM polarization and (b) TE polarization.

A.0.4 Conclusion

The samples presented above show very good structural quality. This is approved by the transmission measurements which provide the best absorption data obtained from such waveguide structures so far. Still, the optical pumping experiments performed so far, did not show lasing action. However, calculations of the Raman gain on the basis of those structures show that only a reduction of the linewidth of 10meV or an about three times higher pump power could be sufficient to overcome the waveguide losses and obtain lasing action. Another fact which could be influenced by design and growth, is the absorption strength. Here, optimization of the cladding layer growth and/or higher doping levels could provide a stronger absorption which would increase the internal pump power. Finally, due to the good growth quality, one could try to grow thicker germanium layers (10Å or 11Å) in order to shift the pump energy even higher ($\sim$ 350meV) where the pump laser is most efficient.
As a conclusion, one can state that the quality of the latest samples is a big step towards the aim of an optically pumped SiGe laser. With the above mentioned steps the realization of such a laser should be possible.

Acknowledgment

First of all, I would like to thank my doctoral thesis adviser at the University of Neuchâtel, Prof. Jérôme Faist, for the supervision of my thesis. His continuous support and encouraging discussions were very important for me and my work.

Secondly, I want to thank my supervisor at the Paul-Scherrer-Institute (PSI), Dr.Hans Sigg, who introduced me in the field of spectroscopy. With his manifold ideas and hints he was always a great support for any kind of optical setup. I also thank him for his help in physical as well as administrative questions and especially for the careful review of this thesis.

Many thanks also to Dr. Soichiro Tsujino, for his support in many theoretical questions and practical ideas, for providing a sophisticated simulation tool (together with Mathilde Rufenacht) and a lot of design ideas. His comments and compact theoretical considerations were always encouraging to improve the deep insight into theoretical physics. Besides this, I also want to thank him for his remarks on this thesis.

For his professional supervision at the PSI and always helpful support I would like to thank Prof. Detlev Grützmacher who moved to the RWTH Aachen but was always a valuable contact.
I also want to thank Prof. Peter Hamm (University of Zürich) and Prof. Philipp Aebi (University of Neuchâtel) for critically reading the manuscript and acting as co-examiners.

A special thanks goes to Dr.Gregor Mussler for his great enthusiasm and MBE growth skills. A lot of this work would not have been possible without his support and his ability to warm up with many different ideas.
For providing TEM pictures of many different samples, I would like to thank Dr. Elisabeth Müller. For a good collaboration and fruitful discussions, I want to thank Dr. Thomas Fromherz (University of Linz, Austria) and Dr. Ulf Gennser (LPN-CNRS, Marcoussis, France). Furthermore, Dr.Giacomo Scalari for his help with magnetic measurements in Neuchâtel and Virgiliu Botan for his time and patience to show us the world of time-resolved spectroscopy.

A warm thank-you goes to Anja Weber and Stefan Stutz. Anja was an important help in processing samples and the art of taking nice SEM pictures. Stefan was polishing reams

of samples for me and was always a big help for problems like new sample holders or not-working Labview programs. Besides their technical support, the numerous off-topic discussions and funny stories to tell made them very good colleagues.

As the main part of my work was carried out at the Laboratory of Micro- and Nanotechnology at PSI, I would like to thank the head of the laboratory, Dr. Jens Gobrecht for general support and all the LMN technicians for their readily assistance.
A big thanks goes to all the (Ex-)PhD students of LMN. Some of them became more friends than colleagues and they have to be acknowledged for all the time we spent together outside PSI in the Beergarden or Pub, on the skiing slopes, on inline skates or even classical concerts: I am very grateful to my 'Villa mates': Ana Diaz, Anja Weber, Slawomir Czekaj, Dirk Backes and Elena Mengotti. The main-building people: Philipp Käser, Claudio Vanoni, Christian Dais, Patrick Farquet, Sandro Bellini and last but not least Peter Morf. In that respect, I also would like to thank Valeriya Shushunova for her always open ears and her support during her time at PSI.

Apart from the scientific friends I met at PSI, I would like to thank my friends in Germany for all what they are to me, especially: Tina and Ute (for everlasting support), Lehmi (acting as big brother), Prof & Kerstin, Stephi, Robert, Ralli and George (thanks for all the nice moments spent on holidays in the mountains, on the bike and on skis as well as on parties).

Finally, I would like to pass a full load of acknowledgment and a warm thank-you to my family: My parents, Susanne and Gernot Scheinert, who were always standing behind me, helping me with their advice and sometimes showing me 'the other side'. And my sister and her husband for all the nice diners, skiing days and discussions on very different aspects of life. Thank you for your huge support during this work!

This work was supported by the Swiss National Science Foundation.

Bibliography

[1] J.Faist, F.Capasso, D.L.Sivco, C.Sirtori, A.L.Hutchinson and A.Y.Cho, Science 264, 553, 1994.

[2] M.Tacke, "Lead Salt Lasers" in *Long wavelength infrared emitters based on quantum wells and superlattices*, edited by Manfred Helm, volume 6, chapter 9, pp.347-396, Gordon and breach Science, Amsterdam, 2000.

[3] H.K.Choi and G.W.Turner, "Antimonide-based mid-infrared laser" in *Long wavelength infrared emitters based on quantum wells and superlattices*, edited by Manfred Helm, volume 6, chapter 9, pp.347-396, Gordon and breach Science, Amsterdam, 2000.

[4] R.Q.Yang, B.H.Yang, D.Zhang, C.H.Lin, S.J.Murry, H.Wu and S.S.Pei, Appl.Phys.Lett.71 (17), 2409-2411, 1997.

[5] A.A.Andronov, I.V.Zverev, V.A.Kozlov, Y.N.Nozdrin, S.A.Pavlov and V.N.Shastin, JEPT Lett.40 (2), 804-807, 1984.

[6] J.C.Campbell, "Optical Applications" in *Germanium Silicon: Physics and Materials*, edited by R.Hull and J.C.Bean, volume 56, pp. 347, Acacdemic Press, 1998.

[7] W.L.Ng, M.A.Lourenco, R.M.GWillam, S.Ledaln, G.Shao and K.P.Homewood, Nature 410, 192, 2001.

[8] M.A.Green, J.Zhao, A.Wang, P.J.Reece and M.Gal, Nature 412, 805, 2001.

[9] L.T.Canham, Appl.Phys.Lett.57 (10), 1046-1048, 1990.

[10] N.Koshida and H.Koyama, Appl.Phys.Lett.60 (3), 347-349, 1992.

[11] L-Pavesi, L.D.Negro, C.Mazzoleni, G.Franzo and F.Priolo, Nature 408, 440, 2000.

[12] M.H.Nayfeh, N.Barry, J.Thierren, O.Akcakir, E.Gratton and G.Belomoin, Appl.Phys.Lett.78 (8), 1131, 2001.

[13] G.Allan, C.Delerue and M.Lannoo, Phys.Rev.Lett.76 (16), 2961-2964, 1996.

[14] G.Franzo, F.Priolo, S.Coffa, A.Polman and A.Carnera, Appl.Phys.Lett.64 (17), 2235, 1994.

[15] S.Coffa, G.Franzo, F.Priolo, A.Pacelli and A.Lcaita, Appl.Phys.Lett.73 (1), 93-95, 1998.

[16] Y.Arakawa and H.Sakaki, Appl.Phys.Lett.40 (11), 939-941, 1982.

[17] A.Beyer, E.Müller, H.Sigg, S.Stutz, D.Grützmacher, O.Leifeld and K.Ennslin, Appl.Phys.Lett.77 (20), 3218-3220, 2000.

[18] K.Eberl, O.G.Schmidt, R.R.Duschl, O.Kienzle, E.E.Ernst and Y.Rau, Thin Solid Films 369, 33, 2000.

[19] K.Kato and Y.Tohmori, IEEE Journal of Sel.Topics of Quantum Electronics 6, 4-13, 2000.

[20] E.L.Friedrich, M.G.Oberg, B.Broberg, S.Nilsson and S.Valette, Jounal Lightwave TEchnology 10, 336-340, 1992.

[21] J.Sasaki, M.Itoh, T.Tamanuki, H.Hatakeyama, S.Kitamura, T.Shimoda, T.Kato, IEEE Transactions on Advanced Packaging 24, 569-575, 2001.

[22] C.Monat et al., Conf.Proc. Int.Conf. on Indium Phosphide Materials FA24, 603-606, 2001.

[23] A.W.Fang, H.Park, O-Cohen, R.Jones, M.J.Paniccia and J.E.Bowers, Opt.Express 14, 9203-9210, 2006.

[24] H.Park, A.W.Fang, S.Kodama and J.E.Bowers, Opt.Express 13, 9460-9464, 2005.

[25] J.Van Campenhout, P.Rojo-Romeo, P.Regreny, C.Seassal, D.Van Thourhout, S.Verstuyft, L.Di Cioccio, J.-M.Fedeli, C.Lagahe and R.Baets, Opt.Express 15 (11), 6744-6749, 2007.

[26] G.Vecchi, F.Raineri, I.Sagnes, A.Yacomotti, P.Monnier, T.J.Karle, K.-H.Lee, R.Braive, L.Le Gratiet, S.Guilet, G.Beaudoin, A.Talneau, S.Bouchoule, A.Levenson and R.Raj, Opt.Express 15 (12), 7551-7556, 2007.

[27] H.Rong, A.Liu, R.Jones, O.Cohen, D.Hak, R.Nicolaescu, A.Fang and M.Paniccia, Nature 433, 292-294, 2005.

[28] H.Rong, R.Jones, A.Liu, O.Cohen, D.Hak, A.Fang and M.Paniccia, Nature 433, 725-727, 2005.

[29] J.Faist, "Silicon shines on", Nature 433, 691-692, 2005.

[30] Q.Xu, V.Almeida and M.Lipson, Opt.Express 12, 4437-4442, 2004.

[31] T.K.Liang and H.K.Tsang, Appl.Phys.Lett.85, 3343-3345, 2004.

[32] O.Boyraz and B.Jalali, Opt.Express 12, 5269-5273, 2004.

[33] Y.R.Shen, *The Principles of Nonlinear Optics*, Wiley&Sons 1984, Chap.10, pp.141-186.

[34] G.Dehlinger, Dissertation, *Vertical Transport and Intersubband Emission in SiGe*, Diss.ETH Nr.114117

[35] L.Diehl, Dissertation, *Development of Si/SiGe Quantum Cascade Emitters* (2003).

[36] G.Dehlinger, L.Diehl, U.Gennser, H.Sigg, J.Faist, K.Ensslin, D.Grützmacher and E.Müller, Science 290, 2277 (2000).

[37] L.Diehl et al., Appl.Phys.Lett. 81, 4700 (2002).

[38] L.L.Chang, L.Esaki and R.Tsu, Appl.Phys.Lett.24, 593-595, 1974.

[39] R.Dingle, W.Wiegmann and C.H.Henry, Phys.Rev.Lett.33, 827, 1974.

[40] L.C.West and S.J.Eglash, Appl.Phys.Lett.46 (12), 1156-1158, 1985.

[41] C.Gmachl, H.M.Ng, S.G.Chu and A.Y.Cho, Appl.Phys.Lett.77 (23), 3722-3724, 2000.

[42] M.Helm, F.M.Peeters, F.DeRosa, E.Colas, J.P.Harbison and L.T.Florez, Phys.Rev.B 43 (17), 13983-13991, 1991.

[43] J.Faist, F.Capasso, D.L.Sivco, A.L.Hutchinson, S.Chu and A.Y.Cho, Appl.Phys.Lett.72, 680-682, 1998.

[44] R.Colombelli, F.Capasso, C.Gmachl, A.L.Hutchinson, D.L.Sivco, A.Tredicucci, M.C.Wanke, A.Michael Seregent and A.Y.Cho, Appl.Phys.Lett.78, 2620-2622, 2001.

[45] G. Scalari, L. Ajili, J. Faist, H. Beere, E. Linfield, D. Ritchie, and G. Davies, Appl.Phys.Lett.82, 3165, 2003.

[46] L. Ajili, G.Scalari, J. Faist, H. Beere, E. Linfield, D. Ritchie, and G. Davies, Appl.Phys.Lett.85, 3986, 2004.

[47] M.Rieger and P.Vogel, Phys.Rev.B 48, 14276, 1993.

[48] S.A.Lynch, R.BAtes, D.J.Paul; D.J.Norris, A.G.Cullis, Z.Ikonic, R.W.Kelsall, P.Harrison, D.D.Arnone and C.R.Pigeon, Appl.Phys.Lett.81 (9), 1543-1545, 2002.

[49] L.Friedman, G.Sun and R.A.Soref, Appl.Phys.Lett.78 (4), 401-403, 2001.

[50] R.F.Kazarinov and R.A.Suris, Sov.Phys.Semicond. 5 (4), 707-709, 1971.

[51] M.Helm, P.England, E.Colas, F.DeRosa and S.J.Allen, Phys.Rev.Lett.63 (1), 74-77, 1989.

[52] M.Beck, D.Hofstetter, T.Aellen, J.Faist, U.Oesterle, M.Ilegems, E.Gimi and H.Melchior, Science 295, 301-305, 2002.

[53] R.Köhler, A.Tredicucci, F.Beltram, H.E.Beere, E.H.Linfield, A.G.Davies, D.A.Ritchie, R.C.Iotti and F.Rossi, Nature 417, 156-159, 2002.

[54] C.Sirtori, P.Kruck, S.Barbieri, P.Collot, J.Nagle, M.Beck, J.Faist and U.Oesterle, Appl.Phys.Lett.73 (24), 3486-3488, 1998.

[55] K.Ohtani and H.Ohno, Appl.Phys.Lett.82 (7), 1003-1005, 2003.

[56] C.Sirtori, F.Capasso, J.Faist, A.L.Hutchinson, D.L.Sivco and A.Y.Cho, IEEE J.Quantum Electronics 34 (9), 1722-1729, 1998.

[57] J.Faist, F.Capasso, C.Sirtori, D.L.Sivco, J.N.Baillargeon, A.L.Hutchinson, S.G.Chu and A.Y.Cho, Appl.Phys.Lett.68 (26), 3680-3682, 1996.

[58] J.Faist, C.Gmachl, F.Capasso, C.Sirtori, D.L.Sivco, J.N.Baillargeon and A.Y.Cho, Appl.Phys.Lett.70 (20), 2670-2672, 1997.

[59] R.M.Williams, J.F.Kelly, J.S.Hartmann, S.W.Sharpe, M.S.Taubmann, J.L.Hall, F.Capasso, C.Gmachl, D.L.Sivco, J.N.Baillargeon and A.Y.Cho, Opt.Lett.24 (24), 1844-1846, 1999.

[60] Y.P.Gousev, I.V.Korolev, K.Korolev, V.P.Sinis, M.S.Kagan, E.E.Haller, M.A.Obmoblyudov, I.N.Yassievitch and K.A.Chao, Appl.Phys.Lett.75, 757-759, 1999.

[61] B.A.Paldus, T.G.Spence, R.N.Zare, J.Oomens, F.J.Harren, D.H.Parker, C.Gmachl, F.Capasso, D.L.Sivco, J.N.Baillargeon, A.L.Hutchinson and A.Y.Cho, Opt.Lett.24 (3), 178-180, 1999.

[62] D.Hofstetter, M.Beck, J.Faist, M.Nägele and M.W.Siegrist, Opt.Lett.26 (12), 887-889, 2001.

[63] A.Müller, M.Beck, J.Faist, U.Oesterle and M.Ilegems, Appl.Phys.Lett.75 (11), 1509-1511, 1999.

[64] K.Namjou, S.Cai, E.A.Whittaker, J.Faist, C.Gmachl, F.Capasso, D.L.Sivco and A.Y.Cho, Opt.Lett.23 (3), 219-221, 1998.

[65] N.Mustafa, L.Pesquera, C.Y.Cheung and K.A.Stone, IEEE Photon.Technol.Lett.11 (5), 527-529, 1999.

[66] J.Faist, F.Capasso, C.Sirtori, D.L.Sivco and A.Y.Cho, "Quantum Cascade Lasers" in *Intersubband Transitions in quantum wells: Physics and device applications II*, edited by H.C.Liu and F.Capasso, Volume 66, Chapter 1, pages 1-83, Academic Press, 2000.

[67] S.Blaser, D.Hofstetter, M.Beck And J.Faist, IEEE Elect.Lett.37 (12), 778-780, 2001.

[68] M.J.Shaw and M.Jaros, "Fundamental Physics of strained layer GeSi: Quo Vadis?", in *Germanium Silicon: Physics and Materials*, edited by R.Hull and J.C.Bean, Volume 56, pages 169-223, Academic Press, 1998.

[69] E.Kasper, editor, *Properties of strained and relaxed Silicon and Germanium*, Volume 12, INSPEC, the Institution of Electrical Engineers, London, 1995.

[70] K.Reimann, R.A.Kaindl and M.Woermer, Phys.Rev.B 65, 45302, 2001.

[71] T.Fromherz, E.Koppensteiner, M.Helm, G.Bauer, J.F.Nützel, and G.Abstreiter, Phys.Rev. B50, 15073 (1994)

[72] S.M.Sze, Semiconductor Devices: Physics and Technology, John Wiley & Sons Inc., New York, 1985.

[73] M.L.Thewalt, D.A.Harrison, C.F.Reinhart, J.A.Wolk and H.Lafontaine, Phys.Rev.Lett. 79 (2), 269, 1997.

[74] N.W.Ahshcroft and N.D.Mermin, *Solid State Physics*, Harcourt Brace College Publishers, Fort Worth, 1976.

[75] J.Bardeen, J.Chem.Phys. 6, 367-371, 1938.

[76] F.Seitz, *The Modern Theory of Solids*, McGraw Hill, New York, 1940, p.352.

[77] W.Shockley, Phys.Rev. 78, 173-174, 1950.

[78] , G.Dresselhaus, A.F.Kip and C.Kittel, Phys.Rev. 98, 368-384, 1955.

[79] E.O.Kane, "The $k \cdot p$ method", Chapter 3, in R.K.Willardson and A.C.Beer, Eds., *Seminconductor and Semimetals*, Vol.1, Academic, New York, 1966.

[80] J.M.Luttinger and W.Kohn, Phys.Rev.97, 869-883, 1995.

[81] R.Winkler, M.Merkler, T.Darnhofer and U.Roessler, Phys.Rev. B 53 (16), 10858-10865, 1996.

[82] M.Helm, 'The basic Physiscs of intersubband transitions' (Section V) in *Intersubband Transitions in quantum wells: Physics and device applications I*, edited by H.C.Liu and F.Capasso, Volume 62, Chapter 1, pages 1-99, Academic Press, 2000.

[83] S.L.Chuang, "Theory of Electronic Band Structures in Semiconductors" (Chpater IV) in *Physics of Optoelectronic Devices*, pages 124-185, Wiley & Sons, 1995.

[84] C.G. Van de Walle, Phys.Rev. B 39, 1871-1883, 1989.

[85] C.G. Van de Walle and R.M.Martin, Phys.Rev. B 34 (8), 5621, 1986.

[86] L.C.Adreani, A.Pasquarello and F.Bassani, Phys.Rev.B 36 (11), 5887 (1987).

[87] R.Wessel and M.Altarelli, Phys.Rev.B 39 (17), 12802 (1989).

[88] R.Wessel and M.Altarelli, Phys.Rev.B 40 (18), 12457 (1989).

[89] B.W.Kim and A.Majerle, J.Appl.Phys. 77 (9), 4552 (1995).

[90] Y.C.Chang and R.B.James, Phys.Rev.B 39, 12672 (1989).

[91] E.Kasper, H.J.Herzog and H.Kibbel, Appl.Phys.Lett. 8, 199-205 (1975).

[92] A.Krost, in *Optical Characterization of Epitaxial Semiconductor Layers*, Chapter 4, edited by G.Bauer and Richter, Springer Verlag.

[93] E.Müller, *Transmission Electron Microscopy Study of Si_mGe_n Strained-Layer Superlattice and $Si_{1-x}GE_x$ Alloys on Si(001) Grown by Molecular Beam Epitaxy*, Diss. ETH Nr.9848.

[94] J.Faist, M.Beck and T.Aellen, Appl.Phys.Lett. 78, 147 (2001).

[95] R.A.Kaindl, M.Wurm, K.Reimann, M.Woerner, T.Elsaesser, C.Miesner, K.Brunner and G.Abstreiter, Phys.Rev.Lett. 86, 1122 (2001).

[96] I.Bormann, K.Brunner, S.Hackenbuchner, G.Abstreiter, S.Schmult and W.Wegscheider, Appl.Phys.Lett. 83, 26, 5371 (2003).

[97] L.Diehl, H.Sigg, G.Dehlinger, D.Grützmacher, E.Müller, U.Gennser, I.Sagnes, T.Fromherz, Y.Campidelli, O.Kermarrec, D.Bensahel, and J.Faist, Appl.Phys.Lett. 80, 3274 (2002).

[98] A.Borak, S.Tsujino, H.Sigg,, C.V.Falub, M.Scheinert, L.Diehl, D.Grützmacher, E.Müller, U.Gennser, Y.Campidelli, O.Kermarrec, D.Bensahel, and J.Faist, *Recent Results on the road to a SiGe quantum cascade laser* in Proc.Mater.Res.Symp., vol832, 2005, pp.F4.2.1-14.

[99] S.Tsujino, H.Sigg, M.Scheinert, D.Grützmacher and J.Faist, IEEE Journal of selected topics in Quantum Electronics, Vol.12, No.6, 1642 (2006).

[100] T.Ando, J. Phys. Soc. Jpn. 54, 2671 (1985).

[101] T.Unuma, T.Takahashi, T.Noda, M.Yoshita, H.Sakaki, M.Baba, and H.Akiyama, Appl.Phys.Lett. 78, 3448 (2001).

[102] S.Tsujino, A.Borak, E.Müller, M.Scheinert, C.V.Falub, H.Sigg, D.Grützmacher, M.Giovannini, and J.Faist, Appl.Phys.Lett. 86, 062113 (2005).

[103] Y.Fedoryshyn, L.Diehl, M.Beck, M.Giovannini, V.Ortiz, C.Sirtori, and J.Faist, *QCL with Wavegide Design with Ge Layer*, 2006.

[104] S.Tsujino, C.V.Falub, E.Müller, M.Scheinert, L.Diehl, U.Gennser, T.Fromherz, A.Borak, H.Sigg, D.Grützmacher, Y.Campidelli, O.Kermarrec, and D. Bensahel, Appl.Phys.Lett. 84, 2829 (2004).

[105] S.Tsujino, A.Borak, C.V.Falub, T.Fromherz, L.Diehl, H.Sigg, and D.Grützmacher, Phys.Rev.B 72, 153315 (2005).

[106] M.Myronov, P.J.Philipps, T.E.Whall, and E.H.C.Parker, Appl.Phys.Lett. 80, 3557 (2002).

[107] L.L.Chang, L.Esaki, and R.Tsu, Appl.Phys.Lett. 24, 593-595 (1974).

[108] H.C.Liu, D.Landherr, M.Buchanan and D.C.Houghton, Appl.Phys.Lett. 52 (21), 1809 (1988).

[109] Z.Matutinovic-Krstelj, C.W.Liu, X.Xiao, and J.Sturm, Appl.Phys.Lett. 62 (6), 603-605 (1993).

[110] S.Tsujino, D.Grützmacher and U.Gennser "Resonant Tunnelling Devices" in *The Silicon Heterostructure Handbook*, edited by J.D.Cressler, Chapter6.2, pp. 647, Taylor & Franscis, 2006.

[111] U.Gennser, M.Scheinert, L.Diehl, S.Tsujino, A.Borak, C.V.Falub, D.Grützmacher, A.Weber, D.K.Maude, G.Scalari, Y.Campidelli, O.Kermarrec and D.Bensahel, Europhys.Lett. 74 (5), 882-888 (2006).

[112] J.-Y.Marzin and J.-M.Gérard, Phys.Rev.Lett. 62, 2172 (1989).

[113] E.E.Mendez, W.I.Wang, B.Ricco and L.Esaki, Appl.Phys.Lett. 47, 415 (1985).

[114] R.K.Hayden, D.K.Maude, L.Eaves, E.C.Valadares, M.Henini, F.W.Sheard, O.H.Hughes, J.C.Portal and L-Cury, Phys.Rev.Lett. 66, 1749 (1991).

[115] G.Schuberth, G.Abstreiter, E.Gornik, F.Schäffler andJ.F.Luy, Phys.Rev.B. 43, 2280 (1991).

[116] U.Gennser, V.P.Kensan, D.A.Syphers, T.P.Smith, S.S.Iyer and E.S.Yang, Phys.Rev.Lett. 67, 3828 (1991).

[117] A.Zaslavsky, T.P.Smith, D.A.Grützmacher, S.Y.Lin, T.O.Sedgwick and D.A.Syphers, Phys.Rev.B 48, 15112 (1993).

[118] R.K.Hayden et al., Semicond.SciTechnology 7, B413 (1992).

[119] P.Gassot, U.Gennser, A.Zaslavsky, D.Grützmacher and J.C.Portal, Physica E 3, 758 (1998).

[120] J.M.Luttinger, Phys.Rev. 102, 1030 (1956).

[121] O.Gauthier-Lafaye, P.Bouceaud, F.H.Julien, S.Sauvage, S.Cabaret, J.M.Lourtioz, V.Thierry-Mieg and R.Planel, Appl.Phys.Lett. 71 (25), 3619-3621 (1997).

[122] O.Gauthier-Lafaye, F.H.Julien, S.Cabaret, J.M.Lourtioz, G.Strasser, E.Gornik, M.Helm and P.bois, Appl.Phys.Lett. 74 (11), 1537-1539 (1999).

[123] H.C.Liu, Iva W.Cheung, A.J.SpringThorpe, C.Dharma-wardana, Z.R.Wasilewski, D.J.Lockwood and G.C.Aers, Appl.Phys.Lett. 78 (23), 3580-3582 (2001).

[124] J.B.Khurgin, G.Sun, L.R:Friedman and R.A.Soref, J.Appl.Phys. 78 (12), 7398-7400 (1995).

[125] A.Belyanin, M.Troccoli and F.Capasso, in *Intersubband Transitions in Quantum Structures*, edited by R.Paiella (McGraw-Hill, 2006), Chap.6, pp.237-283.

[126] T.Elsaesser, in *Intersubband Transitions in Quantum Structures*, edited by R.Paiella (McGraw-Hill, 2006), Chap.4, pp.135-175.

[127] K.Kempa, P.Bakshi, J.Engelbrecht and Y.Zhou, Phys.Rev.B 61 (16), 11083 (2000).

[128] 'The basic Physiscs of intersubband transitions' (Section V) in *Intersubband Transitions in quantum wells: Phsics and device applications I*, edited by H.C.Liu and F.Capasso, Volume 62, Chapter 1, pages 1-99, Academic Press, 2000.

[129] E.Rosencher and Ph.Bois, Phys.Rev.B 44 (20), 11315, 1991.

[130] Jackson,*Classical Electrodynamics*, Chapter 7, pages 269-327, Wiley&Sons 1975.

[131] E.Rosencher and B.Vinter, *Optoelectronics*, Cambridge University Press, 2002.

[132] T.Fromherz, M.Meduna, G.Bauer, A.Borak, C.V.Falub, S.Tsujino, H.Sigg and D.Grützmacher, JAP 98 (4), 044501 (2005).

10

Published Work

- M. Scheinert, H. Sigg, S.Tsujino, M. Giovannini and J. Faist, *Intersubband Raman Laser from GaInAs/AlInAs double quantum wells*, Appl. Phys. Lett **91**, 131108 (2007).
- S. Tsujino, H. Sigg, M. Scheinert, D. Grützmacher and J. Faist, *Strategies to improve optical gain and waveguide loss in strain-compensated SiGe quantum cascade midinfrared emitters*, IEEE Jorunal of Selected Topics in Quantum Electronics, **12 (6)** part 2, 1642 (2006).
- U. Gennser, M. Scheinert, L. Diehl, S. Tsujino, A. Borak, C.V. Falub, D. Grützmacher, A. Weber, D.K. Maude, G. Scalari, Y. Campidelli, O. Kerramec, D. Bensahel, *Total angular momentum conservation during tunnelling through semiconductor barriers*, Europhys. Lett. **74**, 882 (2006).
- S. Tsujino, A. Borak, E. Müller, M. Scheinert, C.V. Falub, D.Grützmacher, M.Giovannini and J.Faist, *Interface-roughness-induced broadening of intersubband electroluminescence in p-SiGe and n-GaInAs/AlInAs quantum cascade structures*, Appl. Phys. Lett. **86**, 062113 (2005).
- A. Borak, S. Tsujino, H. Sigg, C.V. Falub, M. Scheinert, L. Diehl, D. Grützmacher, E. Müller, U. Gennser, Y. Campidelli, O. Kerramec, D. Bensahel and J. Faist, *Recent Results on the road to a SiGe quantum cascade laser*, Proc. Mater. Res. Symp. **832**, F4.2.1- F4.2.14 (2005).
- S. Tsujino, C.V. Falub, E. Müller, M. Scheinert, L. Diehl, U. Gennser, T. Fromherz, A. Borak, H. Sigg, D. Grützmacher, D. Bensahel, *Hall mobility of narrow Si0.2Ge0.8-Si quantum wells on Si0.5Ge0.5 relaxed buffer substrates* Appl. Phys. Lett. **84**, 2829 (2004).
- Conference proceedings.